General Disclaimer

One or more of the Following Statements may affect this Document

- This document has been reproduced from the best copy furnished by the organizational source. It is being released in the interest of making available as much information as possible.

- This document may contain data, which exceeds the sheet parameters. It was furnished in this condition by the organizational source and is the best copy available.

- This document may contain tone-on-tone or color graphs, charts and/or pictures, which have been reproduced in black and white.

- This document is paginated as submitted by the original source.

- Portions of this document are not fully legible due to the historical nature of some of the material. However, it is the best reproduction available from the original submission.

Produced by the NASA Center for Aerospace Information (CASI)

NGR-47-004-090

COLLEGE OF ENGINEERING

(NASA-CR-153263) NONLINEAR ANALYSIS OF BONDED JOINTS WITH THERMAL EFFECTS Interim Report, Sep. 1975 - May 1977 (Virginia Polytechnic Inst. and State Univ.) 201 p HC A10/MF A01 CSCL 20K G3/39

N77-26534

Unclas 36661

VIRGINIA POLYTECHNIC INSTITUTE AND STATE UNIVERSITY

JUL 1977
RECEIVED
NASA STI FACILITY
INPUT BRANCH

BLACKSBURG, VIRGINIA

College of Engineering
Virginia Polytechnic Institute and State University
Blacksburg, VA. 24061

VPI-E-77-19 June, 1977

Nonlinear Analysis of Bonded Joints with Thermal Effects

Edward A. Humphreys[1]

Carl T. Herakovich[2]

Department of Engineering Science and Mechanics

Interim Report - NASA Grant NGR 47-004-090

Prepared for: Materials Application Branch
National Aeronautics & Space Administration
Langley Research Center
Hampton, VA. 23665

[1] Graduate Student

[2] Professor

Approved for public release, distribution unlimited.

BIBLIOGRAPHIC DATA SHEET	1. Report No. VPI-E-77-19	2.	3. Recipient's Accession No.
4. Title and Subtitle NONLINEAR ANALYSIS OF BONDED JOINTS WITH THERMAL EFFECTS			5. Report Date June, 1977 6.
7. Author(s) Edward A. Humphreys and Carl T. Herakovich			8. Performing Organization Rept. No. VPI-E-77-19
9. Performing Organization Name and Address Virginia Polytechnic Institute and State University Engineering Science and Mechanics Blacksburg, Virginia 24061			10. Project/Task/Work Unit No. 11. Contract/Grant No. NASA NGR-47-004-090
12. Sponsoring Organization Name and Address National Aeronautics & Space Administration Langley Research Center Hampton, Virginia 23665			13. Type of Report & Period Covered 14.

15. Supplementary Notes

16. Abstracts

see page ii

17. Key Words and Document Analysis. 17a. Descriptors

bonded joints, composites, thermal stresses, nonlinear behavior, interlaminar stresses, finite elements, single lap, double lap, graphite-polyimide, boron-epoxy, adhesives, titanium, aluminum

17b. Identifiers/Open-Ended Terms

17c. COSATI Field/Group

18. Availability Statement	19. Security Class (This Report)	21. No. of Pages
Distribution unlimited	UNCLASSIFIED	
	20. Security Class (This Page) UNCLASSIFIED	22. Price

FORM NTIS-35 (REV. 10-73) ENDORSED BY ANSI AND UNESCO. THIS FORM MAY BE REPRODUCED USCOMM-DC 8265-P74

ACKNOWLEDGEMENT

This document represents a portion of the work accomplished under NASA Grant NGR 47-004-090 during the period September, 1975 through May, 1977. Dr. John G. Davis, Jr. of NASA Langley was the grant technical monitor and his continued interest and encouragement are appreciated. Thanks are also in order to Professors H. F. Brinson and M. P. Kamat, and Mr. H. W. Bergner, Jr. for their helpful suggestions, and to Ms. Frances Carter for typing the manuscript.

NONLINEAR ANALYSIS OF BONDED JOINTS WITH THERMAL EFFECTS

ABSTRACT

A numerical analysis of the nonlinear response of bonded joints is presented. Mechanical and thermal loadings are considered. Material stress-strain response is represented by Ramberg-Osgood approximations. Temperature dependent properties including modulus percent retentions and coefficients of expansion are modeled with linearly segmented curves. Bonded joints with graphite-polyimide, boron-epoxy, titanium, or aluminum adherends are analyzed using a quasi 3-dimensional finite element analysis. In adhesive bonded joints, the adhesives considered are Metlbond 1113 and AF-126-2.

Elastic results are presented for single and double lap joints, with and without adhesives. It is shown that mechanically induced stresses are greatly affected by longitudinal adherend stiffness. The effects of adherend transverse stiffness are shown to be significant in some cases. Residual curing stresses are shown to be significant in all joints except those with similar adherends and no adhesive.

Nonlinear results are presented for adhesive bonded joints. It is shown that adhesive nonlinearities are only significant in the predicted adhesive shear stresses. Adherend nonlinearities and temperature dependent properties are shown to have little effect upon the adhesive stress predictions under mechanical and thermal loadings.

TABLE OF CONTENTS

	Page
ACKNOWLEDGEMENT	ii
TABLE OF CONTENTS	iii
LIST OF FIGURES	vii
LIST OF TABLES	xv
CHAPTER	
1. INTRODUCTION	1
2. LITERATURE SURVEY	3
3. BASIC CONSIDERATIONS	7
3.1 Geometric Restrictions	7
3.2 Quasi 3-Dimensional Formulation	7
3.3 Bonded Joints	10
3.3.1 2-Dimensional Joint Formulation	10
3.3.2 Quasi 3-Dimensional Joint Formulation	11
3.4 Material Properties	12
3.4.1 Prediction of Laminate Stress-Strain Response	12
3.4.2 Prediction of Laminate Thermal Properties	14
3.5 Finite Element Formulation	22
3.6 Boundary Conditions for Joints	28
3.7 Qualifying Notes	30

Page

4. NONLINEAR ANALYSIS 31

4.1 Modifications of NONCOM1 31

4.1.1 Increased Finite Element Capacity . . . 31

4.1.2 Solution of Simultaneous Equations . . . 32

4.1.3 Three Dimensional Properties 35

4.1.4 Hygroscopic Analysis 35

4.1.5 Elevated Temperature and Moisture Content Analysis 36

4.2 Nonlinear Analysis 36

4.2.1 Incremental Loading Procedure 37

4.2.2 Nonlinear Data Input 37

5. RESULTS AND DISCUSSIONS 41

5.1 Materials Properties 41

5.2 Averaging of Finite Element Results 41

5.3 Finite Element Representations 44

5.4 Stress Free Temperature 44

5.5 Linear Elastic Results 47

5.5.1 Single Lap Joints with Adhesive 47

5.5.1.1 [0] Graphite-Polyimide Adherends 47

5.5.1.2 $[0/\pm45/90]_s$ Graphite-Polyimide Adherends 55

5.5.1.3 [90] Graphite-Polyimide Adherends 60

Page

5.5.1.4 [0] and [90] Graphite-Polyimide Adherends 60

5.5.2 Double Lap Joints with Adhesives 66

5.5.2.1 [0] Graphite-Polyimide Adherends 66

5.5.2.2 [90] Graphite-Polyimide Adherends 68

5.5.2.3 [0] and [90] Graphite-Polyimide Adherends 68

5.5.3 Single Lap Joints without Adhesive 71

5.5.3.1 [0] Graphite-Polyimide Adherends 73

5.5.3.2 [90] Graphite-Polyimide Adherends 73

5.5.3.3 [0] and [90] Graphite-Polyimide Adherends 75

5.5.4 Double Lap Joints without Adherends . . . 79

5.5.5 Elastic Loading Comparisons 84

5.6 NONLINEAR RESULTS 86

5.6.1 Single Lap Joints 86

5.6.1.1 Lap Shear Test 86

5.6.1.2 [0/90/0/90/0] Boron-Epoxy Adherends and AF-126-2 Adhesive . . . 97

Page

5.6.1.3 [0] Graphite-Polyimide Adherends and Metlbond 1113 Adhesive. . 103

5.6.1.4 $[\pm 45]_s$ Graphite Polyimide Adherends and Metlbond 1113 Adhesive. . 110

5.6.2 Double Lap Joints 116

5.6.2.1 Titanium Adherends and Metlbond 1113 Adhesive 116

5.6.2.2 [0] and [90] Graphite-Polyimide Adherends and Metlbond 1113 Adhesives 116

6. SUMMARY AND CONCLUSIONS 129

BIBLIOGRAPHY 132

APPENDICIES

A ELEMENT STIFFNESS MATRIX 135

B ADDENDA TO REFERENCE [1] 140

C MATERIAL PROPERTIES 148

D COMPUTER PROGRAM NONCOM1 166

LIST OF FIGURES

Figure No.		Page
1	Lap Joint Geometries	8
2	Laminate Geometry	13
3	Joint Boundary Conditions	23
4	Block Storage of Stiffness Matrix and Load Vector	34
5	Determination of Current Modulus with Ramberg-Osgood Approximations	39
6	Averaging of Finite Element Results	43
7	Partial Finite Element Grid for Joint with Adhesive Layer	45
8	Partial Finite Element Grid for Joint without Adhesive Layer	46
9	Elastic Mechanical and Curing Adhesive Stresses of a Single Lap Joint with [0] Gr/Pi Adherends and Metlbond 1113 Adhesive	48
10	Free Body Diagrams of Single Lap Joints Under Two Sets of Boundary Conditions	50
11	Deflected Shape of the Lower Adherend of a Single Lap Joint Under Mechanical Loading . . .	54
12	Elastic Mechanical and Curing Adhesive Stresses of a Single Lap Joint with $[0/\pm45/90]_s$ Gr/Pi Adherends and Metlbond 1113 Adhesive	56
13	Elastic Mechanical and Curing Adhesive Stresses	

Figure No.		Page
	of a Single Lap Joint with $[0/\pm45/90]_s$ Gr/Pi Adherends and Metlbond 1113 Adhesive, $\varepsilon_x=0$ . . .	58
14	Elastic Mechanical and Curing Adhesive Stresses of a Single Lap Joint with [90] Gr/Pi Adherends and Metlbond 1113 Adhesive	61
15	Elastic Mechanical Adhesive Stresses of a Single Lap Joint with [0] and [90] Gr/Pi Adherends and Metlbond 1113 Adhesive	62
16	Relative Displacements of a Single Lap Joint with [0] and [90] Gr/Pi Adherends and Metlbond 1113 Adhesive Normalized with Respect to the Adhesive Thickness	63
17	Elastic Curing Adhesive Stresses of a Single Lap Joint with [0] and [90] Gr/Pi Adherends and Metlbond 1113 Adhesive	65
18	Elastic Mechanical and Curing Adhesive Stresses of a Double Lap Joint with [0] Gr/Pi Adherends and Metlbond 1113 Adhesive	67
19	Elastic Mechanical and Curing Adhesive Stresses of a Double Lap Joint with [90] Gr/Pi Adherends and Metlbond 1113 Adhesive	69
20	Elastic Mechanical Adhesive Stresses of a Double Lap Joint with [0] and [90] Gr/Pi Adherends and Metlbond 1113 Adhesive	70

Figure No.		Page
21	Elastic Curing Adhesive Stresses of a Double Lap Joint with [0] and [90] Gr/Pi Adherends and Metlbond 1113 Adhesive	72
22	Elastic Mechanical Interfacial Stresses of a Single Lap Joint with [0] Gr/Pi Adherends and no Adhesive	74
23	Elastic Mechanical Interfacial Stresses of a Single Lap Joint with [90] Gr/Pi Adherends and no Adhesive	76
24	Elastic Mechanical Interfacial Stresses of a Single Lap Joint with [0] and [90] Gr/Pi Adherends and no Adhesive	77
25	Elastic Curing Interfacial Stresses of a Single Lap Joint with [0] and [90] Gr/Pi Adherends and no Adhesive	78
26	Elastic Mechanical Interfacial Stresses of a Double Lap Joint with [0] Gr/Pi Adherends and no Adhesive	80
27	Elastic Mechanical Interfacial Stresses of a Double Lap Joint with [90] Gr/Pi Adherends and no Adhesive	81
28	Elastic Mechanical Interfacial Stresses of a Double Lap Joint with [0] and [90] Gr/Pi Adherend and no Adhesive	82

Figure No.		Page
29	Elastic Curing Interfacial Stresses of a Double Lap Joint with [0] and [90] Gr/Pi Adherends and no Adhesive	83
30	Nonlinear Mechanical Adhesive τ_{yz} Stresses of a Lap Shear Joint with Aluminum Adherends and Metlbond 1113 Adhesive	88
31	Nonlinear Mechanical Adhesive γ_{yz} Strains of a Lap Shear Joint with Aluminum Adherends and Metlbond 1113 Adhesive	89
32	Comparison of Shear Stress-Strain Response of Metlbond 1113 Adhesive	92
33	Nonlinear Mechanical Adhesive σ_z Stresses of a Lap Shear Joint with Aluminum Adherends and Metlbond 1113 Adhesive	94
34	Nonlinear Mechanical Adhesive σ_y Stresses of a Lap Shear Joint with Aluminum Adherends and Metlbond 1113 Adhesive	95
35	Nonlinear Mechanical Adhesive σ_x Stresses of a Lap Shear Joint with Aluminum Adherends and Metlbond 1113 Adhesive	96
36	Nonlinear Mechanical Adhesive τ_{yz} Stresses of a Single Lap Joint with [0/90/0/90/0] B/E Adherends and AF-126-2 Adhesive	99
37	Nonlinear Mechanical Adhesive σ_z Stresses of a	

Figure No.		Page
	Single Lap Joint with [0/90/0/90/0] B/E Adherends and AF-126-2 Adhesive	100
38	Nonlinear Curing Adhesive Stresses of a Single Lap Joint with [0/90/0/90] B/E Adherends and AF-126-2 Adhesive	102
39	Nonlinear Mechanical and Curing Adhesive σ_y Stresses of a Single Lap Joint with [0/90/0/90/0] B/E Adherends and AF-126-2 Adhesive	104
40	Nonlinear Mechanical and Curing Adhesive σ_x Stresses of a Single Lap Jiont with [0/90/0/90/0] B/E Adherends and AF-126-2 Adhesive	105
41	Nonlinear Mechanical and Curing Adhesive τ_{yz} Stresses of a Single Lap Joint with [0] Gr/Pi Adherends and Metlbond 1113 Adhesive	107
42	Nonlinear Mechanical and Curing Adhesive σ_z Stresses of a Single Lap Joint with [0] Gr/Pi Adherends and Metlbond 1113 Adhesive	108
43	Nonlinear Mechanical and Curing Adhesive σ_y Stresses of a Single Lap Joint with [0] Gr/Pi Adherends and Metlbond 1113 Adhesive	109
44	Nonlinear Mechanical and Curing Adhesive τ_{yz} Stresses of a Single Lap Joint with $[\pm 45]_s$ Gr/Pi Adherends and Metlbond 1113 Adhesive	112
45	Nonlinear Mechanical and Curing Adhesive σ_z	

Figure No.		Page
	Stresses of a Single Lap Joint with $[\pm 45]_s$ Gr/Pi Adherends and Metlbond 1113 Adhesive	113
46	Nonlinear Mechanical and Curing Adhesive σ_y Stresses of a Single Lap Joint with $[\pm 45]_s$ Gr/Pi Adherends and Metlbond 1113 Adhesive	114
47	Nonlinear Mechanical and Curing Adhesive σ_x Stresses of a Single Lap Joint with $[\pm 45]_s$ Gr/Pi Adherends and Metlbond 1113 Adhesive	115
48	Nonlinear Mechanical and Curing Adhesive τ_{yz} Stresses of a Double Lap Joint with Titanium Adherends and Metlbond 1113 Adhesive	118
49	Nonlinear Mechanical and Curing Adhesive σ_z Stresses of a Double Lap Joint with Titanium Adherends and Metlbond 1113 Adhesive	119
50	Nonlinear Mechanical and Curing Adhesive σ_y Stresses of a Double Lap Joint with Titanium Adherends and Metlbond 1113 Adhesive	120
51	Nonlinear Mechanical and Curing Adhesive σ_x Stresses of a Double Lap Joint with Titanium Adherends and Metlbond 1113 Adhesive	121
52	Nonlinear Curing Adhesive Stresses of a Double Lap Joint with [0] and [90] Gr/Pi Adherends and Metlbond 1113 Adhesive	122
53	Nonlinear Mechanical and Curing Adhesive τ_{yz}	

Figure No.		Page
	Stresses of a Double Lap Joint with [0] and [90] Gr/Pi Adherends and Metlbond 1113 Adhesive	125
54	Nonlinear Mechanical and Curing Adhesive σ_z Stresses of a Double Lap Joint with [0] and [90] Gr/Pi Adherends and Metlbond 1113 Adhesive	126
55	Nonlinear Mechanical and Curing Adhesive σ_y Stresses of a Double Lap Joint with [0] and [90] Gr/Pi Adherends and Metlbond 1113 Adhesive	127
56	Nonlinear Mechanical and Curing Adhesive σ_x Stresses of a Double Lap Joint with [0] and [90] Gr/Pi Adherends and Metlbond 1113 Adhesive	128
B.1	Compression Stress-Strain Behavior of $[\pm 20]_s$ Boron/Epoxy Laminate-Sandwich Beam Data	141
B.2	Tensile Stress-Strain Behavior of $[\pm 30]_s$ B/E Laminate-Sandwich Beam Data	142
B.3	Compressive Stress-Strain Behavior of $[\pm 30]_s$ B/E Laminate-Sandwich Beam Data	143
B.4	Tensile Stress-Strain Behavior of $[\pm 45]_s$ B/E Laminate	144
B.5	Tensile Stress-Strain Behavior of $[\pm 60]_s$ B/E Laminate Sandwich Beam Data	145
B.6	Compressive Stress-Strain Behavior of $[\pm 60]_s$ B/E Laminate-Sandwich Beam Data	146

Figure No.		Page
B.7	Tensile Stress-Strain Behavior of $[0/\pm45]_s$ Bs/Al Laminate	147
C.1	Stress-Strain Response of Unidirectional Gr/Pi	149
C.2	Stress-Strain Response of $[\pm45]_s$ Laminate Gr/Pi.	150
C.3	Stress-Strain Response of $[0/\pm45/90]_s$ Laminate Gr/Pi	151
C.4	Stress-Strain Response of Unidirectional B/E Ref. [15]	152
C.5	Stress-Strain Response of [0/90/0/90/0] Laminate B/E	153
C.6	Stress-Strain Response of Metlbond 1113 Adhesive	154
C.7	Stress-Strain Response of AF-126-2 Adhesive	155

LIST OF TABLES

Table No.	Title	Page
1	Comparison of Various Boundary Conditions for Single Lap Joints	29
2	Results of Equilibrium Checks of Single Lap Joint with [0] Gr/Pi Adherends and Metlbond 1113 Adhesive	52
3	Comparison of Peak Adhesive Stresses of $[0/\pm45/90]_s$ Joint Under Mechanical Loadings for 2-Dimensional and Quasi 3-Dimensional Analysis	59
4	Force-Displacement Result Comparisons for Elastic Joint Solutions	85
5	Dimensions for Lap Shear Joint and Single Lap Joint with [0/90/0/90/0] B/E Adherends	87
6	Comparison of Numerical and Experimental Results for Lap Shear Joint	91
7	Comparison of Elastic and Nonlinear Adhesive Stresses for a Single Lap Joint with [0] Gr/Pi Adherends and Metlbond 1113 Adhesive	100
8	Comparison of Elastic and Nonlinear Adhesive Stresses for a Single Lap Joint with $[\pm45]_s$ Gr/Pi Adherends and Metlbond 1113 Adhesives	111

Table No.	Title	Page
9	Comparison of Elastic and Nonlinear Adhesive Stresses for a Double Lap Joint with Ti Adherends and Metlbond 1113 Adhesive	117
10	Comparison of Elastic and Nonlinear Adhesive Curing Stresses for a Double Lap Joint with [0] and [90] Gr/Pi Adherends and Metlbond 1113 Adhesive	124
C-1	Ramberg-Osgood Coefficients	156
C-2	Thermal Properties	162

Chapter 1

INTRODUCTION

With the development of advanced fiber reinforced composites as viable structural materials the adhesive bonded joint has become of primary importance. The bonded joint does not require that the structural members being joined (adherends) be perforated to facilitate bolts. Without the bolt holes and the stress concentrations associated with them, a substantial weight savings can be realized which is a major reason for selecting composite materials for the structural component.

In order to fully realize the strength of the composite adherends, the adhesive bonded joint must be efficiently designed and this requires an adequate prediction of the stress distributions in the adhesive layer of the joint. The study of stresses in the adhesive layer has been approached by researchers in the past using one of two types of analysis procedures.

Many researchers have attempted to predict the stresses using a closed form analytical solution. However, when using this approach, the equations that need to be solved become exceedingly complicated and this leads to the need for simplifying assumptions. These assumptions have included linearity, material isotropy, restrictions on the geometry of the joint, and neglect of thermal effects.

Other researchers have approached the problem through the use of numerical techniques such as finite element analysis. They have usually found it necessary to use some or all of the assumptions made for the

closed form type solution procedure. The motivation for the present study is to show the capability of a finite element computer analysis program developed by Renieri and Herakovich [1] to adequately predict these stress fields. The program has the capability for material orthotropy, material nonlinearities, and temperature dependent properties. Modifications to the computer program for this study include increased element capacity, improved execution time, and capability for hygrothermal analysis.

Chapter 2

LITERATURE SURVEY

The first investigation into the behavior of bonded joints found in the literature was presented in 1944 by Goland and Reissner [2]. They obtained an analytical solution by assuming a state of plane strain, prescribing the distributions of the shear and peel stresses to be parabolic and linear, respectively, and applying restrictions on the ratios of adherend moduli and thickness to adhesive modulus and thickness. The solution is based on the principle of minimum potential energy and is restricted to linear isotropic materials and identical adherends. Thermal effects were neglected for this analysis.

Erdogan and Ratwani [3] approached the problem of an orthotropic plate bonded to an isotropic plate with an isotropic adhesive. They obtained closed form solutions for stepped lap and smoothly tapered joints. Their solution was based on a summation of forces in the adhesive layer and adherends and assumed plane stress and linear material behavior. This solution predicted stress singularities at the edges of each step in the adhesive in the stepped lap joint, and at the ends of the overlap in the adhesive for the smoothly tapered joint.

Barker and Hatt [4] used a linear elastic finite element computer analysis program to compare results with the work of Erdogan and Ratwani [3]. The adherends were modeled using four noded isoparametric elements and material orthotropy was considered. The adhesive layer was modeled using a special element developed for that purpose which was formulated

to have no thickness and used modified stiffnesses derived from the moduli, thickness, and length of the adhesive layer. Their results compared favorably with Erdogan and Ratwani.

Sainsbury-Carter [5] solved the stepped and linearly tapered bonded joints by assuming linear isotropic materials and solving the equations of equilibrium. It was assumed that the moduli of the adherends are much larger than those of the adhesive. Also the analysis was one-dimensional and thermal effects were neglected. It was shown that the thickness of the adherends greatly affected the magnitude of the peak shear and peel stresses and an iterative technique was developed to modify these thicknesses within stress design criteria.

Wah [6] investigated non-symmetric single lap joints with composite adherends and isotropic adhesives. Laminated plate theory was used to develop stress and moment resultants and relate them to mid-plane strains and curvatures. The laminated adherends were required to be mid-plane symmetric in order to uncouple the bending-stretching terms in the previously mentioned relationships. A solution was presented for the joints under shear loadings as well as axial loads. The solutions were restricted to the elastic range and thermal effects were neglected.

Hart-Smith [7] was the first researcher to consider the non-linearity of the adhesive layer by assuming its stress-strain response to be elastic-perfectly plastic. This effort presents solutions and design aids, including thermal effects, for single, double and stepped lap joints and linear tapered joints. While a thermal mismatch is considered all material properties are considered temperature indepen-

dent. This research notes the increased failure strength by allowing for plastic deformation in the adhesive.

A comparison of theoretical and experimental shear stress in a single lap joint was presented by Sharpe and Muha [8]. The joint modeled had plexiglass adherends and an epoxy adhesive. Good correlation was obtained with the work of Goland and Reissner [2] and with a linear computer analysis program, BOND4, of the University of Delaware.

Renton and Vinson [9-10] performed parametric studies on single lap joints as well as fatigue testing and thick adherend lap shear testing. The specimens were comprised of mid-plane symmetric composite adherends and elastic behavior only was studied. Linear thermal effects were also included. The parameters studied were over-lap length, adhesive thickness, and ply orientation in the composite adherends. Comparisons were made with the work of Goland and Reissner [2] with Renton and Vinson's work showing better satisfaction of stress free boundary condition at the edge of the adhesive layer.

Grimes, Greimann et al [11] approached the analysis of single, double, and stepped lap joints from both the finite element method and numerical integration of the governing differential equations. Their analysis included full material nonlinearity in the adherends and adhesive layer. The development for both solutions was based on the deformation theory of plasticity with the finite element analysis utilizing an iterative procedure until the solution converged. In both forms of analysis, solutions were presented for room temperature only and curing stresses were neglected.

DasGupta and Sharma [12] used an analysis similar to Goland and Reissner [2] to predict stresses in lap joints with prebent adherends. The work showed a decrease in peak stresses with the use of bent adherends.

Renton [13] provided an analysis of the thick adherend lap shear test using the work of Renton and Vinson [9-10]. This research verified the validity of the test.

Other researchers have investigated the effects of moisture [14], and the reliability [15] of lap joints.

While this survey is by no means all-inclusive, it is representative of the research that has been performed and from this survey the need for fully-nonlinear material behavior and temperature dependent properties can be seen as these physical realities have been consistently neglected.

Chapter 3

BASIC CONSIDERATIONS

The bonded joints selected for analysis in this study are single and double lap joints with and without adhesive layers. Typical geometries for joints with adhesive layers are shown in Figure 1. Composite and isotropic adherends are considered with nonlinear material properties and thermal stresses as well as temperature dependent properties. Hygroscopic analysis capabilities are presented but no results are included in this investigation due to a lack of complete consistent data.

3.1 Geometric Restrictions

For the present study it is assumed that the joint is in a state of plane strain (i.e. $\varepsilon_x = 0$, or $\varepsilon_x = \text{const}$). This is a valid assumption if the x dimension of the joint (Fig. 1) is large and the cross-section under consideration is some distance removed from contraints that are dependent upon the x coordinate.

The analysis is also restricted to balanced, mid-plane symmetric composite adherends and laminate material properties are used for these components.

3.2 Quasi 3-Dimensional Analysis

The analysis of reference [1] considers a long prismatic bar under the influence of a uniform applied strain or temperature change to have strains independent of the x coordinate. With this assumption, the

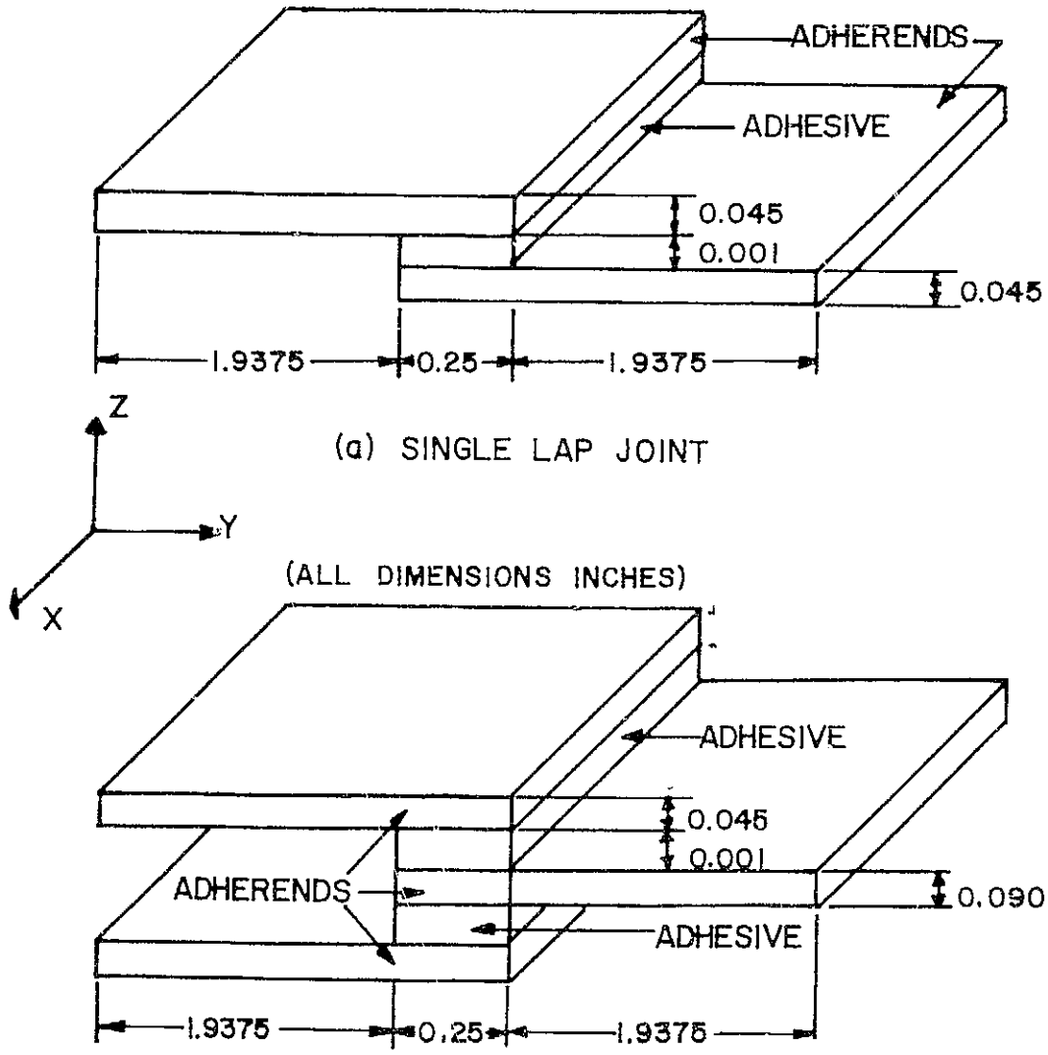

(a) SINGLE LAP JOINT

(b) DOUBLE LAP JOINT

Figure 1. Lap Joint Geometries

strain displacement relations can be written as

$$\varepsilon_x = \frac{\partial u}{\partial x} = f_1(y,z), \quad \varepsilon_y = \frac{\partial v}{\partial y} = f_2(y,z)$$

$$\varepsilon_z = \frac{\partial w}{\partial z} = f_3(y,z), \quad \gamma_{yz} = \frac{\partial v}{\partial z} + \frac{\partial w}{\partial y} = f_4(y,z) \tag{3.1}$$

$$\gamma_{xz} = \frac{\partial u}{\partial z} + \frac{\partial w}{\partial x} = f_5(y,z), \quad \gamma_{xy} = \frac{\partial u}{\partial y} + \frac{\partial v}{\partial x} = f_6(y,z)$$

where u, v, and w are x, y, and z displacements, respectively, and f_1 through f_6 are unknown functions of y and z coordinates only. With the use of suitable mathematical manipulation, (3.1) can be integrated yielding the following form for the displacement fields

$$\begin{aligned} u(x,y,z) &= x(C_1y+C_2z+C_3) + U(y,z) \\ v(x,y,z) &= x(C_4z+C_6) - C_1\frac{x^2}{2} + V(y,z) \\ w(x,y,z) &= x(-C_4y+C_5) - C_2\frac{x^2}{2} + W(y,z) \end{aligned} \tag{3.2}$$

where C_1 through C_6 are unknown constants and U, V, and W are unknown functions of y and z only. With this assumption, and neglecting body forces, the equilibrium equations can be written as

$$\begin{aligned} \frac{\partial \tau_{xy}}{\partial y} + \frac{\partial \tau_{xz}}{\partial z} &= 0 \\ \frac{\partial \sigma_y}{\partial y} + \frac{\partial \tau_{yz}}{\partial z} &= 0 \\ \frac{\partial \tau_{yz}}{\partial y} + \frac{\partial \sigma_z}{\partial z} &= 0 \end{aligned} \tag{3.3}$$

3.3 Bonded Joints

The analysis developed in [1] can be used as two different formulations for the solution of bonded joints. The first of these corresponds to a classical plane strain solution in which $\varepsilon_x = \gamma_{xz} = \gamma_{xy} = 0$. This type of solution is entirely 2-dimensional and is the type of plane strain analysis used in a majority of joint analyses previously in the literature.

The second formulation is a more general plane strain solution where $\varepsilon_x \neq 0$ but is equal to some constant ε_x. For this procedure the components of strain γ_{xz} and γ_{xy} are assumed to be zero. The principal difference between the two formulations is that the second accounts for the transverse stiffness (E_x) of the adherends and adhesive while the first does not. This second formulation is used for this analysis and comparisons between results obtained from the two solutions are presented in Chapter 5. In the following sections and chapters the first formulation is referred to as a 2-dimensional formulation while the second is referred to as a quasi 3-dimensional analysis as it corresponds closely to the analysis of section 3.2.

3.3.1 2-Dimensional Joint Formulation

In the classic plane strain solution the displacements, strains, and therefore stresses, are independent of the x-coordinate (Fig. 1). Under these assumptions the displacement fields (Equ. 3.2) reduce to

$$\begin{aligned} u &= 0 \\ v &= V(y,z) \\ w &= W(y,z) \end{aligned} \tag{3.4}$$

The nonzero strain components (ε_y, ε_z and γ_{yz}) have the same definitions as in Equ's. (3.1).

3.3.2 Quasi 3-Dimensional Joint Formulation

If, in a bonded joint, it can be assumed that ε_x is a nonzero constant and that γ_{xz} and γ_{xy} are zero, then the displacement fields (Equ's. 3.2) reduce to

$$\begin{aligned} u &= \xi_x x \\ v &= V(y,z) \\ w &= W(y,z) \end{aligned} \tag{3.5}$$

In these equations the only nonzero constant from Equ's. (3.2), C_3, has been renamed ξ_x and corresponds to the uniform normal strain ε_x. The remaining strain components (ε_y, ε_z, and γ_{yz}) again have the same form as in Equ's. (3.1).

The assumption that the strain component normal to the plane of the analysis is constant is strictly valid for the case of single lap joints with identical orthotropic adherends. It is also valid for double lap joints where the outer adherends are identical and exhibit orthotropy. The assumptions that $\gamma_{xz} = \gamma_{xy} = 0$ are valid if the adherends are orthotropic.

The restriction that all adherends be orthotropic is satisfied by all joints analyzed in this study. It should be noted however that two of the joints analyzed do not satisfy the first condition as they are single lap joints with differing adherends.

For these joints, the solution neglects the effects of bending out of the plane of the joint and is similar to a membrane solution in this respect.

3.4 Material Properties

In order to adequately model a layered adherend layer by layer an excessive number of finite elements would be needed. Because of this, it is necessary to use laminate material properties and consider the composite adherends to be homogeneous orthotropic materials for the joint analysis.

Obtaining laminate material properties from the literature proved to be impossible thus making it necessary to generate these properties analytically. For this generation of properties two different approaches were used. The stress-strain response of a laminate was predicted following the work of Renieri and Herakovich [1], while thermal properties were predicted using classical lamination theory.

3.4.1 Prediction of Laminate Stress-Strain Response

The details of the analysis of ref. [1] will not be presented as to do so would be overly repetitious; however a brief outline will be presented for completeness.

The analysis utilizes the displacement fields of Equ's. (3.2). Because the laminates in question are balanced and midplane symmetric the analysis can be reduced to the quarter section shown in Figure (2b) with certain symmetry and anti-symmetry conditions. The displacement

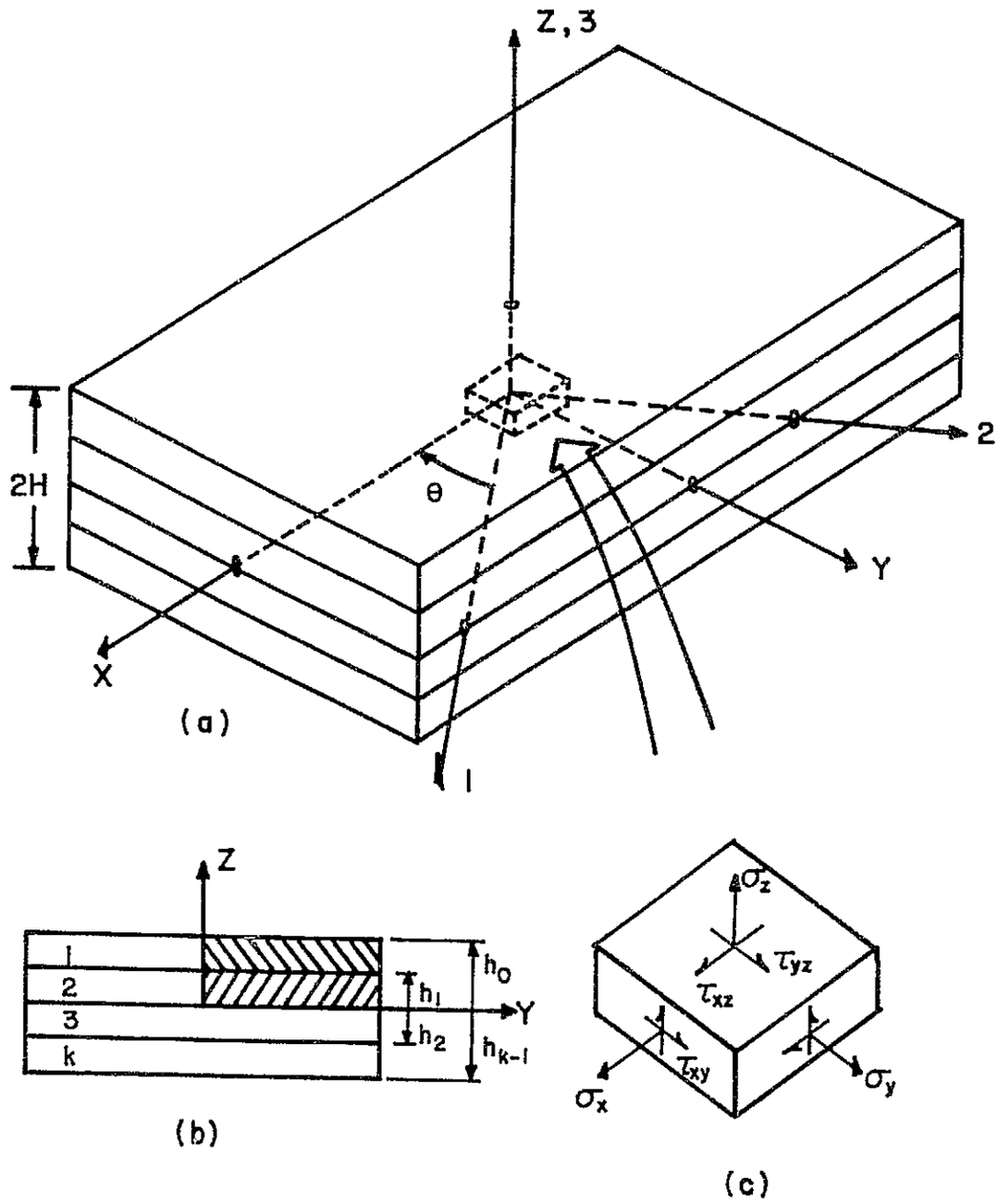

Figure 2. Laminate Geometry

fields (Equ's. 3.2) reduce to

$$
\begin{aligned}
u &= \varepsilon_x x + U(y,z) \\
v &= V(y,z) \\
w &= W(y,z)
\end{aligned}
\tag{3.6}
$$

and again the constant C_3 has been renamed ε_x and corresponds to a uniform applied strain. The displacement fields (3.6) along with the stress-free boundary conditions along the free edges, top and bottom surfaces and certain restrictions imposed upon the displacements by the symmetry and anti-symmetry conditions mentioned previously represent the boundary value problem to be solved by the finite element analysis. With this analysis and the nonlinear finite element program, the moduli E_{xx} and E_{yy} can be predicted as functions of strain level.

3.4.2 Prediction of Laminate Thermal Properties

Laminate thermal properties including coefficients of thermal expansion and moduli as functions of temperature are predicted using lamination theory and unidirectional material properties as functions of temperature. Lamination theory as presented here cannot directly predict temperature dependent laminate properties, however, if the unidirectional properties used as input correspond to an elevated temperature, then the laminate properties generated will also correspond to this temperature. Therefore, laminate properties can be predicted at discrete temperatures corresponding to the input data.

The constitutive relations for a single, orthotropic lamina in the principal material coordinates are

$$\begin{Bmatrix} \sigma_1 \\ \sigma_2 \\ \sigma_3 \\ \tau_{23} \\ \tau_{13} \\ \tau_{12} \end{Bmatrix} = \begin{bmatrix} C_{11} & C_{12} & C_{13} & 0 & 0 & 0 \\ C_{12} & C_{22} & C_{23} & 0 & 0 & 0 \\ C_{13} & C_{23} & C_{33} & 0 & 0 & 0 \\ 0 & 0 & 0 & C_{44} & 0 & 0 \\ 0 & 0 & 0 & 0 & C_{55} & 0 \\ 0 & 0 & 0 & 0 & 0 & C_{66} \end{bmatrix} \begin{Bmatrix} \varepsilon_1 \\ \varepsilon_2 \\ \varepsilon_3 \\ \gamma_{23} \\ \gamma_{13} \\ \gamma_{12} \end{Bmatrix} \tag{3.7}$$

where the principal coordinates are shown in Fig. 2a as the 1-2-3 system. These equations can be written in an abbreviated form as

$$\{\sigma\}_1 = [C]\{\varepsilon\}_1 \tag{3.8}$$

For a coordinate rotation about the 3 axis through an angle θ (Fig. 2a) the stresses and strains are transformed according to the following relations,

$$\{\sigma\}_x = [T_1]\{\sigma\}_1 \text{ and } \{\varepsilon\}_x = [T_2]\{\varepsilon\}_1 \tag{3.9}$$

where

$$\{\sigma\}_x = \begin{Bmatrix} \sigma_x \\ \sigma_y \\ \sigma_z \\ \tau_{yz} \\ \tau_{xz} \\ \tau_{xy} \end{Bmatrix}, \quad [T_1] = \begin{bmatrix} m^2 & n^2 & 0 & 0 & 0 & 2mn \\ n^2 & m^2 & 0 & 0 & 0 & -2mn \\ 0 & 0 & 1 & 0 & 0 & 0 \\ 0 & 0 & 0 & m & -n & 0 \\ 0 & 0 & 0 & n & m & 0 \\ -mn & mn & 0 & 0 & 0 & (m^2-n^2) \end{bmatrix}$$

$$\{\varepsilon\}_x = \begin{Bmatrix} \varepsilon_x \\ \varepsilon_y \\ \varepsilon_z \\ \gamma_{yz} \\ \gamma_{xz} \\ \gamma_{xy} \end{Bmatrix}, \quad [T_2] = \begin{bmatrix} m^2 & n^2 & 0 & 0 & 0 & mn \\ n^2 & m^2 & 0 & 0 & 0 & -mn \\ 0 & 0 & 1 & 0 & 0 & 0 \\ 0 & 0 & 0 & m & -n & 0 \\ 0 & 0 & 0 & n & m & 0 \\ -2mn & 2mn & 0 & 0 & 0 & (m^2-n^2) \end{bmatrix}$$

and $m = \cos\theta$, $n = \sin\theta$

Combining Equ's. (3.8) and (3.9) yields

$$\{\sigma\}_x = [T_1][C][T_2]^{-1}\{\varepsilon\}_x$$

or

$$\{\sigma\}_x = [\bar{C}]\{\varepsilon\}_x \tag{3.10}$$

where $[\bar{C}]$ is defined as

$$[\bar{C}] = [T_1][C][T_2]^{-1} \tag{3.11}$$

and has the form

$$[\bar{C}] = \begin{bmatrix} \bar{C}_{11} & \bar{C}_{12} & \bar{C}_{13} & 0 & 0 & \bar{C}_{16} \\ \bar{C}_{12} & \bar{C}_{22} & \bar{C}_{23} & 0 & 0 & \bar{C}_{26} \\ \bar{C}_{13} & \bar{C}_{23} & \bar{C}_{33} & 0 & 0 & \bar{C}_{36} \\ 0 & 0 & 0 & \bar{C}_{44} & \bar{C}_{45} & 0 \\ 0 & 0 & 0 & \bar{C}_{45} & \bar{C}_{55} & 0 \\ \bar{C}_{16} & \bar{C}_{26} & \bar{C}_{36} & 0 & 0 & \bar{C}_{66} \end{bmatrix} \tag{3.12}$$

Equ's. (3.10) are the constitutive relations for an orthotropic lamina rotated through an angle θ.

For lamination theory it is assumed that a lamina is in a state of plane stress. It should be noted that this lamination theory development is the only case in which plane stress will apply while plane strain is assumed in all other developments.

The mathematical statement of the plane stress assumption is

$$\sigma_z = \tau_{xz} = \tau_{yz} \equiv 0 \tag{3.13}$$

which can be used to reduce the constitutive relations (Equ's. 3.7) to

$$\begin{Bmatrix} \sigma_1 \\ \sigma_2 \\ \tau_{12} \end{Bmatrix} = \begin{bmatrix} Q_{11} & Q_{12} & 0 \\ Q_{12} & Q_{22} & 0 \\ 0 & 0 & Q_{66} \end{bmatrix} \begin{Bmatrix} \varepsilon_1 \\ \varepsilon_2 \\ \gamma_{12} \end{Bmatrix} \tag{3.14}$$

This simplified form of the stiffness matrix [C] is known as the reduced stiffness matrix [Q].

If the transformation matrices (Equ's. 3.9) are reduced similarly, a rotated plane stress constitutive relation $[\bar{Q}]$ can be formed in the same manner as Equ's. (3.10). Thus

$$\{\sigma\}_x = [\bar{Q}]\{\varepsilon\}_x \tag{3.15}$$

where

$$\{\sigma\}_x = \begin{Bmatrix} \sigma_x \\ \sigma_y \\ \tau_{xy} \end{Bmatrix}, \ \{\varepsilon\}_x = \begin{Bmatrix} \varepsilon_x \\ \varepsilon_y \\ \gamma_{xy} \end{Bmatrix}, \text{ and } [\bar{Q}] = \begin{bmatrix} \bar{Q}_{11} & \bar{Q}_{12} & \bar{Q}_{16} \\ \bar{Q}_{12} & \bar{Q}_{22} & \bar{Q}_{26} \\ \bar{Q}_{16} & \bar{Q}_{26} & \bar{Q}_{66} \end{bmatrix}$$

Now, taking the standard plate theory assumption that normals to the mid-plane of the plate remain normal after loading, the strains of Equ's. (3.15) may be written as

$$\{\varepsilon\}_x = \{\varepsilon^\circ\} + z\{\kappa\} \tag{3.16}$$

where

$$\{\varepsilon\}_x = \text{total strains}$$

$$\{\varepsilon^\circ\} = \begin{Bmatrix} \varepsilon_x^\circ \\ \varepsilon_y^\circ \\ \gamma_{xy}^\circ \end{Bmatrix} = \text{mid-plane strains}$$

$$\{\kappa\} = \begin{Bmatrix} \kappa_x \\ \kappa_y \\ \kappa_{xy} \end{Bmatrix} = \text{plate curvatures}$$

and z = distance from the mid-plane

Defining stress resultants

$$\{N\} = \begin{Bmatrix} N_x \\ N_y \\ N_{xy} \end{Bmatrix} = \int_{-H}^{H} \begin{Bmatrix} \sigma_x \\ \sigma_y \\ \tau_{xy} \end{Bmatrix} dz \tag{3.17}$$

and combining Equ's. (3.15), (3.16), and (3.17) yields

$$\{N\} = \int_{-H}^{H} [\bar{Q}]\{\varepsilon^\circ\}dz + \int_{-H}^{H} [\bar{Q}]z\{\kappa\}dz \tag{3.18}$$

or

$$\{N\} = [A]\{\varepsilon^{\circ}\} + [B]\{\kappa\} \tag{3.19}$$

where

$$[A] = \sum_{k=1}^{N} [\bar{Q}]^{(k)}(h_k - h_{k-1}) \tag{3.20}$$

and

$$[B] = \frac{1}{2} \sum_{k=1}^{N} [\bar{Q}]^{(k)}(h_k^2 - h_{k-1}^2)$$

where the k denotes the number of the ply and the h's are as in Fig. 2b.

For symmetric lamiantes [B] = 0 and

$$\{N\} = [A]\{\varepsilon^{\circ}\} \tag{3.21}$$

Inverting this relationship yields

$$\{\varepsilon^{\circ}\} = [A]^{-1}\{N\} \tag{3.22}$$

Noting that

$$\{\bar{\sigma}\}_x = \frac{1}{2H}\{N\} \tag{3.23}$$

and combining Equ's. (3.22) and (3.23), leads to

$$\{\varepsilon^{\circ}\} = [a^*]\{\bar{\sigma}\} \tag{3.24}$$

where

$$[a^*] = 2H[A]^{-1}$$

These relations can be used to define the laminate properties

$$E_x = \frac{\bar{\sigma}_x}{\varepsilon_x^o} = \frac{1}{a_{11}^*}$$

$$E_y = \frac{\bar{\sigma}_y}{\varepsilon_y^o} = \frac{1}{a_{22}^*}$$

$$G_{xy} = \frac{\bar{\tau}_{xy}}{\gamma_{xy}^o} = \frac{1}{a_{66}^*} \tag{3.25}$$

$$\nu_{xy} = \frac{-\varepsilon_y^o}{\varepsilon_x^o} = \frac{-a_{12}^*}{a_{11}^*}$$

For an orthotropic material the coefficients of thermal expansion are

$$\{\alpha\}_1 = \begin{Bmatrix} \alpha_1 \\ \alpha_2 \\ \alpha_3 \\ 0 \\ 0 \\ 0 \end{Bmatrix} \tag{3.26}$$

These coefficients transform, under the rotation defined earlier, in the same manner as the strains (Equ. 3.9).

$$\{\alpha\}_x = [T_2]\{\alpha\}_1 \tag{3.27}$$

For the 2-dimensional analysis Equ. (3.27) reduces to

$$\begin{Bmatrix} \alpha_x \\ \alpha_y \\ \alpha_{xy} \end{Bmatrix} = \begin{Bmatrix} m^2\alpha_1 + n^2\alpha_2 \\ n^2\alpha_1 + m^2\alpha_2 \\ 2mn(\alpha_1-\alpha_2) \end{Bmatrix} \tag{3.28}$$

Now define laminate coefficients of thermal expansion such that

$$\{\varepsilon^\circ\} = \{\bar{\alpha}\}\Delta T \tag{3.29}$$

where ΔT is a uniform temperature change and

$$\{\bar{\alpha}\} = \begin{Bmatrix} \bar{\alpha}_x \\ \bar{\alpha}_y \\ \bar{\alpha}_{xy} \end{Bmatrix}$$

Combining Equ's. (3.18), (3.22), and (3.29), and considering symmetric laminates only yields

$$\{\varepsilon^\circ\} = \{\bar{\alpha}\}\Delta T = [A]^{-1}\int_{-H}^{H} [\bar{Q}]\{\alpha\}dz\Delta T \tag{3.30}$$

or

$$\{\bar{\alpha}\} = [A]^{-1} \sum_{k=1}^{N} [\bar{Q}]^k\{\alpha\}^k(h_k-h_{k-1}) \tag{3.31}$$

When the moduli and thermal coefficients used to calculate the [C] matrix (Equ's. 3.7) are those corresponding to an elevated temperature, then the moduli of Equ's. (3.25) and coefficients of expansion of Equ's. (3.31) will be laminate properties also corresponding to that tempera-

ture. These reduced moduli will be used as input in the finite element program.

These methods of generating material properties were resorted to because of the lack of consistent experimental data found in the literature.

3.5 Finite Element Formulation

As in section 3.2.1 the presentation of the complete formulation would be a duplication of the work of Renieri and Herakovich [1], therefore only the highlights will be given here.

The finite element solution process involves the subdivision of a structure into a finite number of smaller elements (Fig. 3). This process is known as discretization. For each of these finite elements a set of interpolation functions are chosen to represent the displacements at any point in the element as functions of the displacements at the corners or nodes of the element. Using the strain-displacement relations (Equ. 3.1) the strains can also be calculated as functions of nodal displacements. Now with the use of a variational principle, such as the principle of minimum potential energy, a set of equations relating nodal forces to nodal displacements can be obtained for each element,

$$\{F\}^{(\ell)} = [K]^{(\ell)}\{u\}^{(\ell)} \tag{3.32}$$

where $\{F\}$ = nodal forces

$\{u\}$ = nodal displacements

$[K]$ = element stiffness matrix

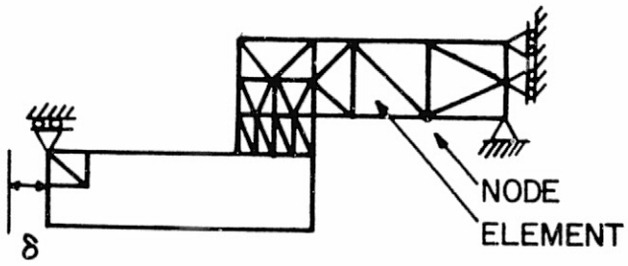

(a) SINGLE LAP JOINT

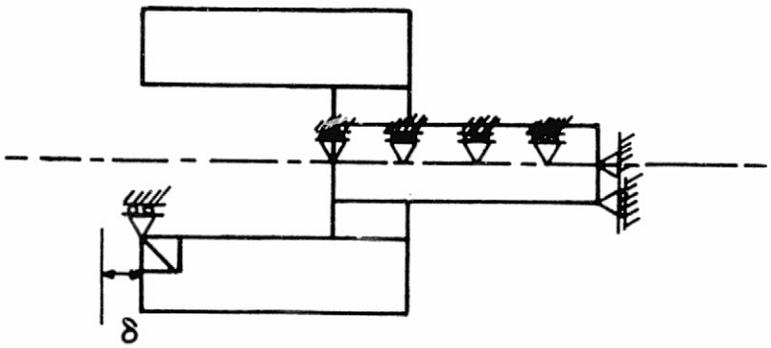

(b) DOUBLE LAP JOINT

Figure 3. Joint Boundary Conditions

and the superscript (ℓ) refers to the individual element. These elemental relations (Equ's. 3.32) are then combined or assembled into a larger system of equations relating forces to displacements for the entire structure. The solution of these equations yields the displacements and therefore the strains and stresses over the entire body.

The finite element scheme developed by Renieri and Herakovich [1] utilizes the constant-stress, constant-strain triangular element with three nodes. The interpolation functions used are

$$u = a_1 + a_2 y + a_3 z + \varepsilon_x x$$

$$v = a_4 + a_5 y + a_6 z \tag{3.33}$$

$$w = a_7 + a_8 y + a_9 z$$

As can be seen from the form of Equ's. (3.33) these are linear relations and will yield constant strains when substituted into Equ's. (3.1). The constants a_1 through a_9 are functions of the spatial coordinates and nodal displacements of the individual elements and ε_x is the applied uniform strain.

Manipulation of Equ's. (3.33) and substitution into Equ. (3.1) yields the following strain-displacement relations for an element.

$$\begin{Bmatrix} \varepsilon_x \\ \varepsilon_y \\ \varepsilon_z \\ \gamma_{yz} \\ \gamma_{xz} \\ \gamma_{xy} \end{Bmatrix} = \frac{1}{A} \begin{Bmatrix} \varepsilon_x A \\ av_1 + cv_2 + ev_3 \\ bw_1 + dw_2 + gw_3 \\ bv_1 + dv_2 + gv_3 + aw_1 + cw_2 + ew_3 \\ bu_1 + du_2 + gu_3 \\ au_1 + cu_2 + eu_3 \end{Bmatrix} \tag{3.34}$$

where A = area of the element

u_1, u_2, u_3 = x-displacements at nodes 1, 2, and 3 respectively

v_1, v_2, v_3 = y-displacements at nodes 1, 2, and 3 respectively

w_1, w_2, w_3 = z-displacements at nodes 1, 2, and 3 respectively

and a, b, c, d, e, g are known constants involving spatial coordinates only.

For the case of a uniform thermal load the strains are

$$\{\varepsilon\}_1 = \{\varepsilon^*\}_1 - \{\varepsilon^T\}_1 \tag{3.35}$$

where $\{\varepsilon^*\}_1$ = total strain

$\{\varepsilon\}_1$ = mechanical strain

and $\{\varepsilon^T\}_1$ = thermal strain

which consists of $\{\alpha\}_1$ (Equ. 3.26) multiplied by the temperature change ΔT. Transforming Equ's. (3.35) to an arbitrary coordinate system yields an individual element.

$$\{\varepsilon\}_x = \{\varepsilon^*\}_x - [T_2]\{\varepsilon^T\}_1 \tag{3.36}$$

Noting Equ's. (3.34), these strains can be written as

$$\begin{Bmatrix} \varepsilon_x \\ \varepsilon_y \\ \varepsilon_z \\ \gamma_{yz} \\ \gamma_{xz} \\ \gamma_{xy} \end{Bmatrix} = \begin{Bmatrix} \xi_x - (m^2\alpha_1 + n^2\alpha_2)\Delta T \\ (av_1 + cv_2 + ev_3)/A - (n^2\alpha_1 + m^2\alpha_2)\Delta T \\ (bw_1 + dw_2 + gw_3)/A - \alpha_3\Delta T \\ (bv_1 + dv_2 + gv_3 + aw_1 + cw_2 + ew_3)/A \\ (bu_1 + du_2 + gu_3)/A \\ (au_1 + cu_2 + eu_3)/A + 2mn\Delta T(\alpha_1-\alpha_2) \end{Bmatrix} \tag{3.37}$$

The preceding formulation for thermal strains is completely analogous for that of hygroscopic strains. For an orthotropic material the coefficients of hygrosopic expansion are

$$\{\beta\}_1 = \begin{Bmatrix} \beta_1 \\ \beta_2 \\ \beta_3 \\ 0 \\ 0 \\ 0 \end{Bmatrix} \tag{3.38}$$

Following exactly the development of Equ's. (3.35) through (3.37) and substituting $\{\beta\}_1$ for $\{\alpha\}_1$ and ΔM for ΔT where ΔM is a uniform percent weight change due to moisture absorption or desorbtion, yields

$$\begin{Bmatrix} \varepsilon_x \\ \varepsilon_y \\ \varepsilon_z \\ \gamma_{yz} \\ \gamma_{xz} \\ \gamma_{xy} \end{Bmatrix} = \begin{Bmatrix} \xi_x - (m^2\beta_1 + n^2\beta_2)\Delta M \\ (av_1 + cv_2 + ev_3)/A - (n^2\beta_1 + m^2\beta_1)\Delta M \\ (bw_1 + dw_2 + gw_3)/A - \beta_3\Delta M \\ (bv_1 + dv_2 + gv_3 + aw_1 + cw_2 + ew_3)/A \\ (bu_1 + du_2 + gu_3)/A \\ (au_1 + cu_2 + eu_3)/A + 2mn\Delta M(\beta_1 - \beta_2) \end{Bmatrix} \tag{3.39}$$

The hygroscopic expressions are presented here because the capability for this type of analysis has been included in the computer program. Results will not be presented because of the lack of data as stated earlier. It should also be noted that the derivation is for a uniform temperature or moisture change and that analysis should be limited to cases where uniformity is a valid assumption.

The principle of minimum potential energy states that a body is in equilibrium when the total potential energy ψ is minimum where

$$\psi = U_e + W_e, \tag{3.40}$$

U_e = internal strain energy

and

W_e = potential energy of the applied loads

The internal strain energy for an element is

$$U_e = \frac{1}{2}\int \{\varepsilon\}^T[\bar{C}]\{\varepsilon\}dVol \tag{3.41}$$

which for an element with constant strains and unit thickness reduces to

$$U_e = \frac{A}{2} \{\varepsilon\}^T [\bar{C}] \{\varepsilon\} \tag{3.42}$$

In both Equ's. (3.41) and (3.42) the strains involved depend upon whether the loading is mechanical (Equ's. 3.34), thermal (Equ's. 3.37) or hygroscopic (Equ's. 3.39). The potential energy of the applied loads is given by the negative of the applied forces multiplied by their respective displacements.

Minimization of Equ's. (3.40) with respect to displacements yield the elemental stiffness matrix plus strain, thermal and hygrosopic related vectors. The forms for these can be found in Appendix A.

3.6 Boundary Conditions for Joints

The boundary conditions applied to single and double lap joints for the present study are shown in Fig. 3. A number of different boundary conditions and loadings were investigated and comparisons were made. These are summarized in Table 1. Noting Table 1 it is seen that all conditions except the fourth yield comparable results. The lower peak stresses for this condition can be attributed to an overly flexible model. It was reasoned that this does not correspond to physical reality as a real joint would not be free to deflect up and down where the loading is applied. The first set of conditions was eliminated from consideration as they can only be applied to symmetric single lap joints. The second set was eliminated because during the solution process a negative diagonal in the global stiffness matrix was encountered. The third set of conditions was disregarded because the stress distribution in the

TABLE 1

Comparison of Various Boundary Conditions for Symmetric Single Lap Joints

Type of Constraint and Loading	Numerically Stable	Symmetric Stress Distribution	Applied Load	Max τ_{yz}	Max σ_y	Max σ_z	Max End Displacement
1 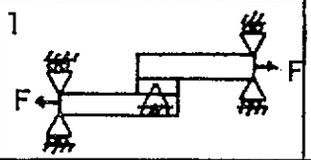	Yes	Yes	300 (lbs)	2.39 (KSI)	.84 (KSI)	1.13 (KSI)	$.91 \times 10^{-3}$ $.82 \times 10^{-3}$ (in)
2 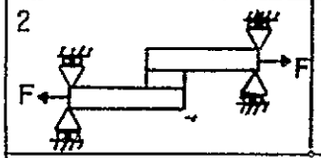	No	Yes	300 (lbs)	2.39 (KSI)	.84	1.13	$.91 \times 10^{-3}$ $.82 \times 10^{-3}$
3 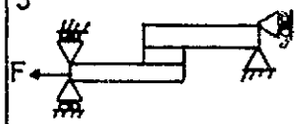	Yes	No	300 (lbs)	2.52 2.25 (KSI)	.97 .72 (KSI)	1.32 .93 (KSI)	$.179 \times 10^{-2}$ $.165 \times 10^{-2}$ (in)
4 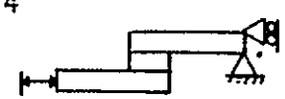	Yes	Yes	$.165 \times 10^{-2}$ (in)	1.91	.66	.88	$.165 \times 10^{-2}$ $.165 \times 10^{-2}$
5 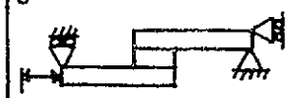	Yes	Yes	$.165 \times 10^{-2}$ (in)	2.32 (KSI)	.83 (KSI)	1.11 (KSI)	$.165 \times 10^{-2}$ $.165 \times 10^{-2}$

adhesive layer was not symmetric for a symmetric joint while it is intuitively obvious that it should be. The fifth set of constraints and loading was chosen because it provided symmetric results, numerical stability and is applicable to nonsymmetric joints.

3.7 Qualifying Notes

Due to the lack of data present in the literature a number of assumptions concerning material properties have been made. For lamina data input, it is assumed that E_{22} is identical to E_{33}. It is also assumed that the three shear moduli G_{12}, G_{13} and G_{23} are identical. Poisson ratios are considered constant and percent modulus retentions are assumed identical in tension and compression

When inputting laminate material properties, much of the data is generated according to the analyses presented earlier. It is assumed that the σ_z-ε_z laminate response is identical to the σ_2-ε_2 response of a unidirectional lamina. It is also assumed that the τ_{yz}-γ_{yz} and τ_{xz}-γ_{xz} curves are the same as the τ_{12}-γ_{12} response of a lamina and that the laminate poisson ratios ν_{xz} and ν_{yz} are the same as the lamina poissons ratios ν_{13} and ν_{23}, respectively. Other restrictions are the same as for lamina data.

It should be mentioned here that the material properties used in this analysis (Appendix C) are not consistent. The data has been taken from a number of sources and is not all realted to identical material systems. Even with these limitations it is felt that the investigation still fulfills its goal of showing the capability to analyze joints if consistent properties were available.

Chapter 4

NONLINEAR ANALYSIS

A significant portion of the research effort involved in this study was devoted to the modification of the finite element analysis program NONCOM [1]. The improved version, NONCOM1 will be briefly described here.

4.1 Modifications of NONCOM1

For the analysis of bonded joints, a number of modifications to the existing finite element program were implemented. These included:

(1) Increased finite element capacity

(2) Inclusion of a more efficient equation solver

(3) Capability for input of fully 3-dimensional orthotropic material properties

Other modifications included:

(4) Capability for hygroscopic analysis

(5) Capability for elevated temperature and moisture content analysis

4.1.1 Increased Finite Element Capacity

In order to model an adhesive bonded joint a large number of finite elements are needed because of the large stress gradients and inherent large aspect ratio of the adhesive layer. For this reason the maximum number of elements was increased from 100 to 400 elements. This was done with an increase of high speed storage of approximately 50 percent.

This increase was held this low through the use of storage addressing schemes where many arrays are stored in the same common storage locations and by the block storage schemes of the equation solver chosen.

4.1.2 Solution of Simultaneous Equations

The equation solver in NONCOM is not suitable for large systems of equations as its solution time becomes excessively large for such systems. For this reason a new equation solver, SESOL [16] was selected for NONCOM1. This equation solver offers a fast solution time and high speed storage reduction schemes. In brief the solution algorithm considers the system of linear equations

$$[K]\{X\} = \{R\} \tag{4.1}$$

where [K] is the assembled stiffness matrix, {X} is the nodal displacement vector and {R} is the applied nodal load vector. The stiffness matrix is factored into an upper and lower triangular matrix

$$[K] = [L]^T[G] \tag{4.2}$$

where [G] is upper triangular and $[L]^T$ is lower triangular and normalized such that $L_{ii} = 1$ (i not summed). Since [K] is symmetric

$$G_{ij} = G_{ii}L_{ij} \quad \text{(i not summed)} \tag{4.3}$$

and equation (4.2) can be written as

$$[K] = [L]^T[D][L] \tag{4.4}$$

where

$$[D] = G_{ii} \quad (i \text{ not summed}) \tag{4.5}$$

Defining

$$\{v\} = [D][L]\{x\} \tag{4.6}$$

and combining equations (4.1) and (4.6) yields

$$[L]^T\{v\} = \{R\} \tag{4.7}$$

The vector {v} in equation (4.7) is first found by Gauss reduction of the load vector and then the nodal displacements are found through back substitution into equation (4.6). The stiffness matrix and load vector are assembled and stored on low speed storage in block form as in Fig. 4. During the solution process, reductions are performed on non-zero terms only and only two blocks need be in high speed storgage at any time.

In the computer program NONCOM1 the number of equations per block is determined as a function of the maximum half bandwidth plus the diagonal of the assembled stiffness matrix. This is done to minimize the number of blocks necessary and maximize the number of equations per block within high-speed storage limitations. By making the number of blocks a minimum, I-O operations performed by the computer with the elemental stiffness matrices are also minimized. To further this reduction of operations the blocks are assembled two at a time.

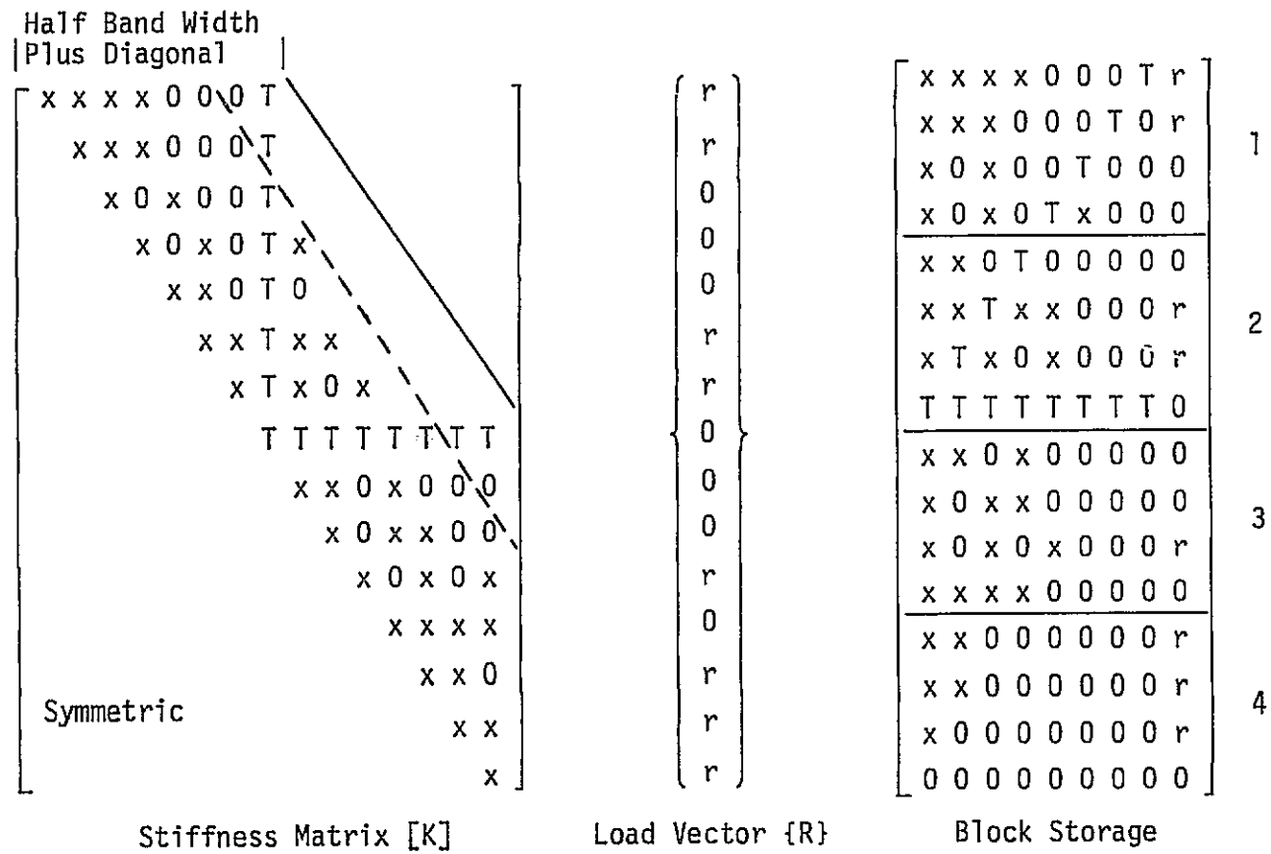

Figure 4

Block Storage of Stiffness Matrix and Load Vector

It should be noted the size of the maximum half bandwidth plus diagonal is not only a function of node numbering, as is usually the case with the finite element analysis, but is also a function of the type of loading applied. When the applied loading is thermal, hygroscopic or an average force applied in the x direction an equation relating a uniform strain to an average force in the x direction is required in addition to the equations relating nodal forces and displacements. This equation is related to all of the elements and may involve all the nodal displacements of the finite element model. To minimize the effect of this equation on the maximum half bandwidth plus diagonal it is assembled in the center of the stiffness matrix. The average force equation and its effect on the bandwidth can be seen in Fig. 4 where the T's represent the average force terms. The half bandwidth plus diagonal without the average force equation is shown by the dotted line. These two bandwidths are for identical finite element models under different loadings.

4.1.3 Three Dimensional Properties

The program NONCOM1 was given the capability for fully three dimensional orthotropic material properties because of the restriction that composite adherends must be modeled as homogeneous orthotropic laminates (Chapter 3). This means that a plane of transverse isotropy cannot in general be assumed as done in NONCOM [1].

4.1.4 Hygroscopic Analysis

A capability for hygroscopic loadings has been included in NONCOM1.

It is modeled in the computer program in exactly the same fashion as the thermal analysis and is therefore subject to the same limitations. The most notable of these is the restriction that the moisture distribution be uniform throughout the finite element model. Other restrictions will be mentioned in the section dealing with the nonlinear analysis.

4.1.5 Elevated Temperature and Moisture Content Analysis

This modification allows for mechanical loading at elevated temperature and moisture content or thermal loading at elevated moisture content or hygroscopic loading at elevated temperature. Insight into the interactions between thermal and hygroscopic material response could not be obtained from the literature. For this reason two assumptions are made about these interactions. First, it is assumed that hygroscopic properties are independent of temperature and that thermal properties are independent of moisture content. It is also assumed that changes in mechanical properties due to temperature and moisture content are cumulative. By cumulative it is meant that when a modulus is to be modified to correspond to both temperature and moisture content it is first modified for the temperature and then this new modulus is then modified to correspond to the moisture content. The process of changing material properties will be more fully described in the following section.

4.2 Nonlinear Analysis

In order to simulate nonlinear material behavior in a computer program with the linear elastic finite element analysis described in Chapter 3 two separate problems must be dealt with. First a method of

accounting for material nonlinearities within the analysis procedure and second a method of representing the nonlinear material properties.

4.2.1 Incremental Loading Procedure

The finite element computer program NONCOMI deals with varying material properties through the use of a incremental solution procedure. With this type of procedure, the load whether mechanical, thermal, or hygroscopic is applied as a series of increments. This yields a series of linear solutions with total stresses, strains, and displacements formed by summation of the linear increments of these quantities. When applying the load incrementally the material properties are updated to correspond to the current levels of strain, temperature, and mositure content. With the finite element method an individual element can have material properties varying independently of other elements in the model.

4.2.2 Nonlinear Data Input

Material stress-strain response for an othrotropic material in the principal material coordinates are represented in the form of modified Ramberg-Osgood [17] approximations which have the form

$$\varepsilon = \frac{\sigma}{E} + K_i \sigma^{n_i} \quad i = 1 \text{ or } 2 \tag{4.8}$$

In equation (4.8) E is the elastic modulus and K_i and n_i are Ramberg-Osgood coefficients. A method for calculating the four coefficients K_i and n_i is described in Ref. [1]. A tangent modulus can be defined as

$$\bar{E} = \frac{d\sigma}{d\varepsilon} = \frac{E}{K_i E n_i \sigma^{n_i - 1} + 1} \qquad i = 1 \text{ or } 2 \tag{4.9}$$

where $\bar{E}$ is the tangent modulus corresponding to the principal stress σ. Noting Fig. (5) the value of the stress σ^P corresponding to the strain at the end of load increment P is

$$\sigma^P = \sum_{k=1}^{P} \Delta\varepsilon^j \bar{E}^i \tag{4.10}$$

where $\Delta\varepsilon^j$ is the increment of strain during the jth load increment. Combining equations (4.9) and (4.10) yields for the $P + 1^{th}$ increment

$$\bar{E}^{P+1} = \frac{E}{K_i E n_i [\sum_{j=1}^{P} \Delta\varepsilon^j \bar{E}^j]^{n-1} + 1} \qquad i = 1 \text{ or } 2 \tag{4.11}$$

With equation (4.11) and principal material strains, the tangent moduli are calculated at the end of each increment to be used for the next increment. Moduli determined are $\bar{E}_{11}$, $\bar{E}_{22}$, $\bar{E}_{33}$, $\bar{G}_{23}$, $\bar{G}_{13}$, and $\bar{G}_{12}$. It can be seen in Fig. 5 that the strain ε^P_{R-0} for which the tangent modulus is calculated differs from the strain ε^P where the modulus should be calculated. This difference is a function of the size of the load increment and can be made negligible by choosing an appropriately small increment. For the computer analysis it is assumed that the shear response is independent of sign while extensional behavior can be different in tension and compression.

Temperature and moisture dependent properties are represented as linearly segmented curves. These properties consist of percent modulus retention curves which represent the change in stiffness of a material

due to variations in temperature or moisture levels and coefficients of thermal and hygroscopic expansion as functions of temperature and moisture content respectively. During thermal or hygroscopic loading, the moduli and coefficients of expansion are calculated at the mid-point of the increment using linear interpolation. For input to the computer program it is assumed that percent modulus retentions are identical for tension and compression.

Chapter 5

RESULTS AND DISCUSSIONS

The analysis procedures presented in Chapters 3 and 4 were used to generate laminate properties and analyze various bonded joints. The joints investigated included single and double lap joints with, and without adhesive layers. Both elastic and non-linear results are presented. The material systems considered were graphite-polyimide, boron-epoxy, titanium, and aluminum for the adherends, and Metlbond 1113 and AF-126-2 for the adhesives.

5.1 Materials Properties

The mechanical and thermal properties for the materials used in this study were taken from the literature whenever possible. However, as was stated in previous chapters, complete properties were not always available for a given material system. Therefore, laminate properties, with the exclusion of uni-directional laminates, were predicted in accordance with the analysis procedures presented earlier and the results can be found in Appendix C which contains all of the material properties of this study.

5.2 Averaging of Finite Element Results

The finite element analysis presented in Chapter 3 is based upon a displacement formulation. This approach yields results in the form of displacements at the node points and stresses and strains which are constant over each element. Because the stresses are constant for an

individual element, a distribution of stresses over a series of elements may appear to be discontinuous. In many cases, however, it is known that the stresses must be continuous. For this reason, stress averaging was used to produce the desired smooth distributions.

Noting Fig. 6a, stresses are presented along the line A-A which corresponds to the mid-plane of the adhesive layer. The stresses presented at point E would correspond to an average of the stresses in elements 3 and 4. This method of averaging was used for all joints with adhesive layers.

When considering bonded joints without adhesive layers, the stresses in question are along the interface between the two adherends. This interface is shown as line C-C in Fig. 6b. For the stresses τ_{yz} and σ_z which must be continuous across the interface, the results presented correspond to an average of elemental stresses above and below the interface. Thus, these stresses at point G would consist of an average of elements 13, 14, 21, and 22. The normal stress components σ_x and σ_y are not necessarily continuous across this interface so these stress components are averaged along both line B-B, and line D-D. At point F, an average of element 11 and 12 is presented and at point H, the stresses are averaged between element 19 and 20.

The stress components τ_{xy} and τ_{xz} have not been mentioned as they do not occur either at the mid-plane of the adhesive layer in adhesive bonded joints, nor at the interface between the adherends in non-adhesive bonded joints since the adherends in this study, when composite laminates, are considered to be homogeneous, orthotropic materials. If

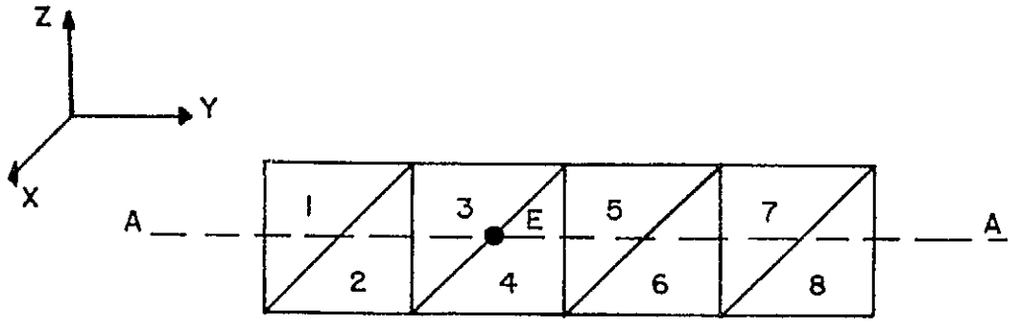

(a) JOINT WITH ADHESIVE

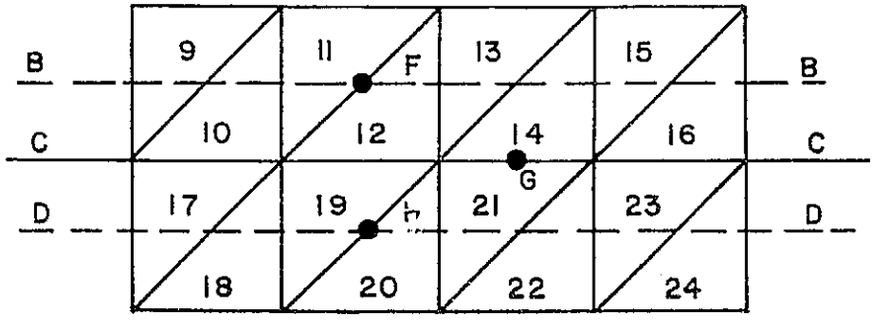

(b) JOINT WITHOUT ADHESIVE

Figure 6. Averaging of Finite Element Results

these components were present it could easily be shown that τ_{xz} must be continuous across an adherend-adherend interface while τ_{xy} would need not be.

5.3 Finite Element Representations

For the analysis of bonded joints, two finite element models were used. Fig's. 7 and 8 show partial plots of the finite element models of joints with, and without adhesive layers, respectively. Both of these models were generated using a mesh generator described by Bergner, Davis, and Herakovich [18]. In both figures the scaling of the model for the figure is not uniform. In Fig. 7, the aspect ratio of an element in the adhesive layer ranges from 2.5 at the free edge to 15 at the center of the adhesive layer. The aspect ratio's of the elements in the adherends range from 1.1 to 9.0. For the joints without adhesives (Fig. 8) all aspect ratios are 1.0.

5.4 Stress Free Temperature

Bonded joints are, in general, cured with a combination of elevated temperature and pressure. The maximum temperature involved in this process is known as the cure temperature. The temperature at which curing stresses begin to form is the stress free temperature and, in general, the cure and stress free temperatures are not the same. The stress free temperature of the adhesives used in this study was chosen to be 270°F. This value was selected because both adhesives are epoxy based and 270°F was the value used in [1] for epoxy matrix material systems.

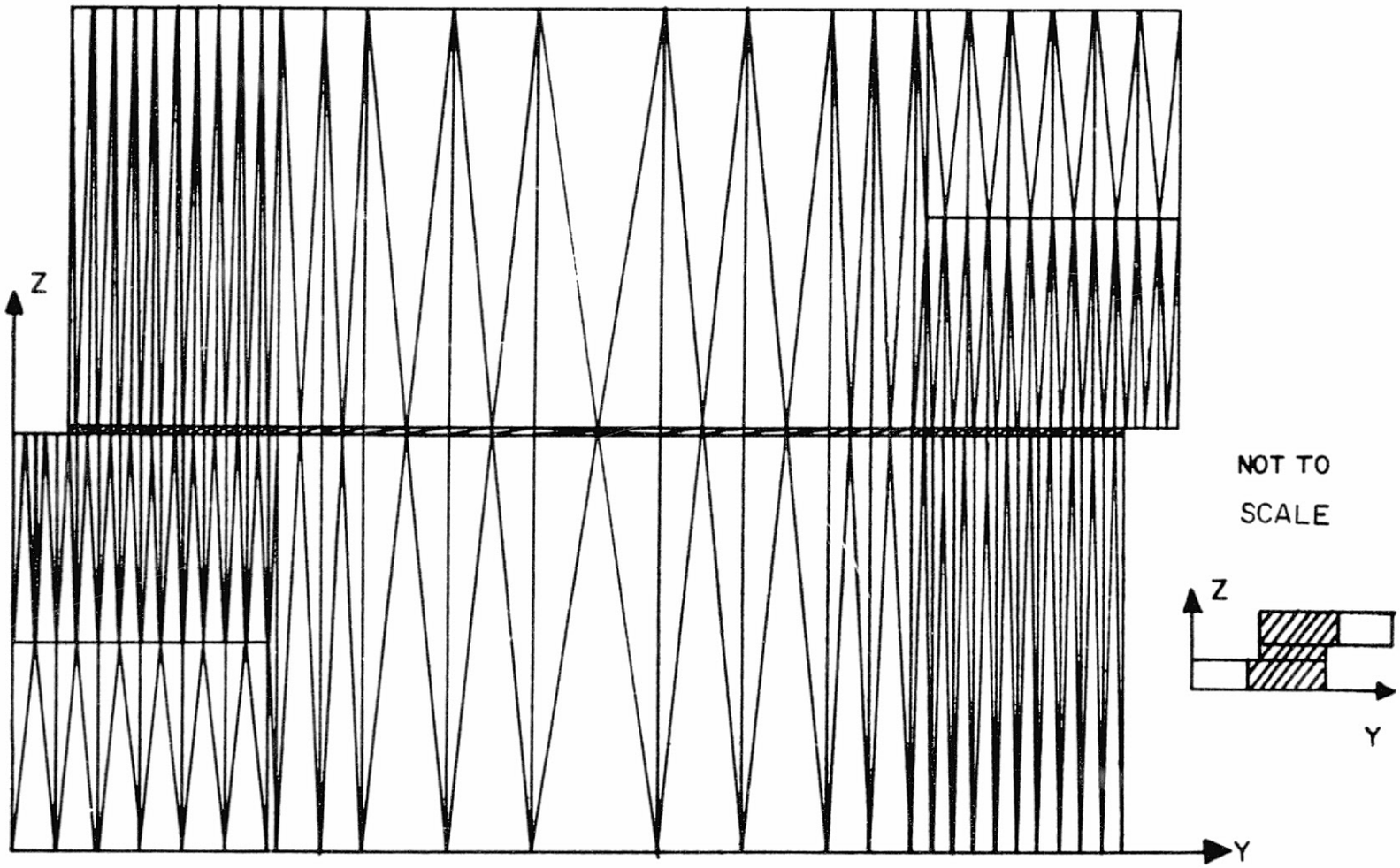

Figure 7. Partial Finite Element Grid for Joint with Adhesive Layer

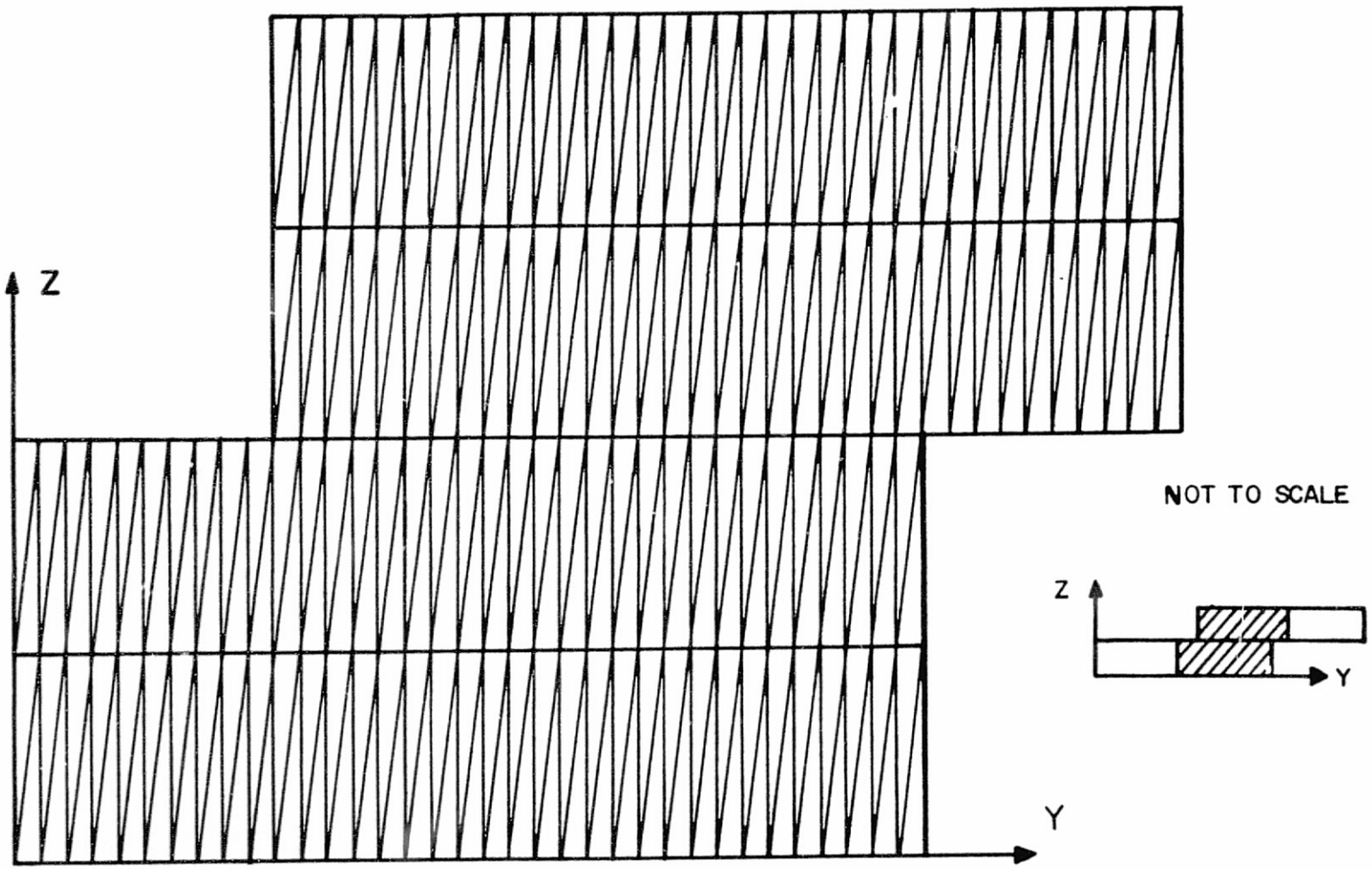

Figure 8. Partial Finite Element Grid for Joint without Adhesive Layer

For bonded joints without adhesives, the stress free temperature was chosen to be 350°F. This is the value reported in [19] as the stress free temperature of graphite-polyimide laminates. This is appropriate as polyimides were the only composite lamiantes used in joints without adhesives.

5.5 Linear Elastic Results

This section contains the linear thermoelastic results for various joints. The dimensions for adhesive bonded joints are shown in Fig. 1. For joints without adhesives the dimensions are identical to those of joints with adhesives except the adhesive layer is removed. Most of the curves in this section were drawn by the VPI & SU computer plotter.

In the figures that follow the superscripts M and T are used to differentiate stresses. Mechanically induced stresses are indicated by the superscript M while thermal, or curing, stresses are denoted by the superscript T. These are also used in combination indicating a superposition of mechanical and curing stresses. In some instances a curing stress is referred to, while the corresponding figure presents only the mechanical, and combined mechanical and curing stresses. The magnitude of the curing component can, of course, be determined by taking the difference of the combined, and mechanical stresses.

5.5.1 Single Lap Joints with Adhesives

5.5.1.1 [0] Graphite-Polyimide Adherends

The adhesive stresses of a single lap joint with [0] graphite-polyimide adherends and Metlbond 1113 adhesive are shown in Fig. 9. The

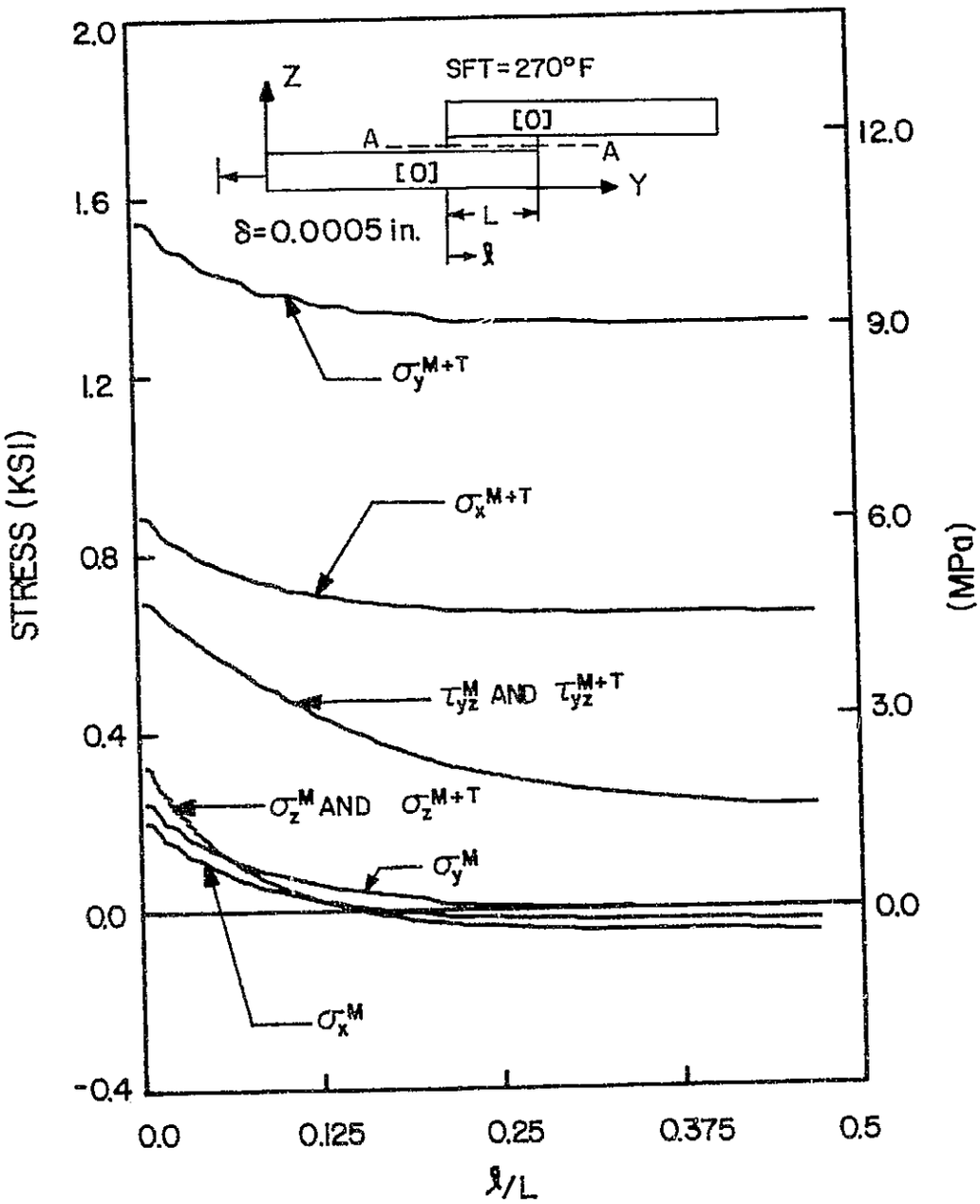

Figure 9. Elastic Mechanical and Curing Adhesive Stresses of a Single Lap Joint with [0] Gr/Pi Adherends and Metlbond 1113 Adhesive

loading consists of a thermal increment of -200°F and an applied displacement. The resulting stresses are shown to $\ell/L = 0.5$ as the stresses are symmetric about this line.

Upon examination of Fig. 9 it is seen that the stress free boundary conditions

$$\sigma_y\Big|_{\ell/L\,=\,0} = 0 \text{ and } \tau_{yz}\Big|_{\ell/L\,=\,0} = 0 \qquad (5.1)$$

are not satisfied by the finite element solution. This is due to the nature of the constant stress finite elements used and the limitations on the maximum number of element available. In order to check the finite element analysis' ability to meet such stress free boundary conditions, an analysis was performed on a small portion of the adhesive layer from $\ell/L = 0.0$ to $\ell/L = 0.05$. The displacements predicted along the upper and lower interfaces of the adhesive in the joint solution were used as loading for the partial adhesive analysis. The stress distributions produced by this analysis exhibited the proper trends with σ_z reaching a peak value near $\ell/L = 0$ and σ_y and τ_{yz} tending towards zero. These distributions are not presented, however, as they appeared very erratic. It is believed that this was caused by round-off error in the applied displacements. This error may have become significant after subtracting rigid body motion from the joint analysis displacements.

In order to check the validity of the finite element solution presented in Fig. 9, a number of static equilibrium calculations were

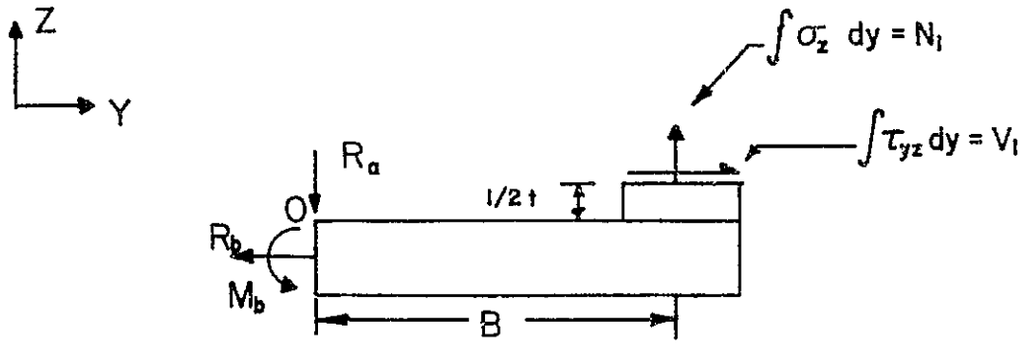

(a)

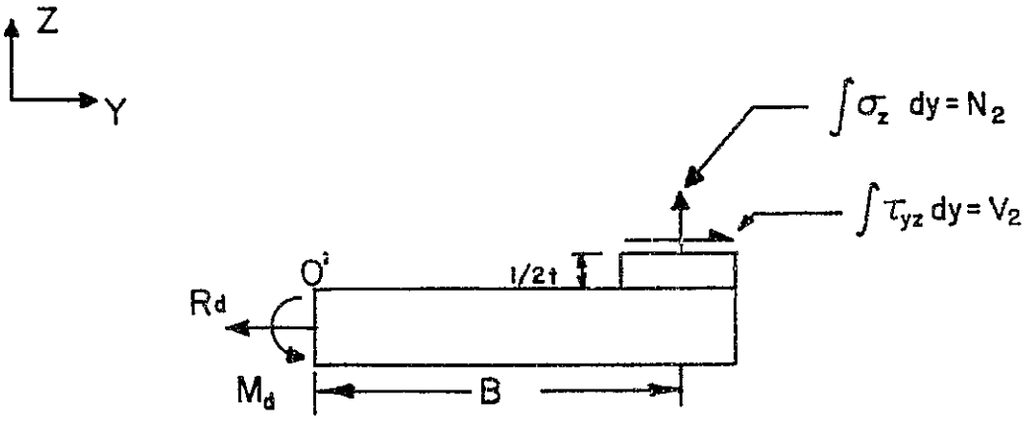

(b)

Figure 10. Free Body Diagrams of Single Lap Joints Under Two Sets of Boundary Conditions

made. The equilibrium equations for one half of a single lap joint corresponding to the free body diagram of Fig. 10a are

$$\Sigma F_y = 0 = V_1 - R_b,$$

$$\Sigma F_z = 0 = N_1 - R_a,$$

and (5.2)

$$\Sigma M_0 = 0 = M_b + \frac{1}{2} tV_1 - BN_1$$

The finite element program NONCOM1 does not back substitute the nodal displacements to solve for the nodal forces. Therefore it is not possible to determine the reactions R_a or M_b. However, the reaction R_b can be determined as the average of the σ_y stresses of the elements adjacent to the edge where R_b acts multiplied by the adherend thickness and assuming a unit depth. A comparison of V_1 and R_b determined from the finite element solution indicates a four percent error as shown in Table 2.

Since the unknown reactions severely limit the equilibrium calculations for the previous joint, similar calculations were also performed on a more simply constrained joint. This joint corresponds to the joint shown in Table 1, condition 4, and a free body diagram of one half of the joint is shown in Fig. 10b. For this free body diagram the equilibrium equations are

$$\Sigma F_y = 0 = V_2 - R_d,$$

$$\Sigma F_z = 0 = N_2, \tag{5.3}$$

TABLE 2

Results of Equilibrium Checks of Single Lap Joint with [0] Gr/Pi Adherends and Metlbond 1113 Adhesive Under Two Sets of Boundary Conditions

Joint F.B.D. (Fig. 10)	ΣF_y	ΣF_z
a	v_1 = 92.6 lb R_b = 89.0 lb ERROR = 4.0%	
b	v_2 = 71.8 lb R_d = 78.3 lb ERROR = 8.3%	N_2^{FE} = -0.25 lb N_2^{EXACT} = 0.0 lb

and

$$\Sigma M_{0'} = 0 = M_d - \frac{1}{2} tV_2$$

As in the previous joint, the reaction moment M_d cannot be determined from the finite element solution. However, by removing the constraint in the z direction, the integral of the σ_z stresses, N_2, must now equal zero. The results of these equilibrium calculations are also shown in Table 2.

Returning to Fig. 9, it can be seen that under mechanical loading only, the shearing stresses dominate the stress fields. This is a function of the overlap lenth, L. If the overlap were longer, for a given loading, the shearing stresses would be reduced while the peak σ_z^M stresses would increase. This will be shown later in the section containing nonlinear results and can be verified by considering the force and moment equilibrium equations (5.2). It is interesting to note that the normal stresses σ_x^M, σ_y^M, and σ_z^M are very close in magnitude for this joint.

Since the stresses presented are produced by the displacements of the joint, its deflected shape would provide significant insight into the physics of the problem. Fig. 11 shows the deflection of the upper edge of the lower adherend under mechanical loading only. The dashed line signifies the beginning of the overlap ($\ell = 0$). In this figure it is difficult to distinguish any curvature of the adherend in the region of the overlap because of the relatively small distance involved. A plot of the overlap only showed a nearly straight line distribution also indicating very little bending in this region. It is interesting

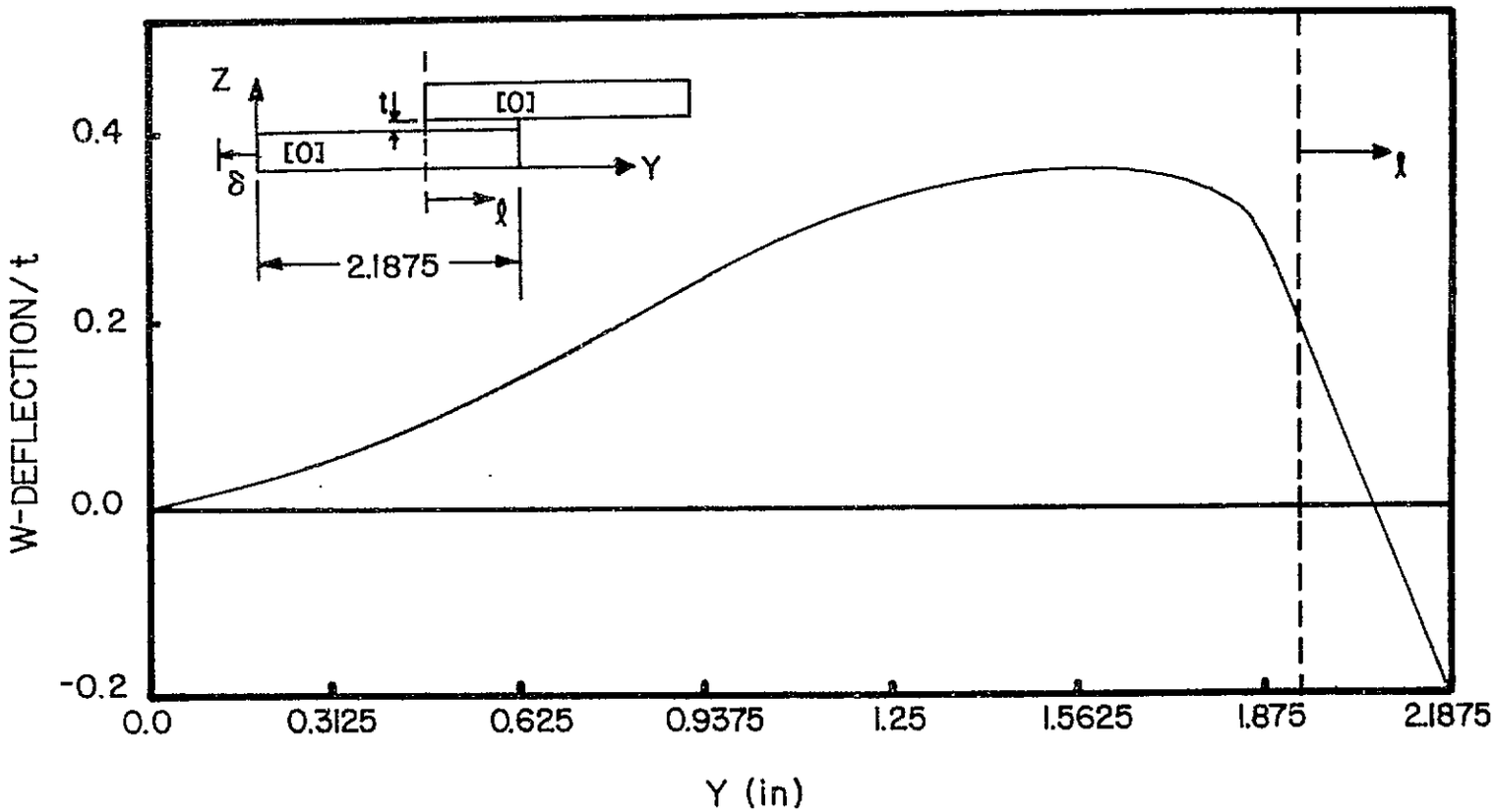

Figure 11. Deflected Shape of the Lower Adherend of a Single Lap Join Under Mechanical Loading

that the maximum bending occurs just before the overlap region. However, due to the layout of the finite element model, which was designed for adhesive studies, the stresses in this high bending region cannot be accurately obtained.

Again returning to Fig. 9 it is seen that the only nonzero components of curing stresses are σ_x^T and σ_y^T. Actually, the finite element solution did predict other components of curing stresses but their magnitudes were insignificant. It is difficult to make a valid comparison of the relative magnitudes of the mechanical and curing stress components as the mechanical loads were produced by a small load increment while the curing stresses are due to the full temperature change from the stress free temperature to room temperature. The σ_y^T curing stresses represent approximately 15 percent of the ultimate strength of the adhesive and while this magnitude is not exceedingly large, its contribution should be included in a failure theroy.

5.5.1.2 $[0/\pm45/90]_s$ Graphite-Polyimide Adherends

Fig. 12 represents the mechanical and curing stresses for a single lap joint with $[0/\pm45/90]_s$ graphite-polyimide adherends and Metlbond 1113 adhesive. The loadings are identical with those of the previous joint. Comparing Fig's. 9 and 12 it can be seen that under mechanical loading only, the magnitude of the peak adhesive stresses decrease with decreasing adherend stiffness E_y. Thus, for the same loading, the joint with [0] adherends has higher stresses than the joint with $[0/\pm45/90]_s$ adherends. However, when considering curing stresses, this is no longer the case. It can be seen that the magnitudes of the stresses σ_x^T and

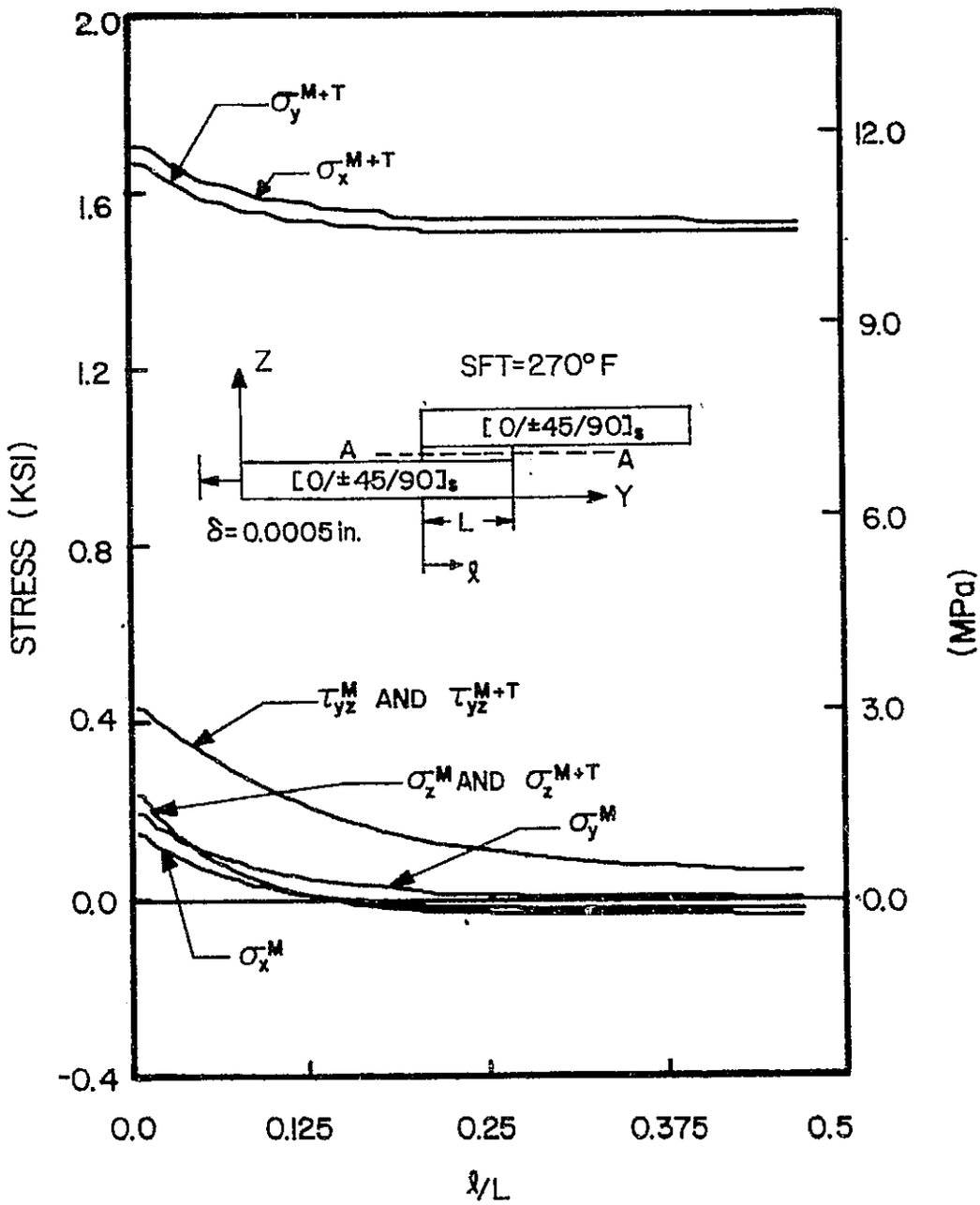

Figure 12. Elastic Mechanical and Curing Adhesive Stresses of a Single Lap Joint with $[0/\pm45/90]_s$ Gr/Pi Adherends and Metlbond 1113 Adhesive

σ_y^T are larger for the $[0/\pm45/90]_s$ joint than for the [0] joint. This is due to the effects of the transverse stiffness and coefficient of the thermal expansion. For the $[0/\pm45/90]_s$ adherends the longitudinal (y) and transverse (x) directions have identical modulus and coefficient of expansion. This quasi-isotropy leads to curing stresses, σ_x^T and σ_y^T, that are identical for the joint with $[0/\pm45/90]_s$ adherends. This is not the case for the joint with [0] adherends as the transverse direction has a much lower modulus and higher coefficient of expansion than the longitudinal direction.

Because the adherends of this joint have identical transverse and longitudinal stiffness it is appropriate to determine what effects the transverse stiffness have upon the mechanically induced stresses. For this purpose the joint of Fig. 12 was also loaded under a classical plane strain assumption. The resulting stresses are shown in Fig. 13. The loading and materials were identical for both joints except that for the joint of Fig. 13 the average normal stress acting perpendicular to the plane was not specified and the strain normal to the plane, ε_x, was zero. Also, σ_x stresses are not presented for the classic plane strain solution. Comparing the two figures (12 and 13) it can be seen that the mechanically induced stresses are reduced slightly for the quasi three-dimensional analysis. This indicates that a 2-D solution would underestimate the strength of this joint. Comparisons of the stress components for the two joints can be found in Table 3. The curing stresses are identical for the two joints because both analyses were performed under the 3-D analysis.

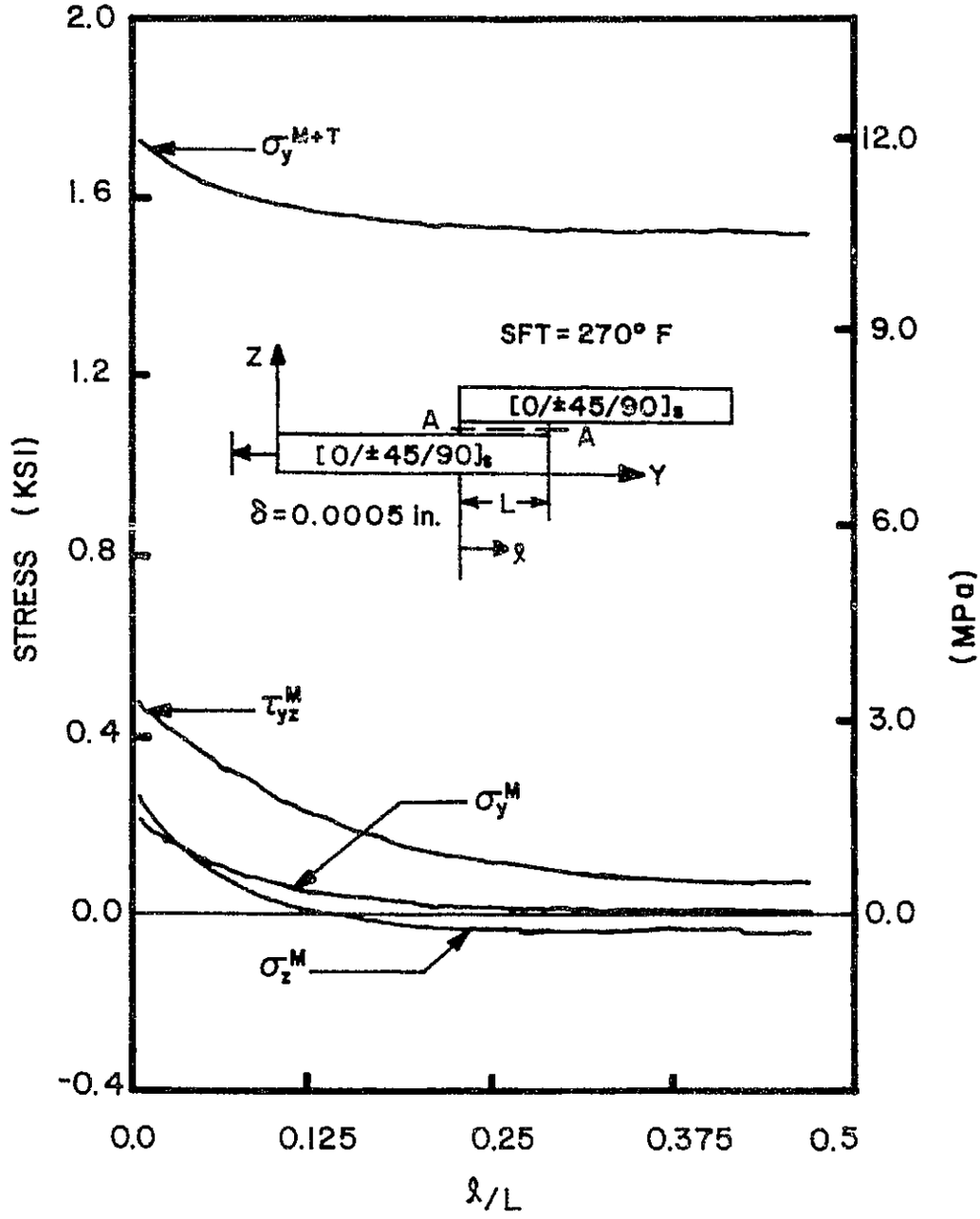

Figure 13. Elastic Mechanical and Curing Adhesive Stresses of a Single Lap Joint with $[0/\pm45/90]_s$ Gr/Pi Adherends and Metlbond 1113 Adhesive, $\varepsilon_x=0$

TABLE 3

Comparison of Peak Adhesive Stresses of $[0/\pm45/90]_s$
Joint Under Mechanical Loading for
2-Dimensional and Quasi 3-Dimensional Analysis

Type of Analysis	Peak τ_{yz}^{M} (ksi)	Peak σ_z^{M} (ksi)	Peak σ_y^{M} (ksi)
2-D	1.44	.826	.654
3-D	1.33	.762	.60
Percent Difference	8%	8%	8%

5.5.1.3 [90] Graphite-polyimide Adherends

The mechanical and curing stresses of a single lap joint with [90] graphite-polyimide adherends and Metlbond 1113 adhesive are shown in Fig. 14. Comparing Figs. 9, 12, and 14 the trends pointed to earlier concerning adhesive stresses and adherend stiffness are again confirmed. It is seen that the [90] adherends produce the lowest mechanical stresses of the three joints. Comparing Fig's. 9 and 14 only it is revealed that the σ_x^T curing stresses for the [0] joint are identical to the σ_y^T stresses for the [90] joint. This is as would be expected and the same correspondence is also seen between the σ_x^T of the [90] joint and the σ_y^T of the [0] joint.

5.5.1.4 [0] and [90] Graphite-Polyimide Adherends

The adhesive stresses for a single lap joint with [0] and [90] graphite-polyimide adherends and Metlbond 1113 adhesive due to mechanical loading only are presented in Fig. 15. The most striking aspect of these stresses is the lack of symmetry present in their distributions. This is due, of course, to the unsymmetric nature of this joint. It is also interesting to note that the peak values of stress occur near the line $\ell/L = 1.0$ This correspondence of the peak stresses with the more flexible adherend seems inconsistent as the trends of the previous joints pointed to higher stresses with stiffer adherends. This can be explained upon examination of Fig. 16 which presents displacements of the upper adherend-adhesive interface relative to the displacements of the lower adherend-adhesive interface. The displacements are normalized with respect to the thickness of the adhesive layer. It can be seen

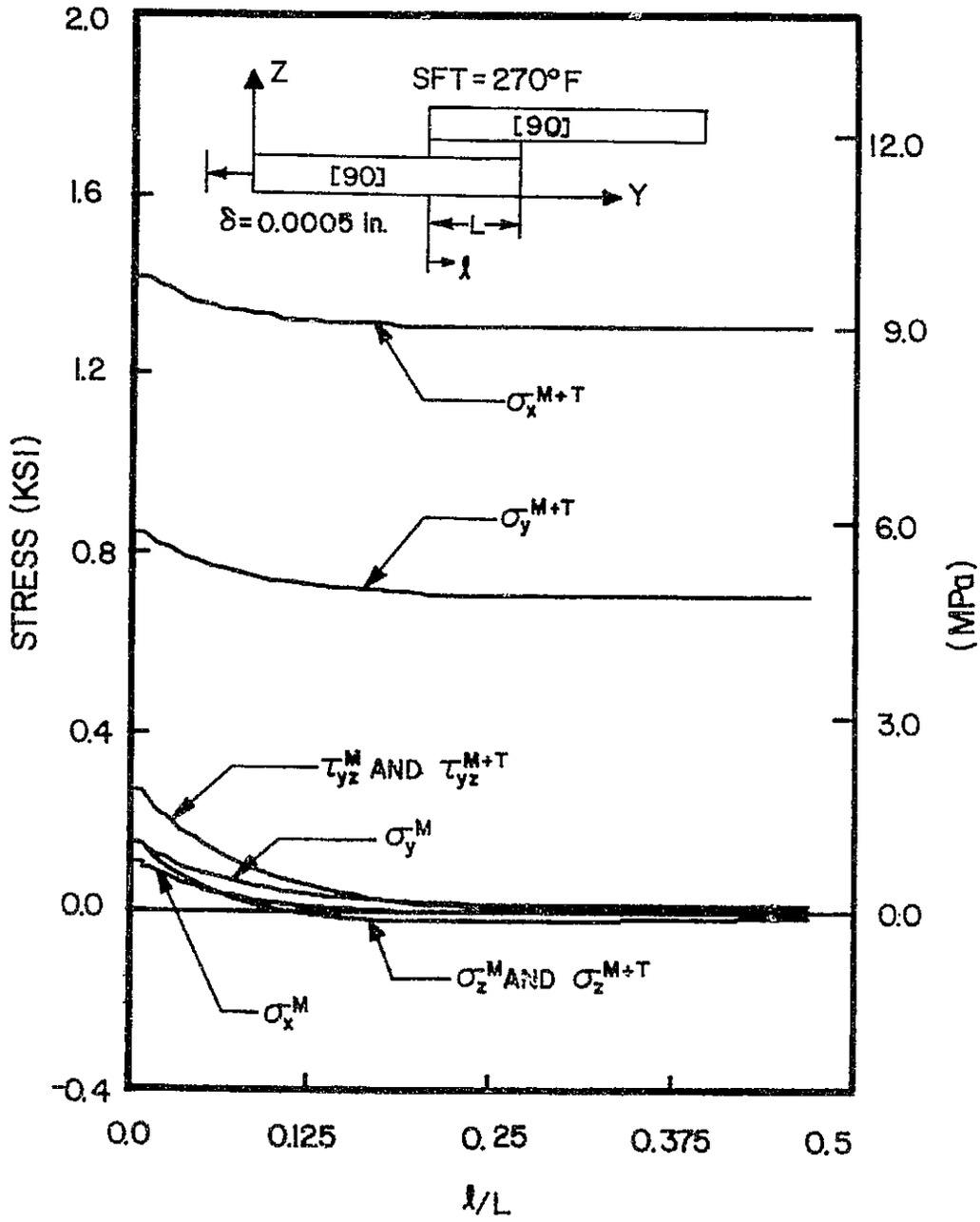

Figure 14. Elastic Mechanical and Curing Adhesive Stresses of a Single Lap Joint with [90] Gr/Pi Adherends and Metlbond 1113 Adhesive

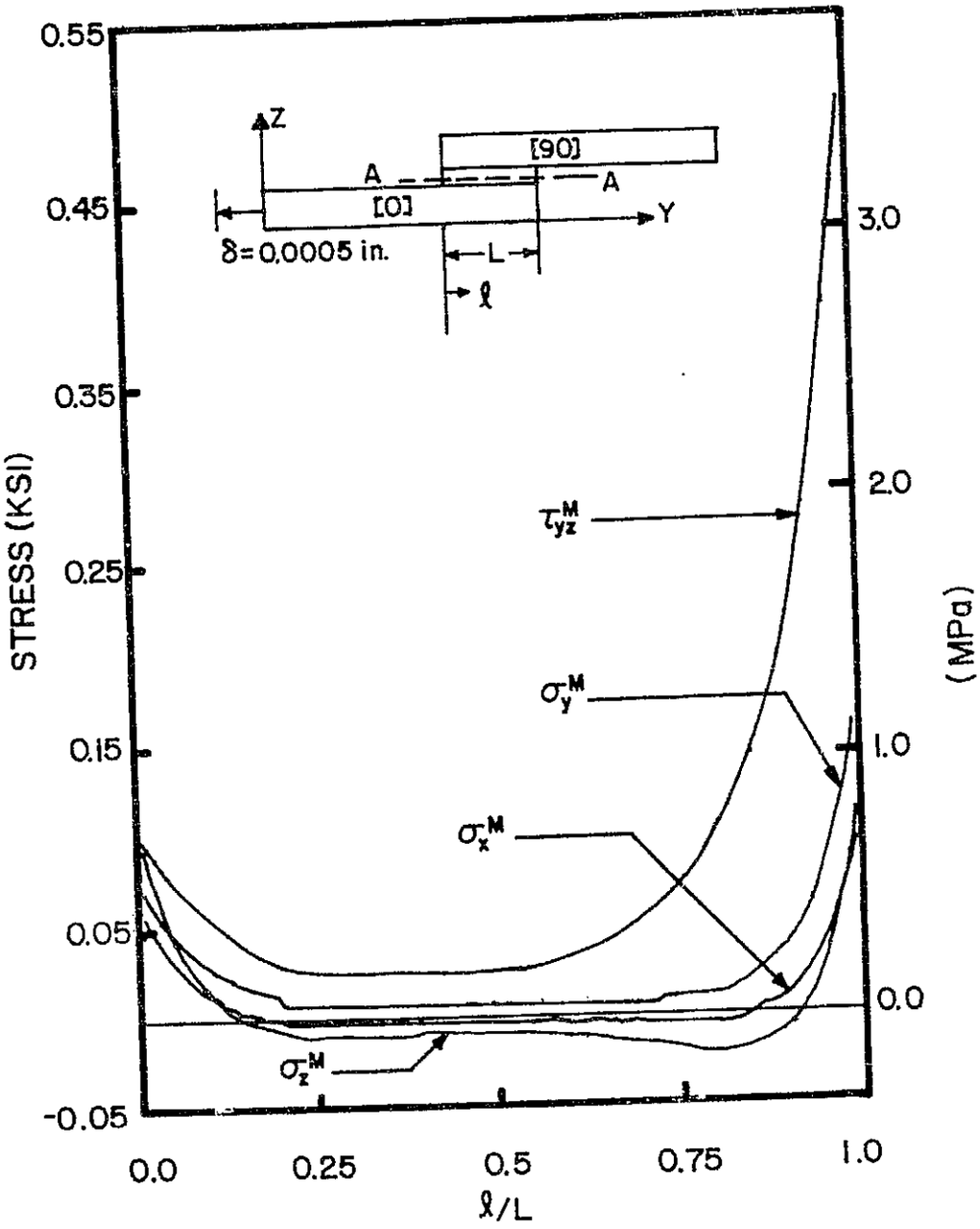

Figure 15. Elastic Mechanical Adhesive Stresses of a Single Lap Joint with [0] and [90] Gr/Pi Adherends and Metlbond 1113 Adhesive

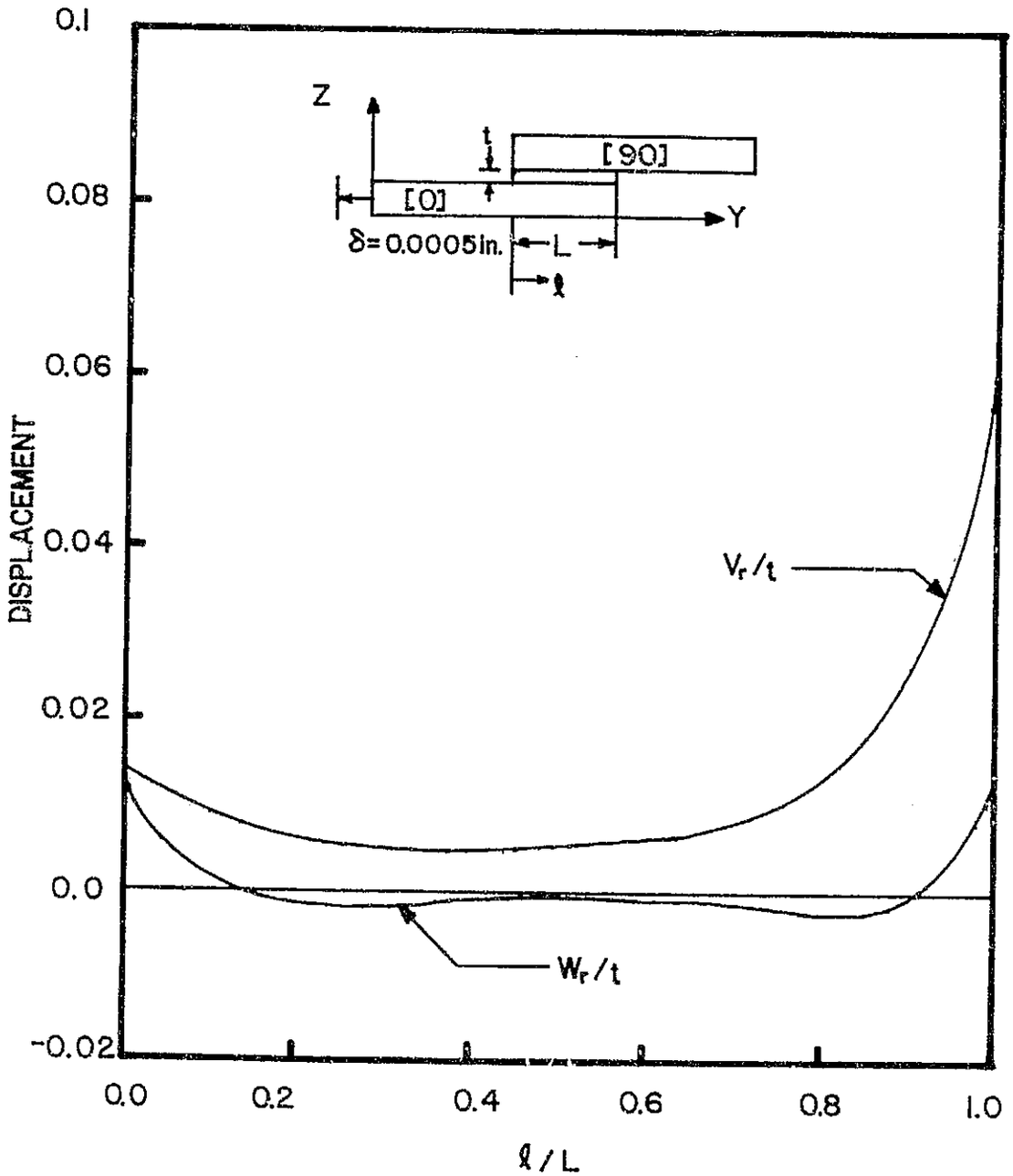

Figure 16. Relative Displacements of a Single Lap Joint with [0] and [90] Gr/Pi Adherends and Metlbond 1113 Adhesive Normalized with Respect to the Adhesive Thickness

that the relative displacements v_r (y-component) reach a much higher value at $\ell/L = 1$ than at $\ell/L = 0$, while the w_r displacements (z-component) are nearly symmetric about the center of the joint ($\ell/L = 0.5$). The normalized component v_r can be considered as a shear strain thus indicating why the shearing stresses are much larger near $\ell/L = 1$ in Fig. 15. It is interesting that the w_r component is nearly symmetric. This indicates that bending is not a major factor. This corresponds to the results seen in Fig. 11 where the curvature of adherend was nearly zero in the overlap region. From Fig. 16 it is seen that the increased stresses are due, almost entirely, to the increased flexibility (E_y) of the [90] adherend.

Returning to Fig. 15 a discontinuity in the σ_y^M stress distribution can be observed at $\ell/L = 0.2$. This can be explained as a change in adherend stiffness corresponding to a change in the finite element representation of the adherend. Referring back to Fig. 7, this change in representation is seen as the point at which the adherend in the model is changed from two, to one layer of elements. This situation was unavoidable due to the large number of elements required to model the adhesive layer and a limitation on the maximum number of elements available. This change in stiffness is recognizable in many of the stress distributions presented for adhesive bonded joints.

Curing stresses for the single lap joint with [0] and [90] adherends are presented in Fig. 17. These stresses are, not surprisingly, different than those for the joints presented earlier. For this case, all of the components of stress induced by mechanical loading are

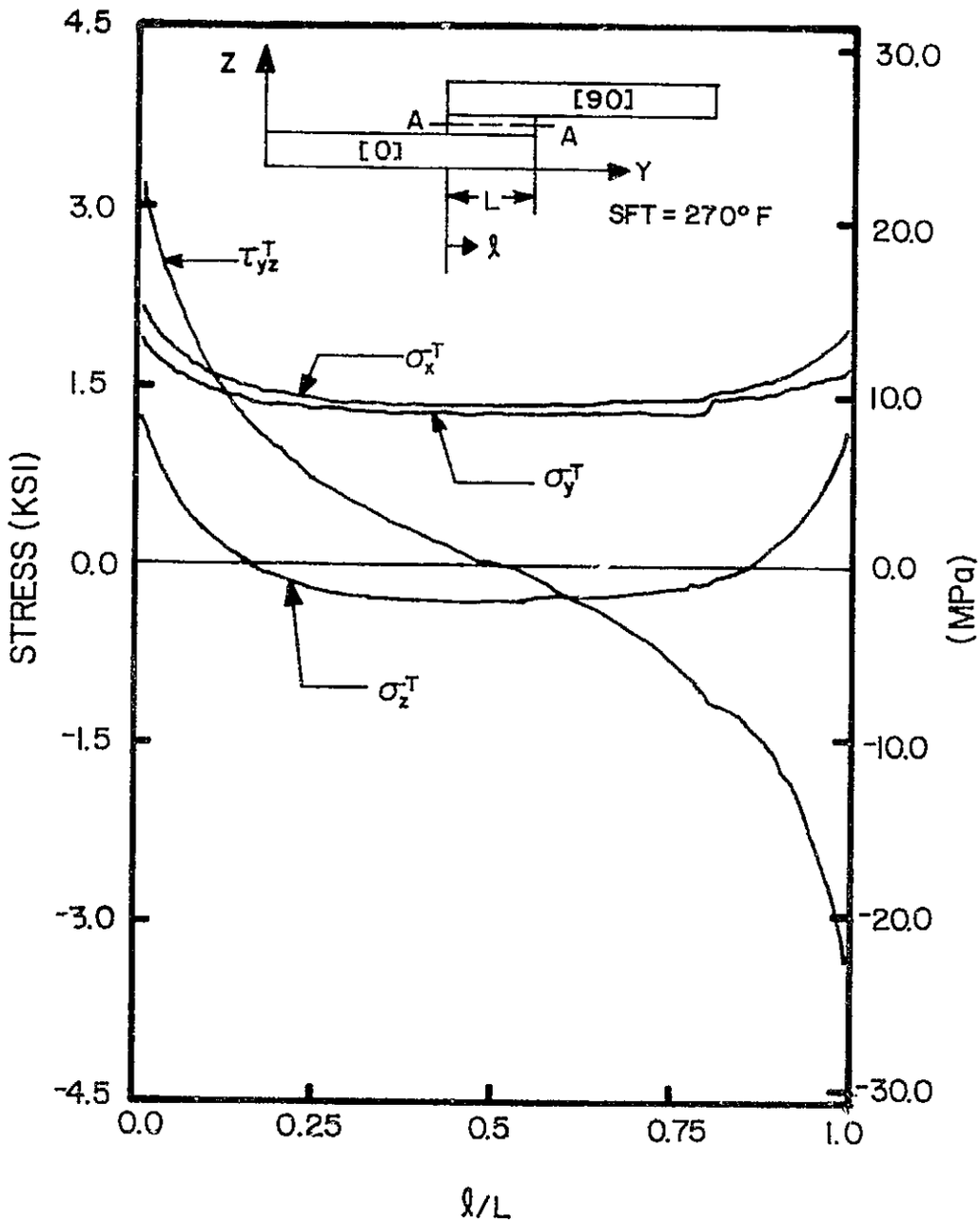

Figure 17. Elastic Curing Adhesive Stresses of a Single Lap Joint with [0] and [90] Gr/Pi Adherends and Metlbond 1113 Adhesive

present due to cure. From observing the τ_{yz}^{T} and σ_{z}^{T} distributions it can be seen that the integrals of these stresses appear to be zero, as would be required by equilibrium considerations. It is interesting to note the magnitude of the τ_{yz}^{T} stress peaks near $\ell/L = 0$ and $\ell/L = 1$. The values of shearing cure stresses are nearly 75 percent of the ultimate shear strength of the adhesive. Because the mechanical and curing stresses have opposite signs near $\ell/L = 1$ it can be seen that curing counteracts the large mechanical stresses in this region. It should be mentioned, however, that the percent modulus retentions, used for determining moduli as functions of temperature, are only strictly valid through a limited portion of the stress-strain curve of a material. Because of this, the peak shear cure stresses may not be quite as accurate as the other components of cure stress which correspond to points lower on their respective stress-strain curves.

5.5.2 Double Lap Joints with Adhesives

5.5.2.1 [0] Graphite-Polyimide Adherends

The adhesive stresses due to curing and mechanical loading for a double lap joint with [0] graphite-polyimide adherends and Metlbond 1113 adhesive are presented in Fig. 18. Here, as with the single lap joints, the mechanically induced shearing stresses dominate the mechanical stresses. It is interesting to note the lack of symmetry present in these stress distributions due to the restrictions upon the w displacements along the midsurface of the inner adherend. These restrictions are induced by the symmetry of joint about the midsurface of the inner

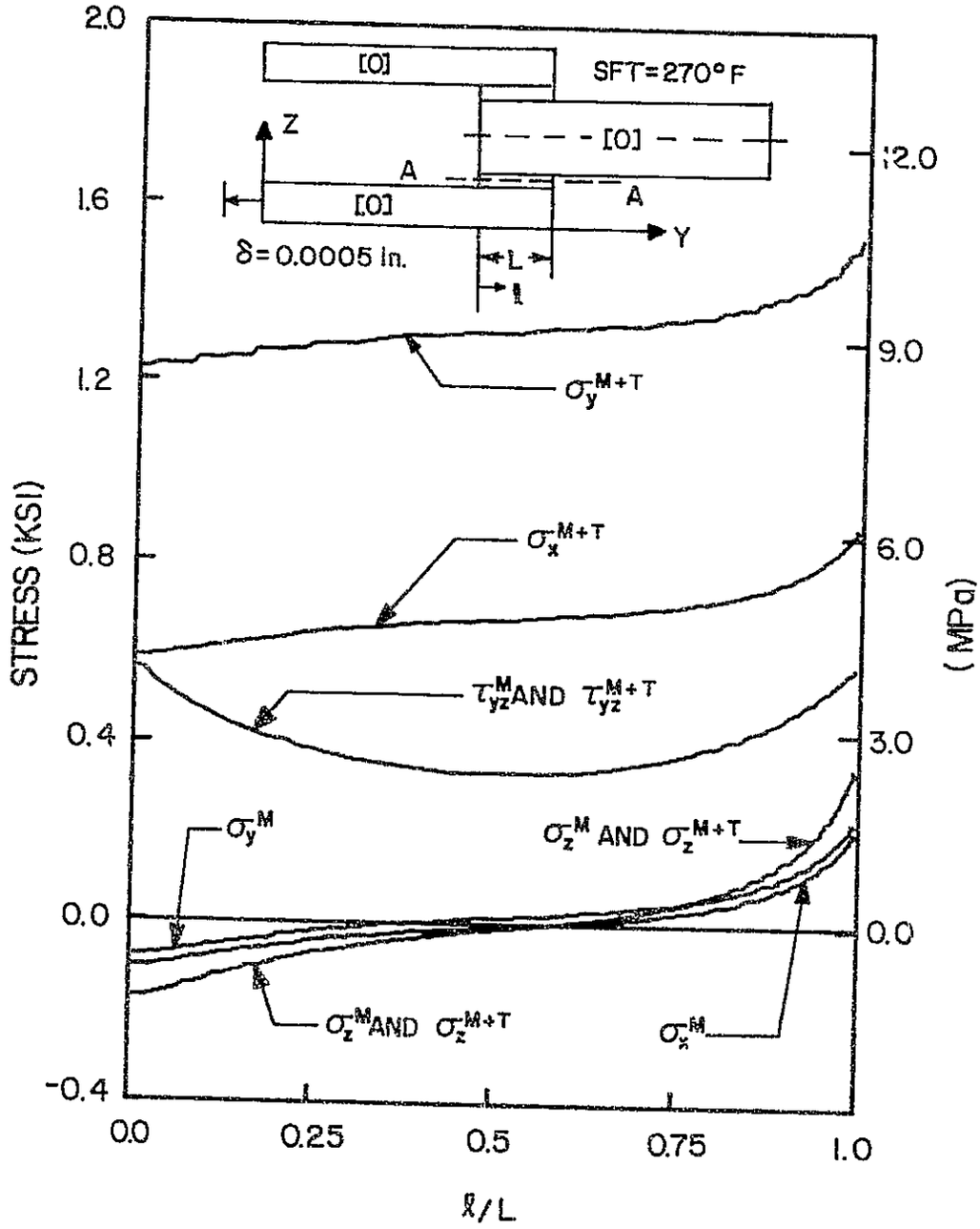

Figure 18. Elastic Mechanical and Curing Adhesive Stresses of a Double Lap Joint with [0] Gr/Pi Adherends and Metlbond 1113 Adhesive

adherend. Comparing Fig's. 9 and 18 it can be seen that the mechanically induced stresses are smaller for the double lap joint than for the single lap joint. The distributions are more uniform for the double lap joint indicating reduced bending in the adherends. This is also due to the restrictions on the w displacements.

The curing stresses for this double lap joint follow the trends exhibited by the single lap joints where the adherends were identical, with σ_x^T and σ_y^T being the only significant curing stresses. As expected, the magnitudes of the curing stress components are identical to those of the single lap joint with [0] adherends.

5.5.2.2 [90] Graphite-Polyimide Adherends

Fig. 19 represents the curing and mechanical loading induced stresses of a double lap joint with [90] adherends. Comparing Fig's. 18 and 19 it is seen that the peak stress values decrease with increased flexibility of the adherends, as was the case with single lap joints. Noting the curing stresses of both of these joints it can be seen that the σ_x^T cure stresses are higher for the [90] adherend joint while the σ_y^T cure stresses are higher for the [0] adherend joint. This is exactly the same as with the single lap joints and the reason for it is also the same.

5.5.2.3 [0] and [90] Graphite-Polyimide Adherends

Mechanically induced adhesive stresses of a double lap joint with [0] and [90] graphite-polyimide adherends and Metlbond 1113 adhesive are represented in Fig. 20. As was the case with the two previous double lap joints, comparisons made with a single lap of the same adherends

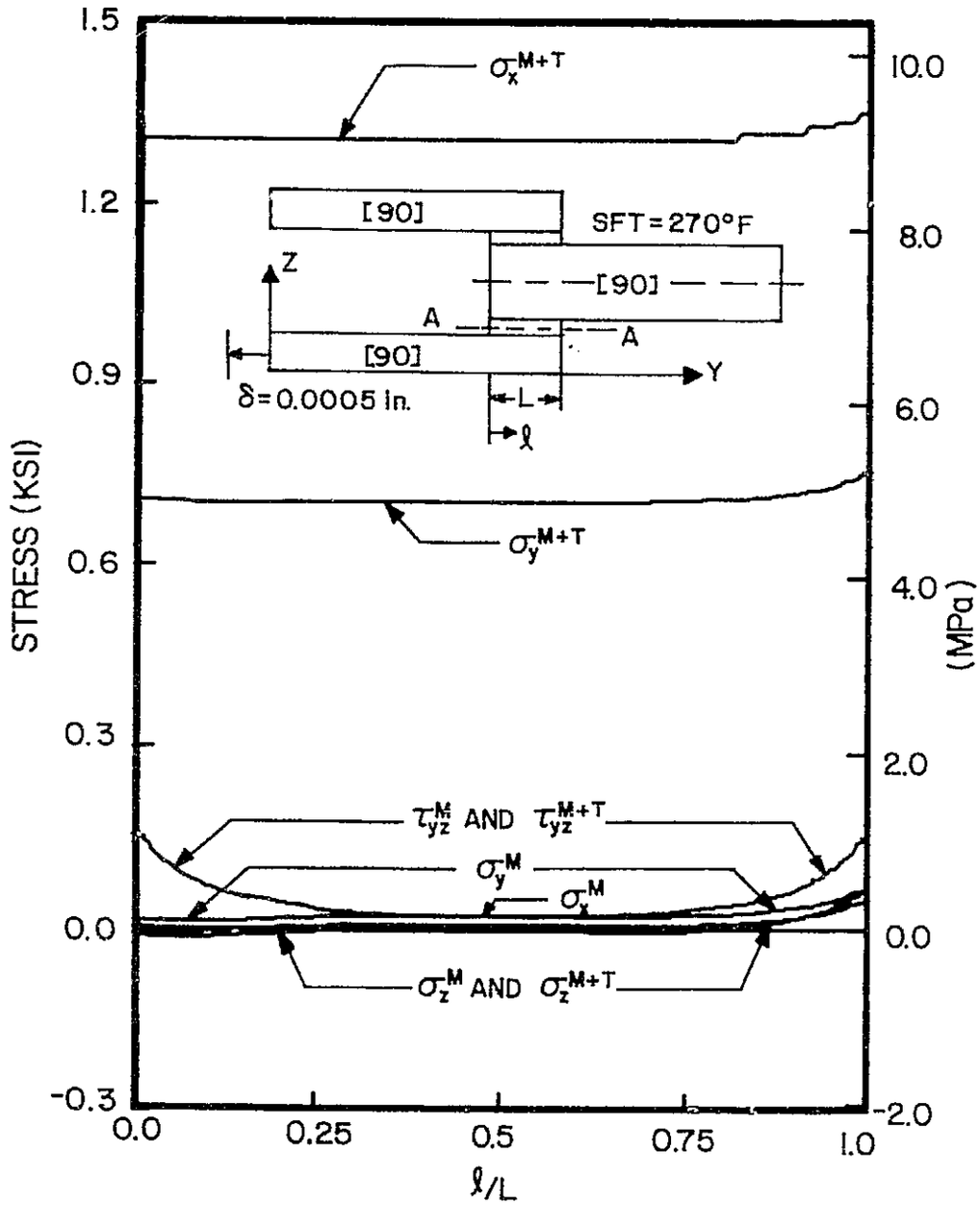

Figure 19. Elastic Mechanical and Curing Adhesive Stresses of a Double Lap Joint with [90] Gr/Pi Adherends and Metlbond 1113 Adhesive

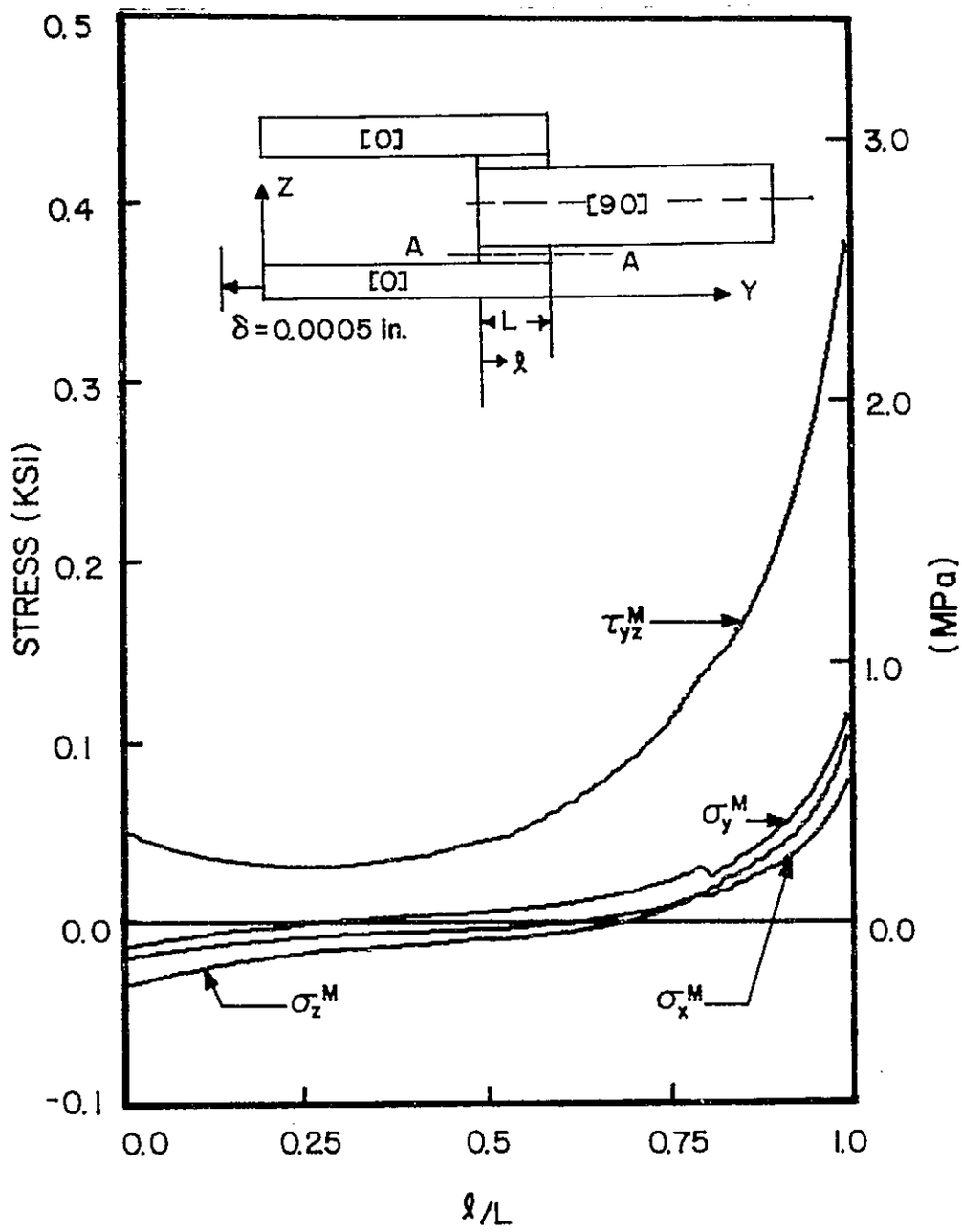

Figure 20. Elastic Mechanical Adhesive Stresses of a Double Lap Joint with [0] and [90] Gr/Pi Adherends and Metlbond 1113 Adhesive

(Fig. 15) shows lower peak stress values and a more uniform distribution of stresses for the double lap joint. A striking similarity between these two joints is the location of the peak stress values corresponding to a line near $\ell/L = 1.0$. In the double lap joint, as in the single lap, this is due to the increased relative displacement v_r at the line $\ell/L = 1.0$. It is interesting to note that the restrictions on the displacements in the z direction in the double lap do not greatly decrease the relative difference in peak stresses near $\ell/L = 0$ and $\ell/L = 1.0$ in comparison to the single lap joint, indicating that the effects of bending are also small for the double lap joint.

The curing stresses for this double lap joint are presented in Fig. 21. This figure shows that the σ_z^T curing stresses are very small while the τ_{yz}^T stresses are approximately 90 percent of the ultimate shear strength. Comparing these stresses to those for a single lap joint of the same adherends (Fig. 17) indicates that for curing stresses, the restrictions upon displacements at the midsurface of the inner adherend in the double lap joint are not necessarily helpful. The double lap joint produces higher shearing stresses, but lower peel stresses than those of the single lap joint. The only difference between the two joints is the increased bending stiffness of the inner adherend in the double lap. This indicates that bending stiffness is an important factor in these curing stresses. This must also be the cause for differences in the σ_x^T and σ_y^T curing stresses of the two joints.

5.5.3 Single Lap Joints without Adhesives

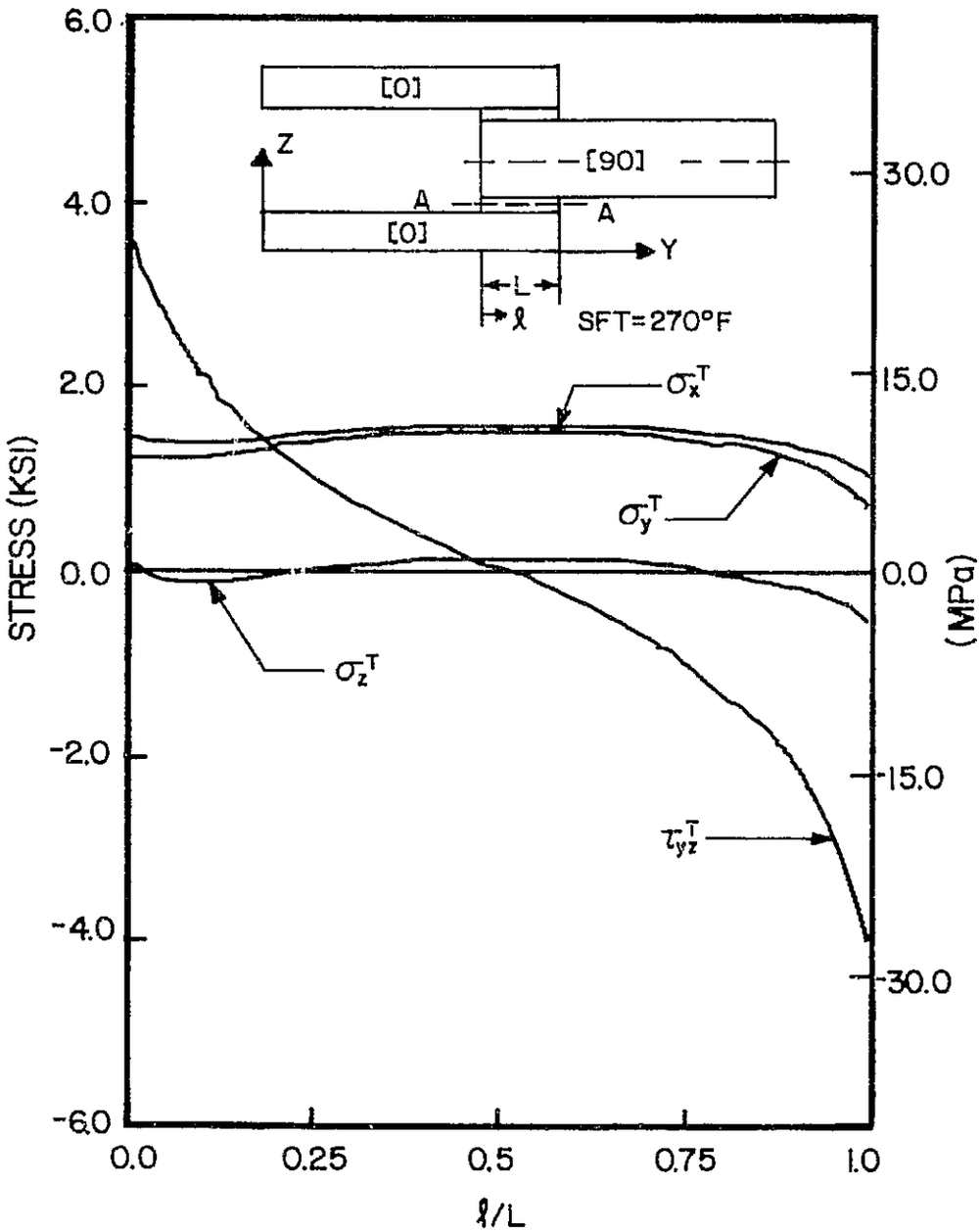

Figure 21. Elastic Curing Adhesive Stresses of a Double Lap Joint with [0] and [90] Gr/Pi Adherends and Metlbond 1113 Adhesive

Before presenting the first set of results in this section it should be pointed out once more exactly how the following stresses were averaged (see section 5.2). For the case of stresses which must be continuous across the interface between the adherends, the stresses presented are an average of the elemental stresses above and below this interface. For stresses which need not be continuous, the results presented consist of elemental stresses averaged either above or below the interface, thus two σ_x and σ_y curves are presented for each joint. This will also be the case for the stress results in the next section.

5.5.3.1 [0] Graphite-Polyimide Adherends

Fig. 22 presents the interfacial stresses of a single lap joint with [0] graphite-polyimide adherends and no adhesive. These stress distributions are interesting in that the shear stress τ_{yz} is not the dominant stress as it was in the joints with adhesives. For this joint it is seen that the σ_y^M upper and lower stresses are of greater magnitude and that σ_z^M attains higher peak values than the shearing stresses. For this joint τ_{yz}^M appears to be nearly uniform along the interface at a relatively low value. Due to the strength of the [0] laminates in the fiber direction it would appear that failure would initiate as a result of the peel stresses σ_z^M.

Curing stresses are not presented for this joint as they do not exist. The finite element solution was also checked on this point with the results being zero as required.

5.5.3.2 [90] Graphite-Polyimide Adherends

Mechanically induced interfacial stresses of a single lap joint

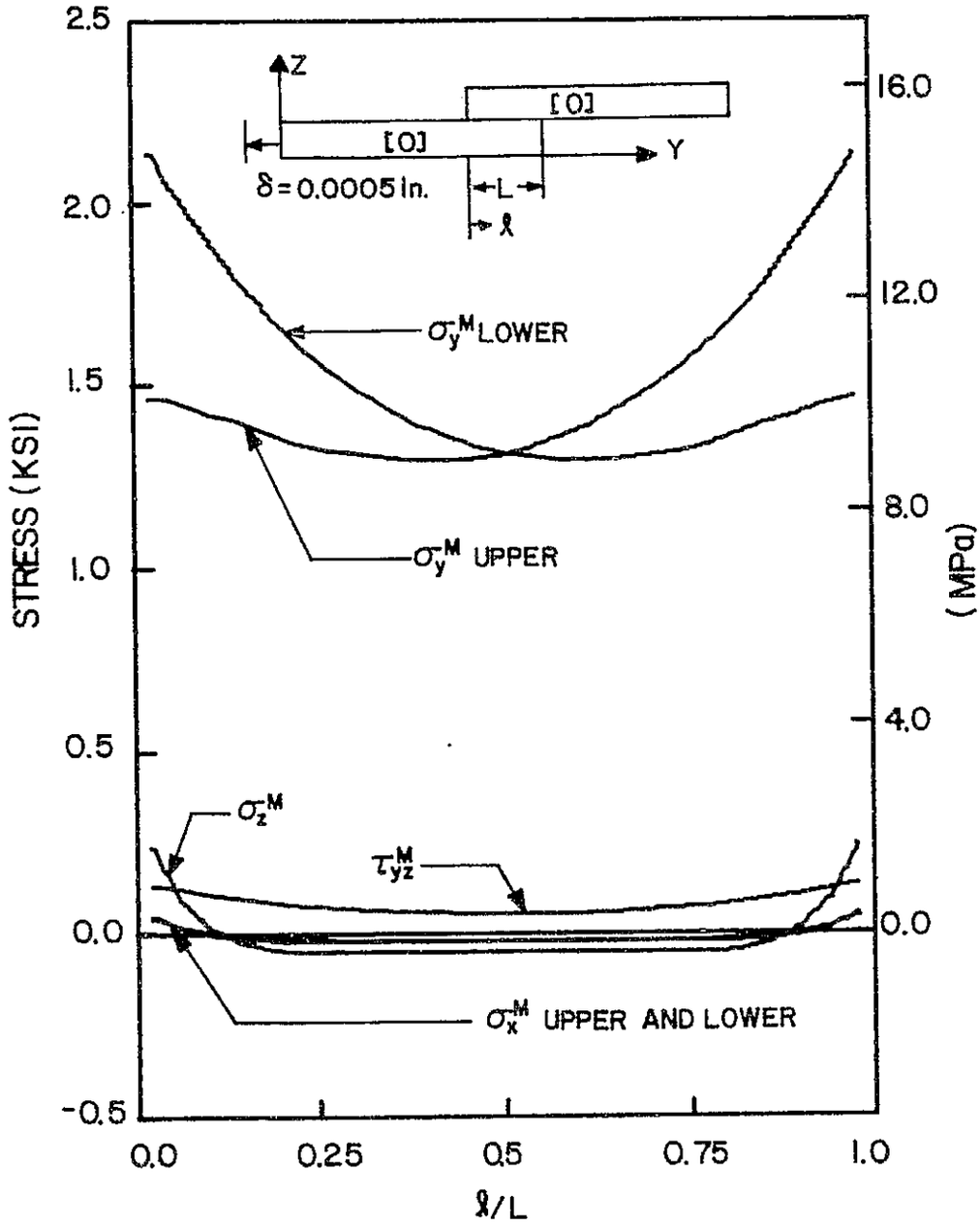

Figure 22. Elastic Mechanical Interfacial Stresses of a Single Lap Joint with [0] Gr/Pi Adherends and no Adhesive

with [90] graphite-polyimide adherends are presented in Fig. 23. These distributions show the same trends as the previous joint with the σ_y^M upper and lower stresses being the largest, σ_z^M reaching a relatively high peak, and τ_{yz}^M showing a nearly smooth distribution. Comparing Fig's. 22 and 23 it is seen that the larger stress values occur with the stiffer adherends as was the case for all of the adhesive bonded joints in previous sections.

5.5.3.3 [0] and [90] Graphite-Polyimide Adherends

Fig. 24 is a plot of interfacial stresses for a joint with [0] and [90] graphite-polyimide adherends under mechanical loading. As with the previous two joints, the internal stresses σ_y^M upper and lower are the largest in magnitude. It is interesting to note that for this joint the peak stresses do not necessarily occur with the more flexible adherend, as was true for adhesive bonded joints. For this joint σ_z^M and σ_y^M lower have peak values near $\ell/L = 0$ while τ_{yz}^M and σ_y^M upper have peaks near $\ell/L = 1.0$. Further examination of Fig. 24 indicates that the internal stresses are highest in the direction of the fiber in these unidirectional laminates. Thus σ_y^M is larger for the [0] adherend than in the [90] adherend while σ_x^M is larger for the [90] adherend.

Curing stresses for this joint are presented in Fig. 25. The magnitudes of the σ_x^T stresses in the [0] adherend are nearly 60 percent of the ultimate strength of laminate which represents a significant curing stress. The σ_y^T curing stresses in the [90] adherend are also large at 40 percent of ultimate. The other internal components of

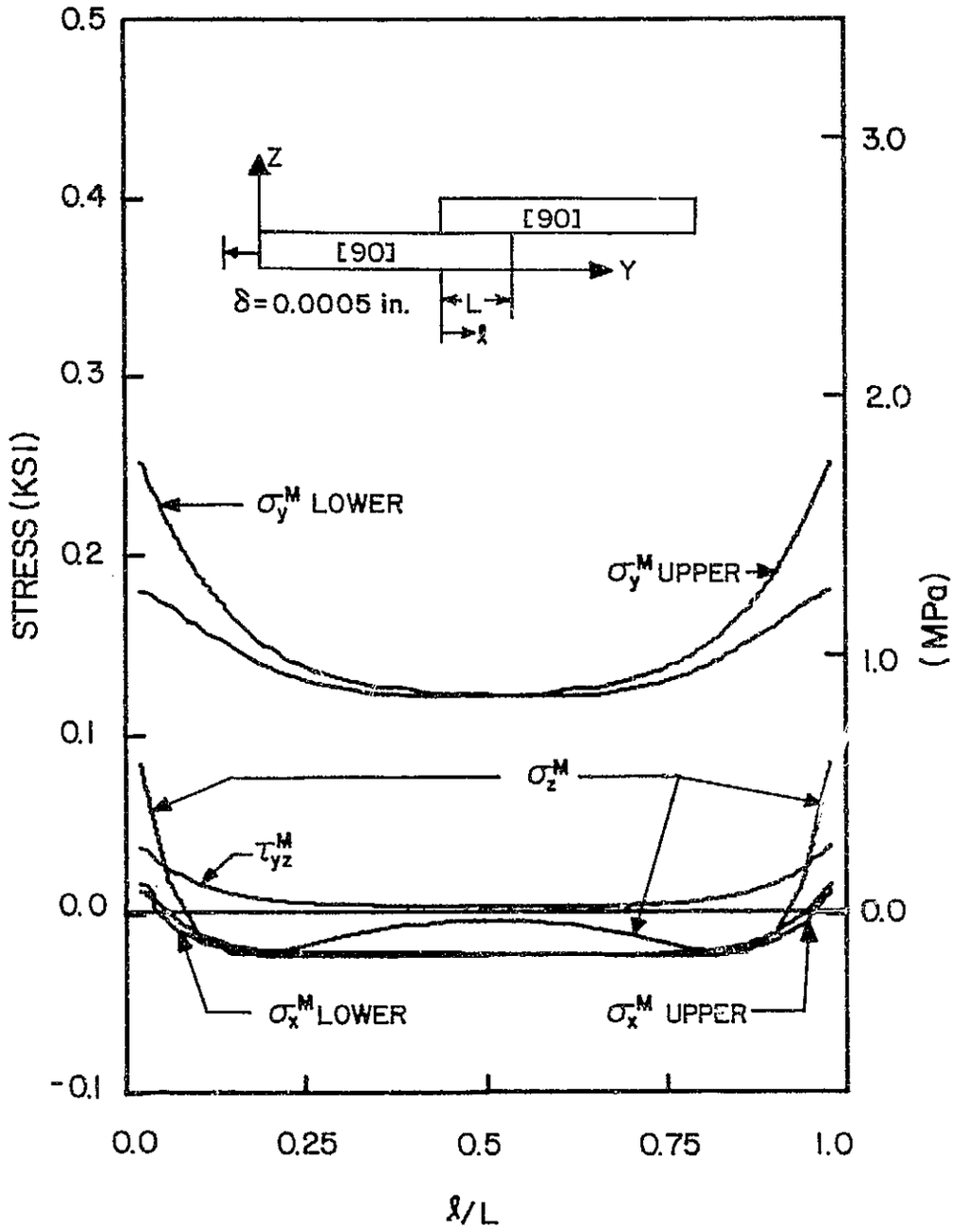

Figure 23. Elastic Mechanical Interfacial Stresses of a Single Lap Joint with [90] Gr/Pi Adherends and no Adhesive

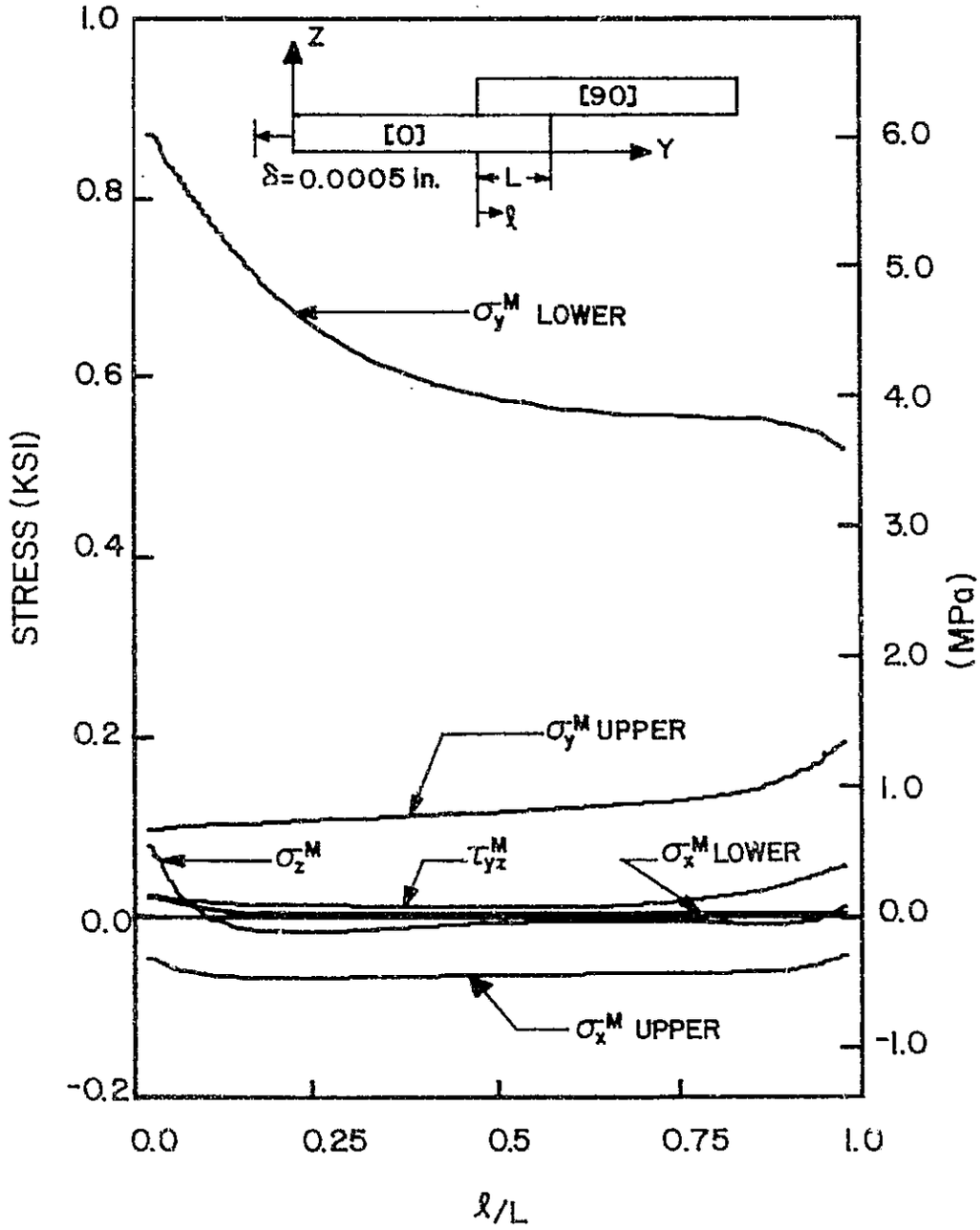

Figure 24. Elastic Mechanical Interfacial Stresses of a Single Lap Joint with [0] and [90] Gr/P: Adherends and no Adhesive

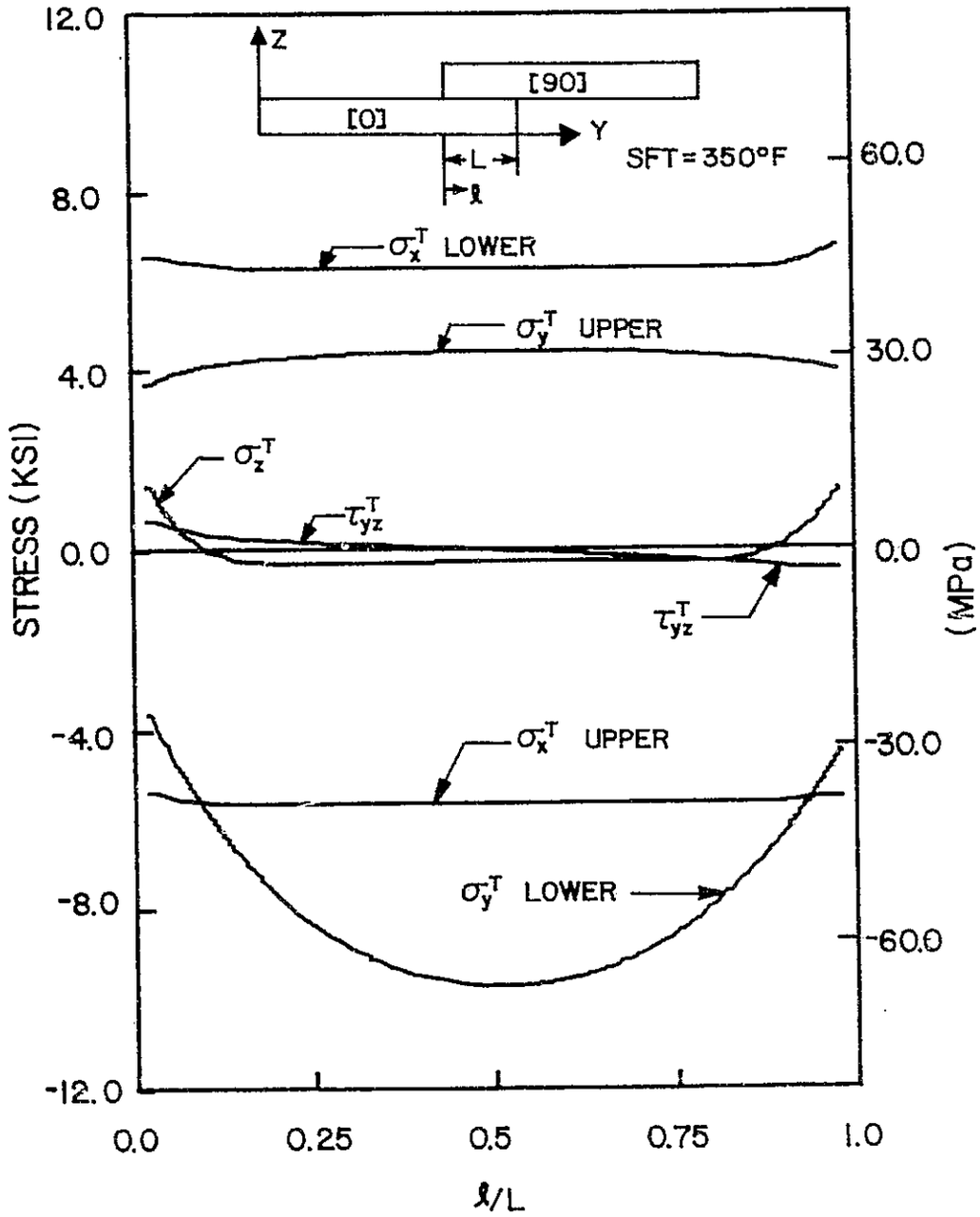

Figure 25. Elastic Curing Interfacial Stresses of a Single Lap Joint with [0] and [90] Gr/Pi Adherends and no Adhesive

stress σ_x^T upper and σ_y^T lower are of comparable numerical value, but are in the fiber direction of their respective adherends and therefore do not represent such significant percentages of the ultimate strengths. This figure shows that equilibrium appears to be satisfied by the σ_z^T and τ_{yz}^T curing stresses.

5.5.4 Double Lap Joints without Adhesives

Fig's. 26 and 27 represent mechanically induced interfacial stresses for double lap joints with [0] and [90] graphite-polyimide adherends respectively. These joints show higher stresses with the stiffer adherends as with all other joints presented. It can be seen that with these joints the σ_y^M stresses are the largest as has been shown for all joints without adhesives.

Comparing Fig's 22 and 26 it can be seen that the double lap joint has higher stresses for the same displacement loading. This can only be caused by the increased bending stiffness of the inner adherend in the double lap joint. This trend is also present in comparison of Fig's. 23 and 27 representing joints with [90] adherends. For joints with adhesive layers the effect of the increased bending stiffness of the inner adherend was to smooth and reduce slightly the stress distributions for double lap joints in comparison to single lap joints.

Fig's. 28 and 29 represent the mechanical and curing stresses respectively for a double lap joint with [0] and [90] graphite-polyimide adherends. As with the single lap with [0] and [90] adherends and no adhesive, the peak stresses for mechanical loading do not occur with the

C-2

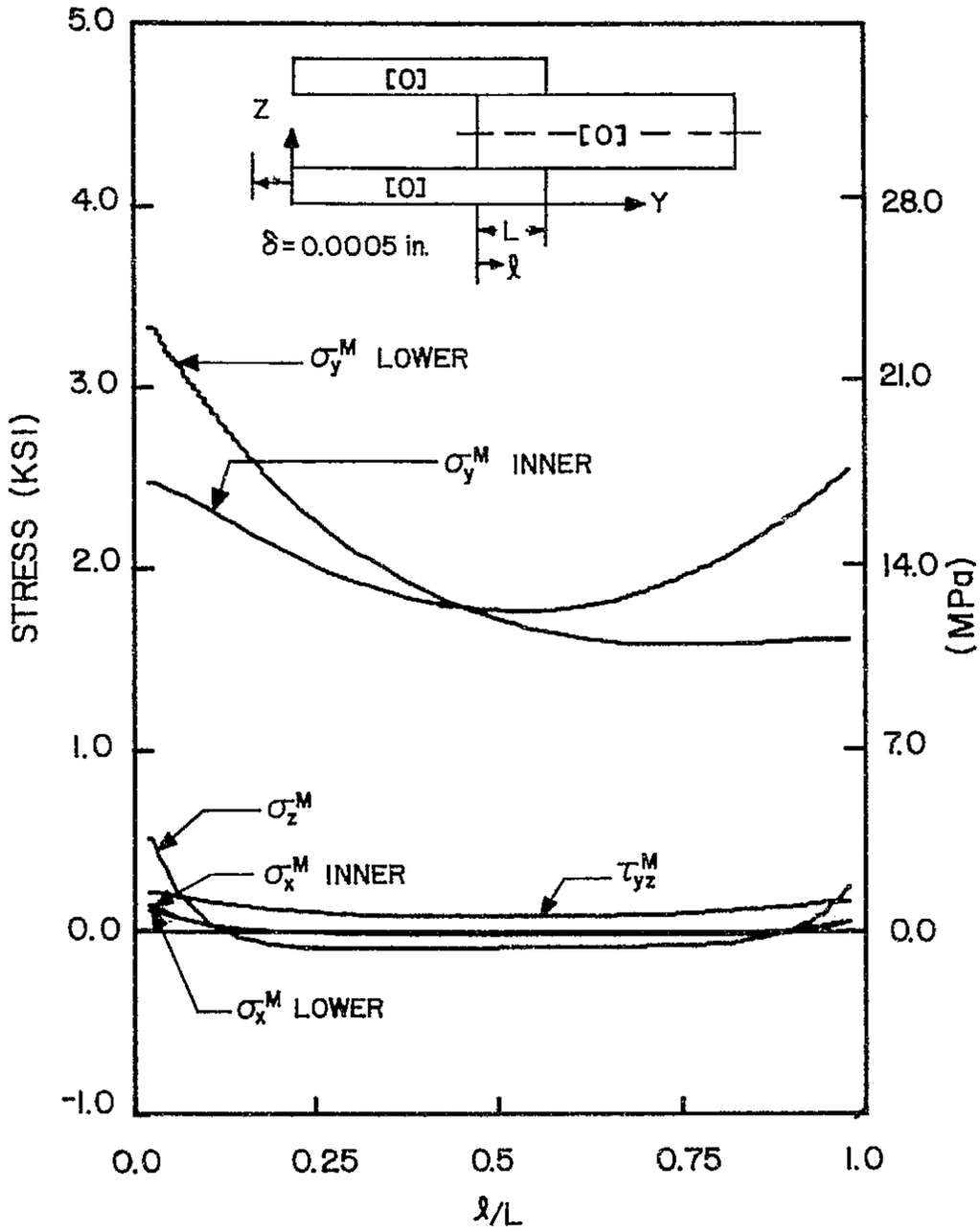

Figure 26. Elastic Mechanical Interfacial Stresses of a Double Lap Joint with [0] Gr/Pi Adherends and no Adhesive

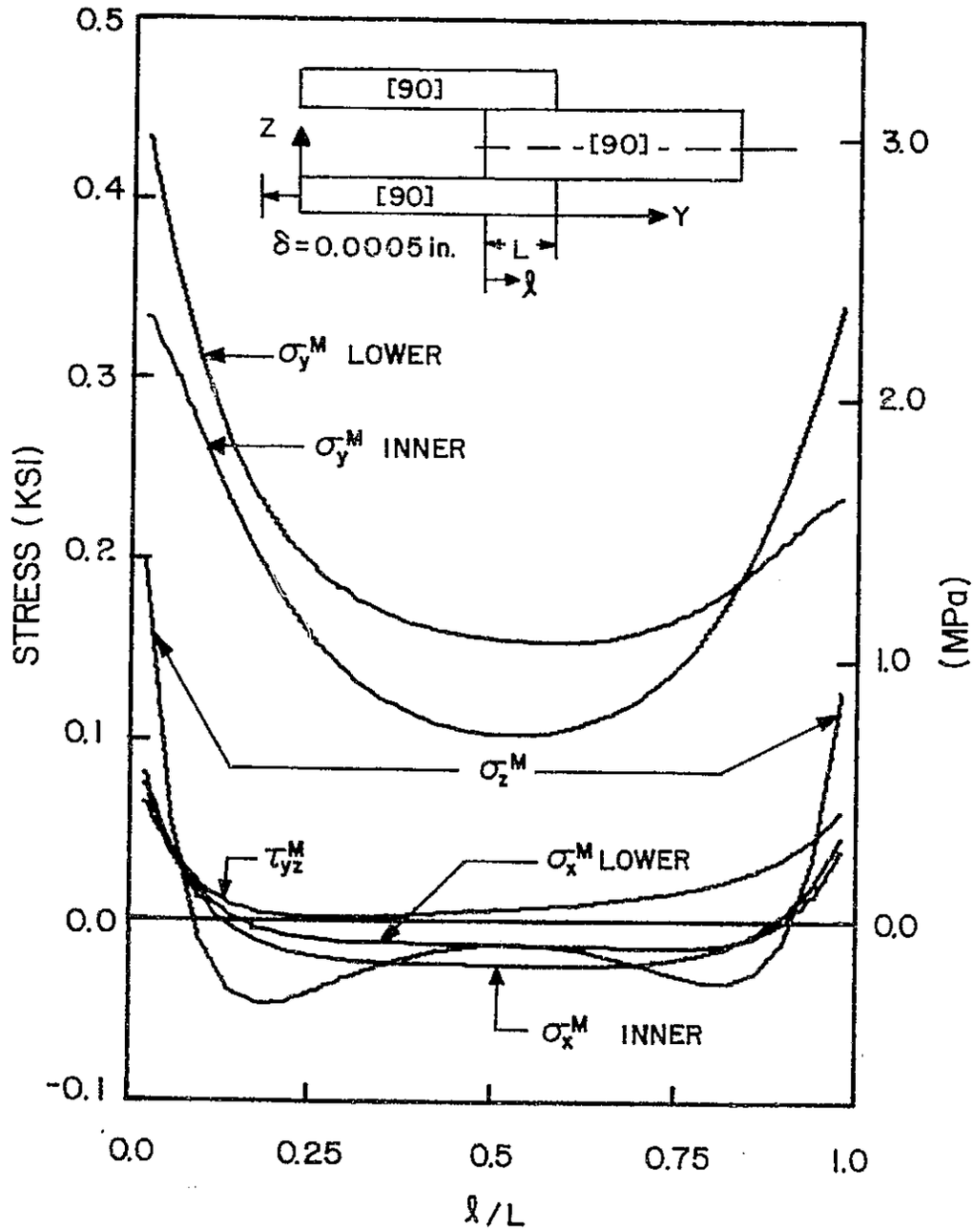

Figure 27. Elastic Mechanical Interfacial Stresses of a Double Lap Joint with [90] Gr/Pi Adherends and no Adhesive

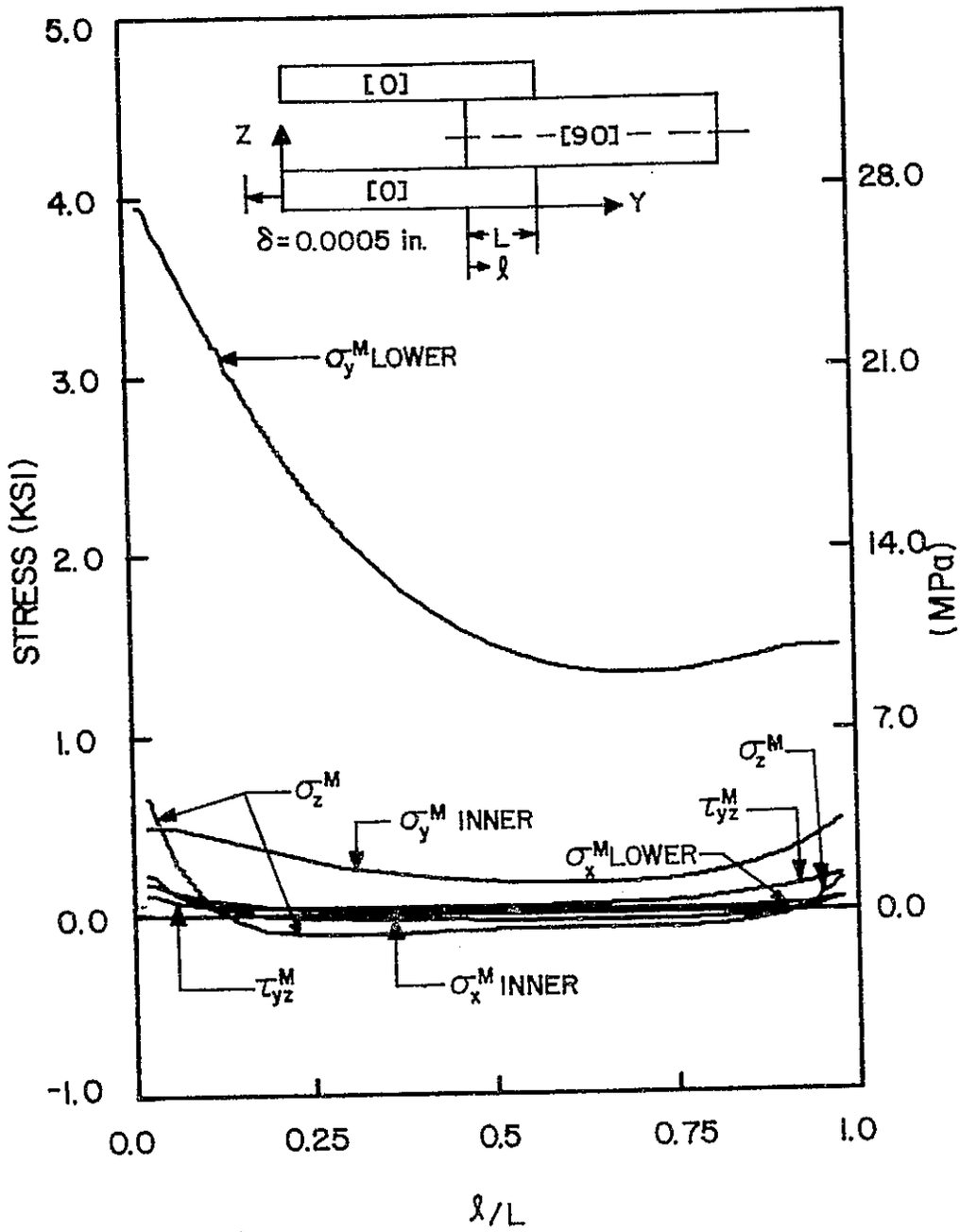

Figure 28. Elastic Mechanical Interfacial Stresses of a Double Lap Joint with [0] and [90] Gr/Pi Adherend and no Adhesive

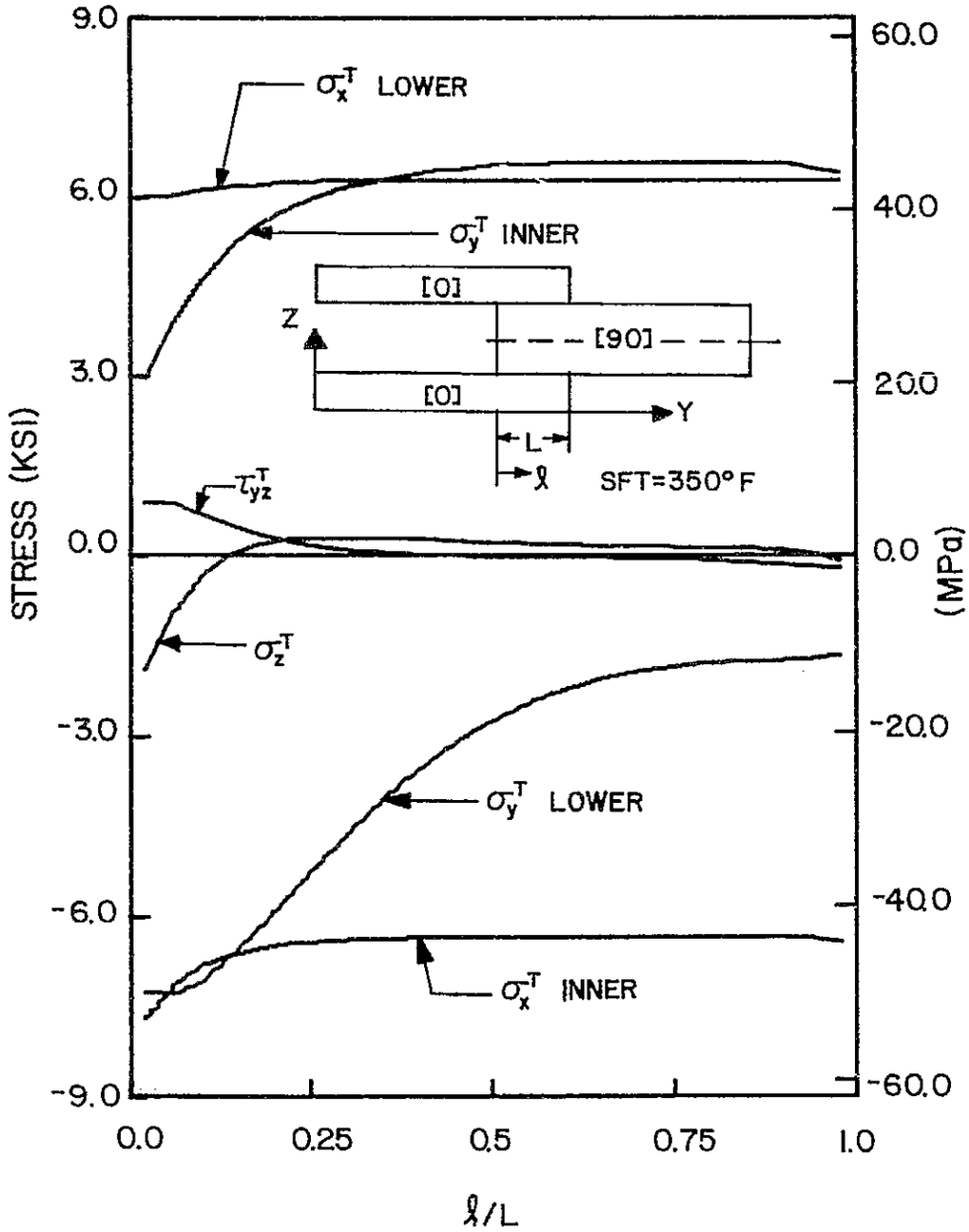

Figure 29. Elastic Curing Interfacial Stresses of a Double Lap Joint with [0] and [90] Gr/Pi Adherends and no Adhesive

more flexible adherend. This is again contrary to the results presented for lap joints with adhesive layers. The curing stress components σ_x^T for the [0] adherend and σ_y^T for the [90] adherend represent approximately 60 percent of ultimate strength for the laminates.

5.5.5 Elastic Loading Comparisons

After reviewing the stress distributions of the four previous subsections, interesting comparisons can be made by considering the force loading corresponding to the displacement applied for each of the joints. The results can be seen in Table 4. In this table the force load for double lap joints corresponds to the total load carried by the joint. The forces for all of the joints are calculated by averaging stresses in the elements at the ends of the adherends, multiplying by the thickness of the adherend, and assuming a unit depth.

Making comparisons of single and double lap joints with the same adherends it can be seen that the double lap joints carry more than twice as much force as the single lap joints. In the cases where the joints have adhesives, this can be seen as a beneficial effect of the increased bending stiffness of the inner adherend, as the peak stresses for double lap joints of this category are lower than for the single lap joints. The increased load carrying capacity is due to the more uniform shear stress distribution of the double lap joints, which creates a larger resultant force opposing the load.

Comparisons of single and double lap joints without adhesives also show a more than doubled load carrying capacity for the double lap

TABLE 4

Force-Displacement Result Comparisons for Elastic Joint Solutions

Type of Joint	Adherends	Adhesive Bonded	Applied Displacement	Corresponding Force
Single	[0], [0]	Yes	0.0005 in.	88.8 lb.
Single	[90], [90]	Yes	0.0005 in.	11.6 lb.
Single	$[0/\pm45/90]_s$, $[0/\pm45/90]_s$	Yes	0.0005 in.	38.9 lb.
Single	[0], [90]	Yes	0.0005 in.	20.9 lb.
Double	[0], [0], [0]	Yes	0.0005 in.	202.0 lb.
Double	[90], [90], [90]	Yes	0.0005 in.	24.4 lb.
Double	[0], [90], [0]	Yes	0.0005 in.	44.1 lb.
Single	[0], [0]	No	0.0005 in.	86.3 lb.
Single	[90], [90]	No	0.0005 in.	10.9 lb.
Single	[0], [90]	No	0.0005 in.	20.2 lb.
Double	[0], [0], [0]	No	0.0005 in.	244.2 lb.
Double	[90], [90], [90]	No	0.0005 in.	34.7 lb.
Double	[0], [90], [0]	No	0.005 in.	159.0 lb.

joints. However, in this case, the peak stresses are higher for the double lap joints making it unclear as to which joints are the more efficient.

5.6 Nonlinear Results

Bonded joint stress distributions presented in this section were predicted using the analysis of Chapter 3 and the nonlinear formulation of Chapter 4. Mechanical and thermal loading was applied as a series of increments. Where curing stresses are presented, they correspond to the total curing load. Mechanically induced stresses are presented at three load levels for each individual joint. The load levels for an individual joint do not necessarily correspond to those of other joints. The dimensions of the joints of this section are identical to those of the elastic results (Fig. 1) except where otherwise stated.

5.6.1 Single Lap Joints

5.6.1.1 Lap Shear Test

The adhesive shear stress and strain distributions for a lap shear test joint with aluminum adherends and Metlbond 1113 adhesive are shown in Fig's. 30 and 31 respectively. This joint corresponds to that used in Ref. [20] for determining the adhesive shear properties as used in this study. The dimensions of this joint are presented in Table 5.

These two figures (30 and 31) point to the effects of the nonlinear shear behavior of the adhesive. Examination of Fig. 30 reveals that as the displacement loading increases, the shear stress distribution becomes more uniform. Fig. 31, however, shows that the shear strain

TABLE 5

Dimensions for Lap Shear Joint and
Single Lap Joint with [0/90/0/90/0] B/E Adherends

Joint	Overall Length (In)	Overlap Length (In)	Adherend Thickness (In)	Adhesive Thickness (In)
Thick Adherend Lap Shear Test Joint	5.1	0.308	0.125	0.003
[0/90/0/90/0] Adherends	6.25	0.75	0.026	0.005

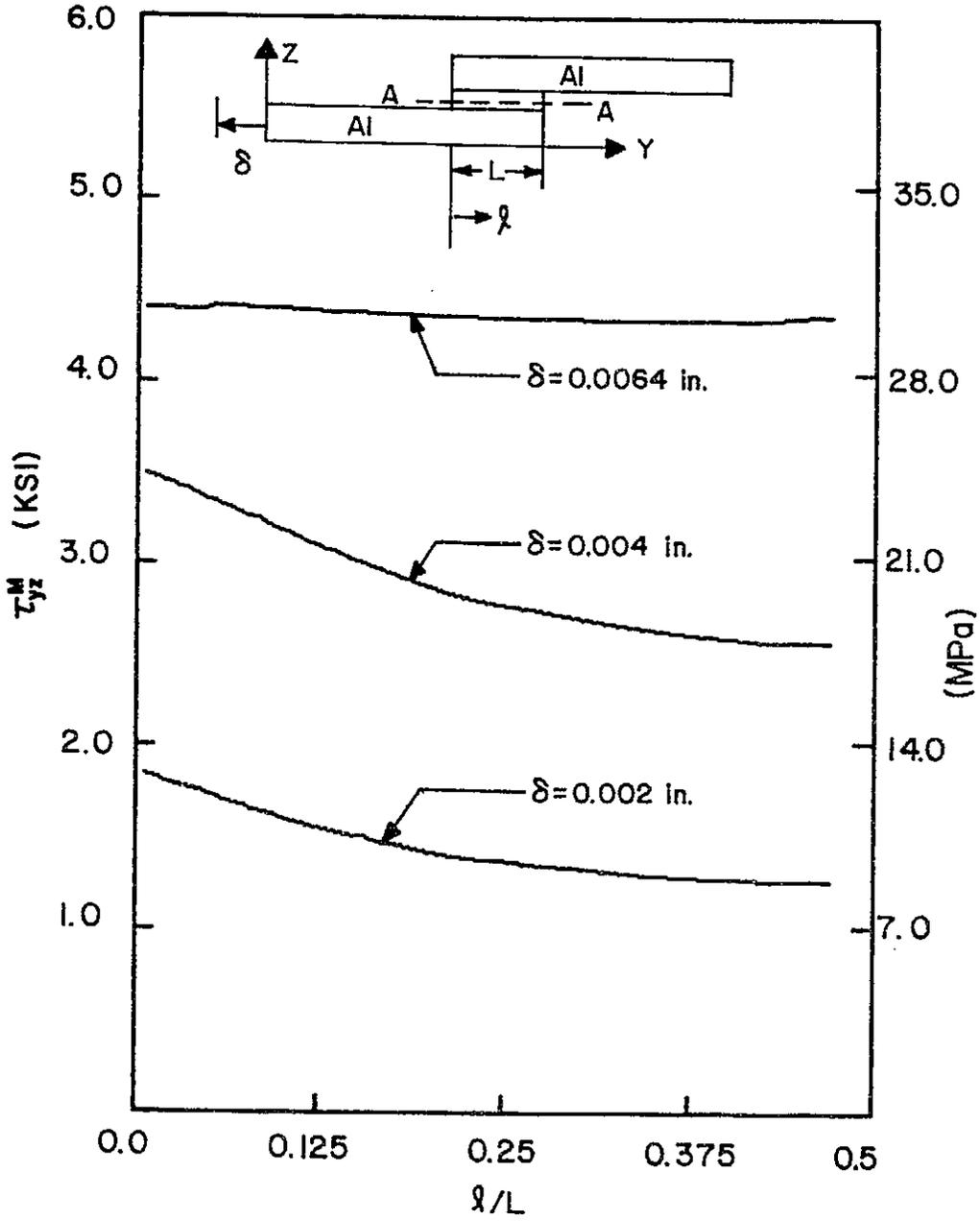

Figure 30. Nonlinear Mechanical Adhesive τ_{yz} Stresses of a Lap Shear Joint with Aluminum Adherends and Metlbond 1113 Adhesive

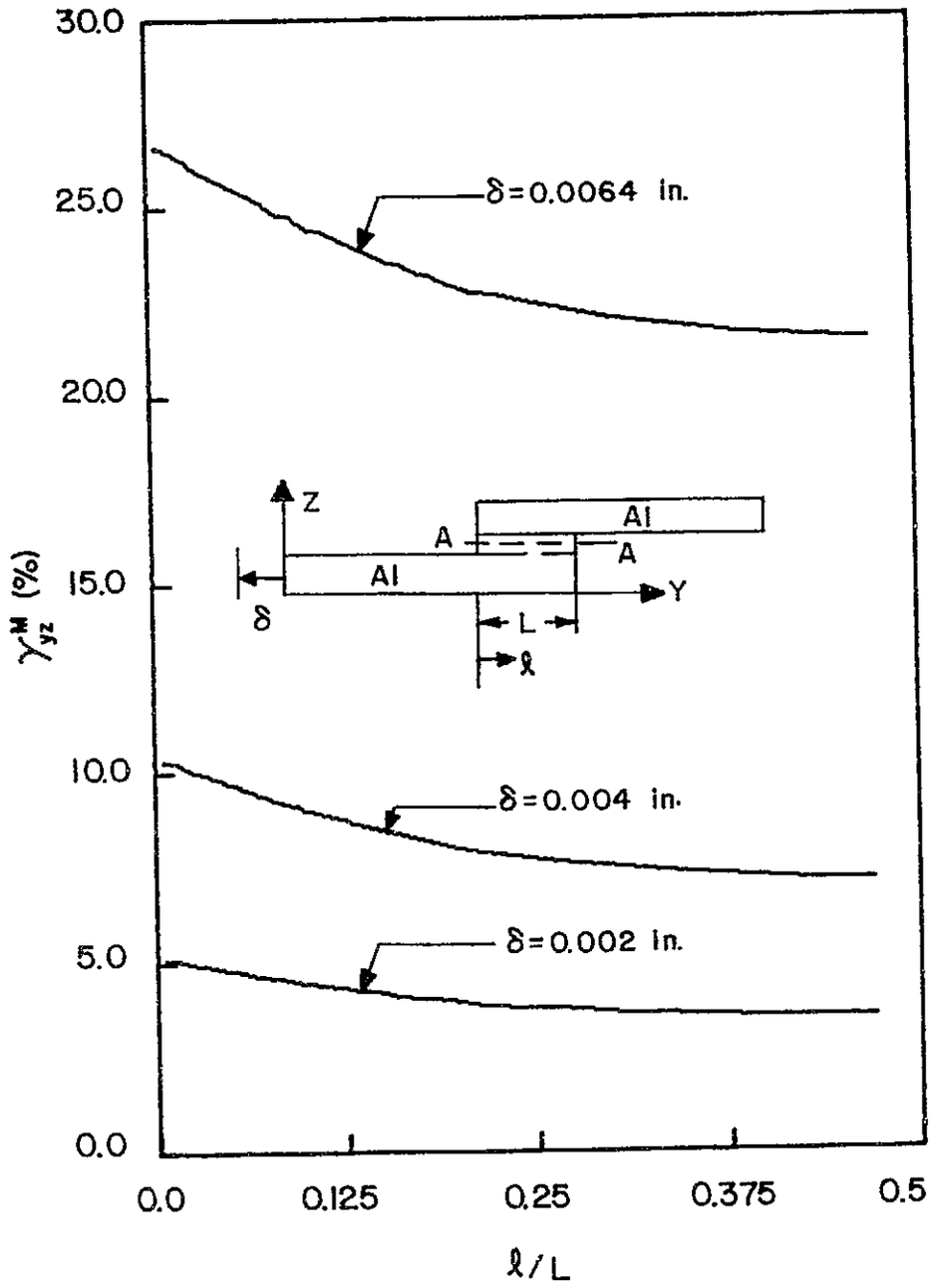

Figure 31. Nonlinear Mechanical Adhesive γ_{yz} Strains of a Lap Shear Joint with Aluminum Adherends and Metlbond 1113 Adhesive

distribution does not become more uniform as loading increases. This can be explained by considering the shear stress-strain response of the adhesive (Appendix C, Fig. C.6). The slope of this curve becomes much smaller as the strain is increased. Therefore, in the bonded joint, the increment of stress corresponding to an increment of strain, at high strain levels, is smaller than at low strain levels. Thus, the shear stress distribution in the center of the joint is increasing more rapidly as loading increases than at the edges ($\ell/L = 0$ and $\ell/L = 1$), because the strains are higher at the edges. It is interesting to note that the largest shear stress presented (Fig. 30) is nearly a constant value. This value corresponds to the ultimate shear strength of the adhesive.

As was stated earlier, this joint corresponds to a joint used in the lap shear tests [20]. Therefore, comparisons between numerical and experimental work were made and the results can be found in Table 6 and Fig. 32.

The experimental stresses and strains presented in Table 6 are values corresponding the maximum stress of the adhesive shear curve. These stress and strain values are chosen for the comparison because of the nature of both the Ramberg-Osgood [17] approximations, and the finite element analysis. The Ramberg-Osgood parameters cannot model the stress-strain curve beyond the point at which the slope becomes zero and the finite element formulation does not produce a positive definite stiffness matrix when a negative modulus is used.

In Table 6, the numerical strain chosen for the comparison was near

TABLE 6

Comparison of Numerical and Experimental Results
for Single Lap Shear Joint

	Max Adhesive Shear Strain (%)	Max Adhesive Shear Stress (ksi)	Failure Load (kips)
Numerical	27	4.4	1.35
Experimental [20]	29*	4.4*	1.36
Percent Difference	7%	0%	0.7%

* Corresponds to maximum stress value

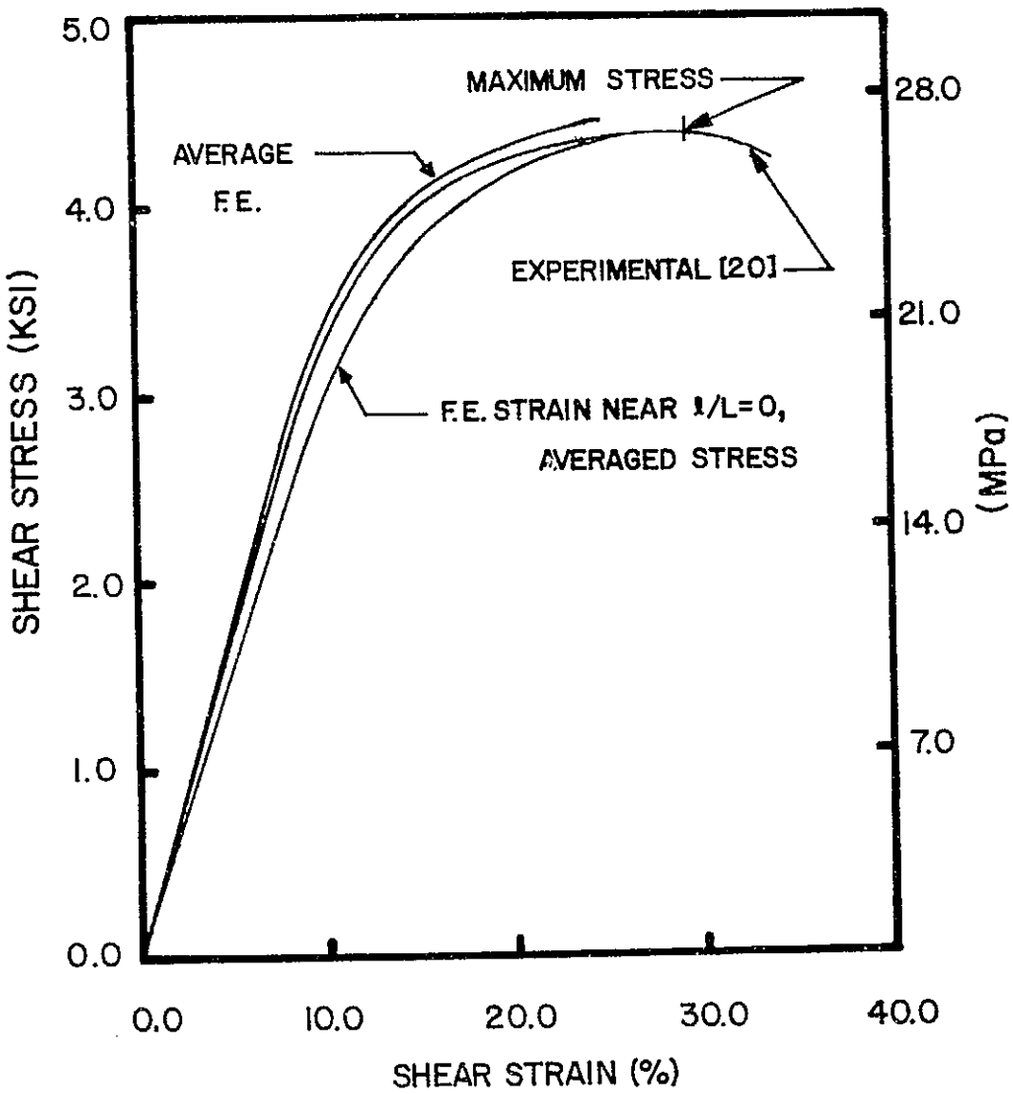

Figure 32. Comparison of Shear Stress-Strain Response of Metlbond 1113 Adhesive

the line $\ell/L = 0$. This is also the region where the strain was determined in Ref. [20]. This table shows good correlation between experimental results and the numerical prediction. In Fig. 32 two finite element stress-strain responses are presented. In both of these finite element curves, the stress corresponds to an average of elemental stresses throughout the adhesive layer.

The upper numerical curve (AVE.F.E.) presents strains that are also averaged over the entire adhesive layer. The lower numerical curve (F.E. STRAIN NEAR $\ell/L = 0$, AVERAGED STRESS) shows strains corresponding to the finite elements adjacent to the line $\ell/L = 0$ in the adhesive. The upper curve shows a better stress correlation while the lower curve shows a better ultimate strain correspondence with experimental data.

Fig's. 33, 34, and 35 present the σ_z^M, σ_y^M, and σ_x^M adhesive stresses of the same lap shear test joint under identical loadings. These figures do not show the effects of adhesive nonlinearity in such a pronounced fashion as Fig. 30. The reason for this is two fold. First, the extensional stress-strain response of the adhesive is not as nonlinear as the shear response. Secondly, the extensional stress values produced are not as large in magnitude relative to the ultimate strength. The maximum σ_z and σ_y stresses correspond to approximately 15 percent of the ultimate while the maximum σ_x component is approximately 10 percent of ultimate. Upon examination, Fig's. 34 and 35 reveal the discontinuity at $\ell/l = 0.2$ that was discussed in the elastic results (section 5.5.1.4). Thermal stresses are not presented for this joint as they would have no bearing on the comparisons made. This is because the

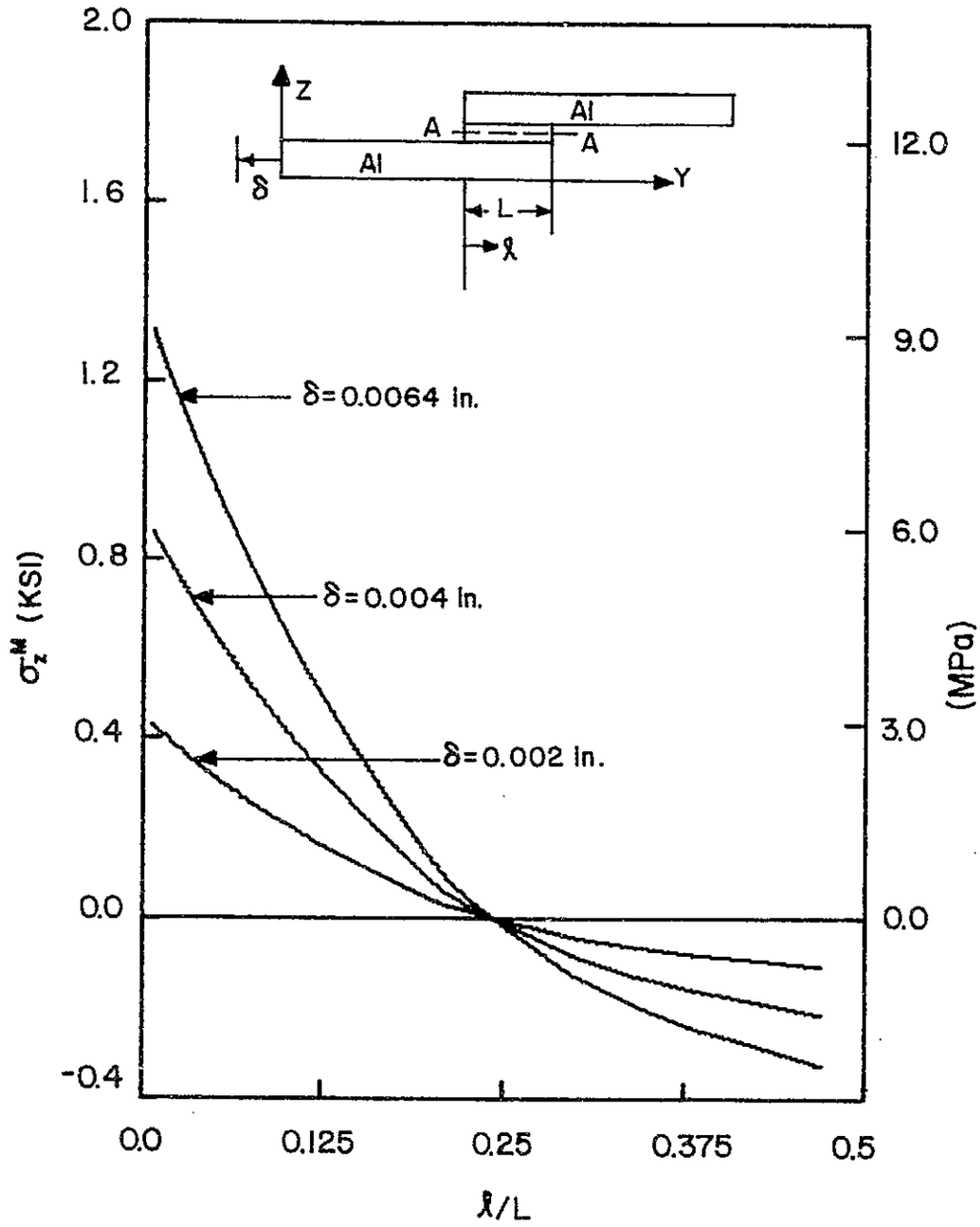

Figure 33. Nonlinear Mechanical Adhesive σ_z Stresses of a Lap Shear Joint with Aluminum Adherends and Metlbond 1113 Adhesive

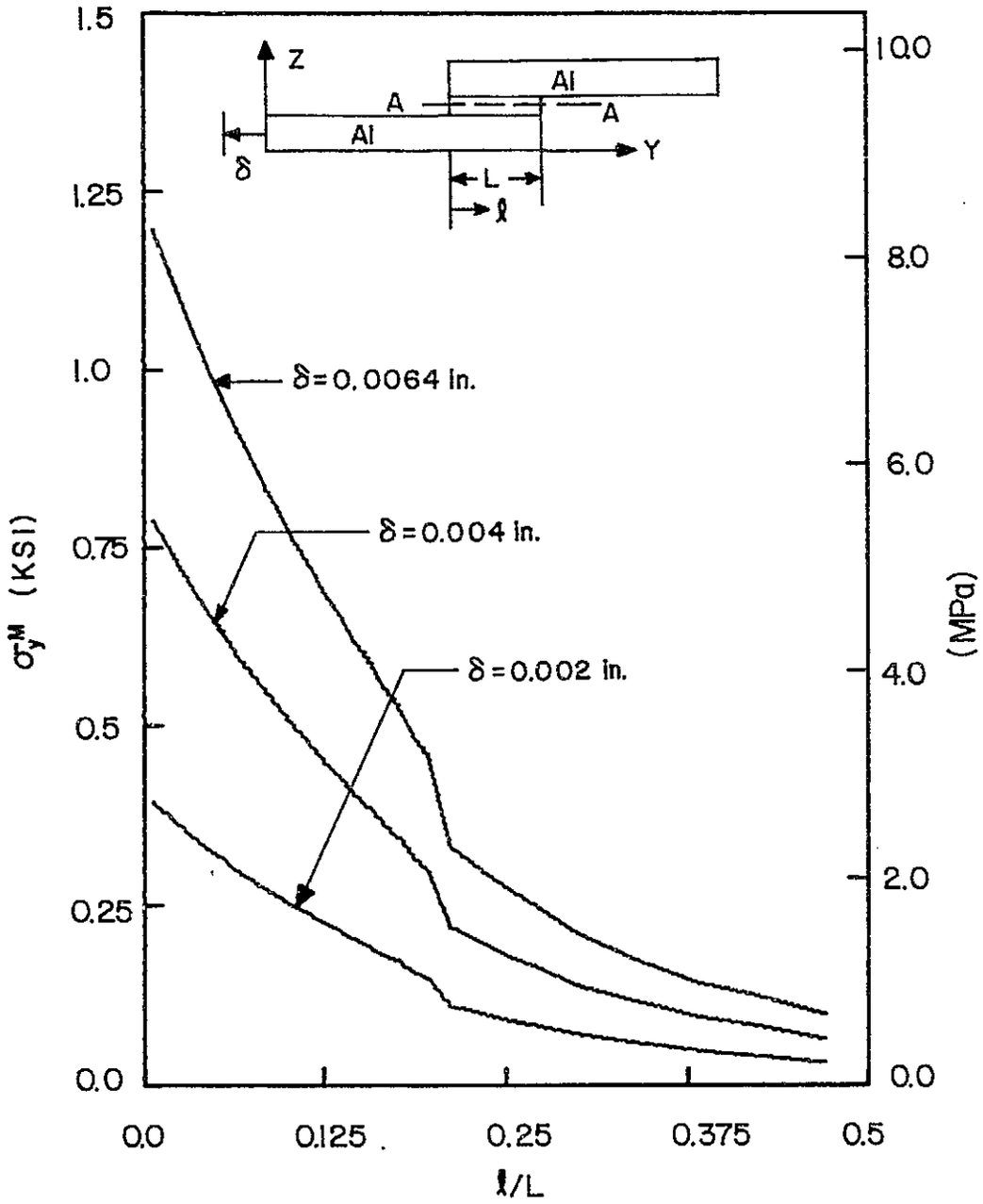

Figure 34. Nonlinear Mechanical Adhesive σ_y Stresses of a Lap Shear Joint with Aluminum Adherends and Metlbond 1113 Adhesive

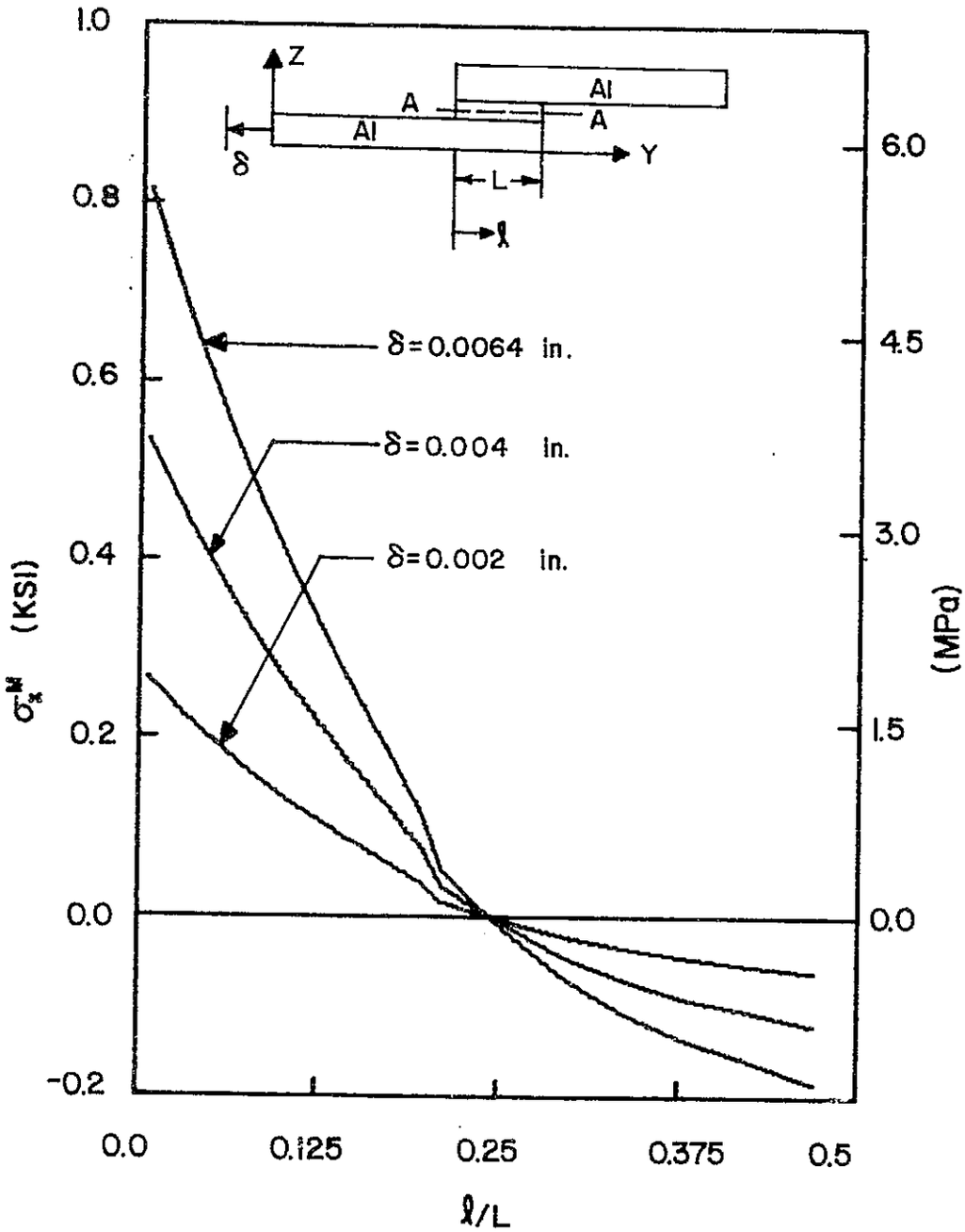

Figure 35. Nonlinear Mechanical Adhesive σ_x Stresses of a Lap Shear Joint with Aluminum Adherends and Metlbond 1113 Adhesive

shear properties produced from the experimental work on this joint [20] included any effects of curing.

An interesting comparison can be made concerning results obtained from the two different solution formulations presented in Chapter 3. In order to produce similar stress and strain distributions, it was necessary to apply a larger displacement load to the joint analyzed under the quasi 3-dimensional formulation. The additional load corresponded to 1/15 of the total displacement applied for the 2-dimensional solution. The resulting ultimate force loads were identical for the two analyses indicating that under the quasi 3-dimensional formulation the joint was more flexible and therefore capable of withstanding a larger displacement load.

5.6.1.2 [0/90/0/90/0] Boron-Epoxy Adherends and AF-126-2 Adhesive

This adhesive bonded joint was selected for analysis in order to compare the results of this study to those of Ref. [11]. For this comparison it was necessary to use a force loading instead of the displacement loading used for all other joints in this study. The force loading was required in order to exactly match the loading in [11]. In [11], two solution procedures are used. In the first, an iterative finite element analysis is used to account for material nonlinearities. The second procedure utilizes direct numerical integration of the governing differential equations for the joint. Results obtained by the second procedure are labeled as theoretical in the following figures. The dimensions of this joint are given in Table 5.

Fig's. 36 and 37 present the adhesive stress components τ_{yz}^{M} and σ_{z}^{M} respectively. In Fig. 36 it can be seen that the distributions of the shear stresses predicted by the present study compare favorably with the two distributions predicted in [11]. The principal difference is seen to be the magnitude of the peak stresses near the lines $\ell/L = 0$ and $\ell/L = 1$. It is interesting that none of the shear stress distributions presented in Fig. 36 satisfy the stress free boundary condition $\tau_{yz} = 0$ at $\ell/L = 1$. It appears that the areas under each of the three curves are approximately the same as required by equilibrium considerations.

In Fig. 37 it can be seen that the σ_{z}^{M} distributions predicted by the present study and theoretical results of [11] have significant differences. The present analysis predicts a symmetric distribution of peel stresses while the theoretical results [11] show peak stresses at $\ell/L = 0$ and $\ell/L = 1$ differing by more than 100 percent. The nonsymmetric nature of these results appears physically inconsistent as the adherends are identical. The finite element results presented in [11] do show the symmetry of stresses as predicted by this study. Another interesting aspect of the theoretical results is the reversal in sign of the peel stresses near $\ell/L = 1.0$. This is not seen in the finite element results of this study or [11].

Comparisons of the numerical values of the peel stresses cannot realistically be made as the extensional properties of the AF-126-2 adhesive were not known. The extensional Ramberg-Osgood coefficients used for this adhesive correspond to the extensional properties of

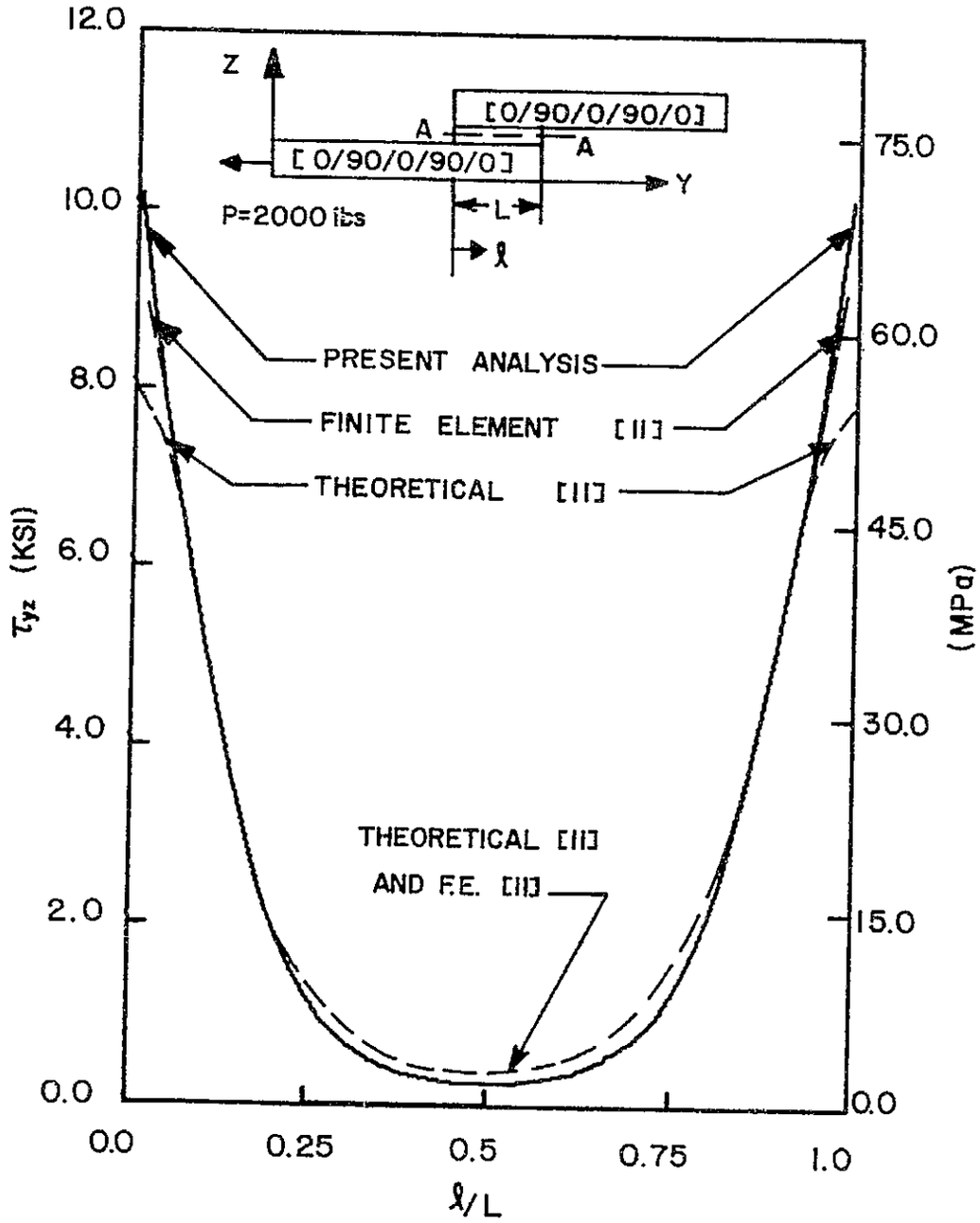

Figure 36. Nonlinear Mechanical Adhesive τ_{yz} Stresses of a Single Lap Joint with [0/90/0/90/0] B/E Adherends and AF-126-2 Adhesive

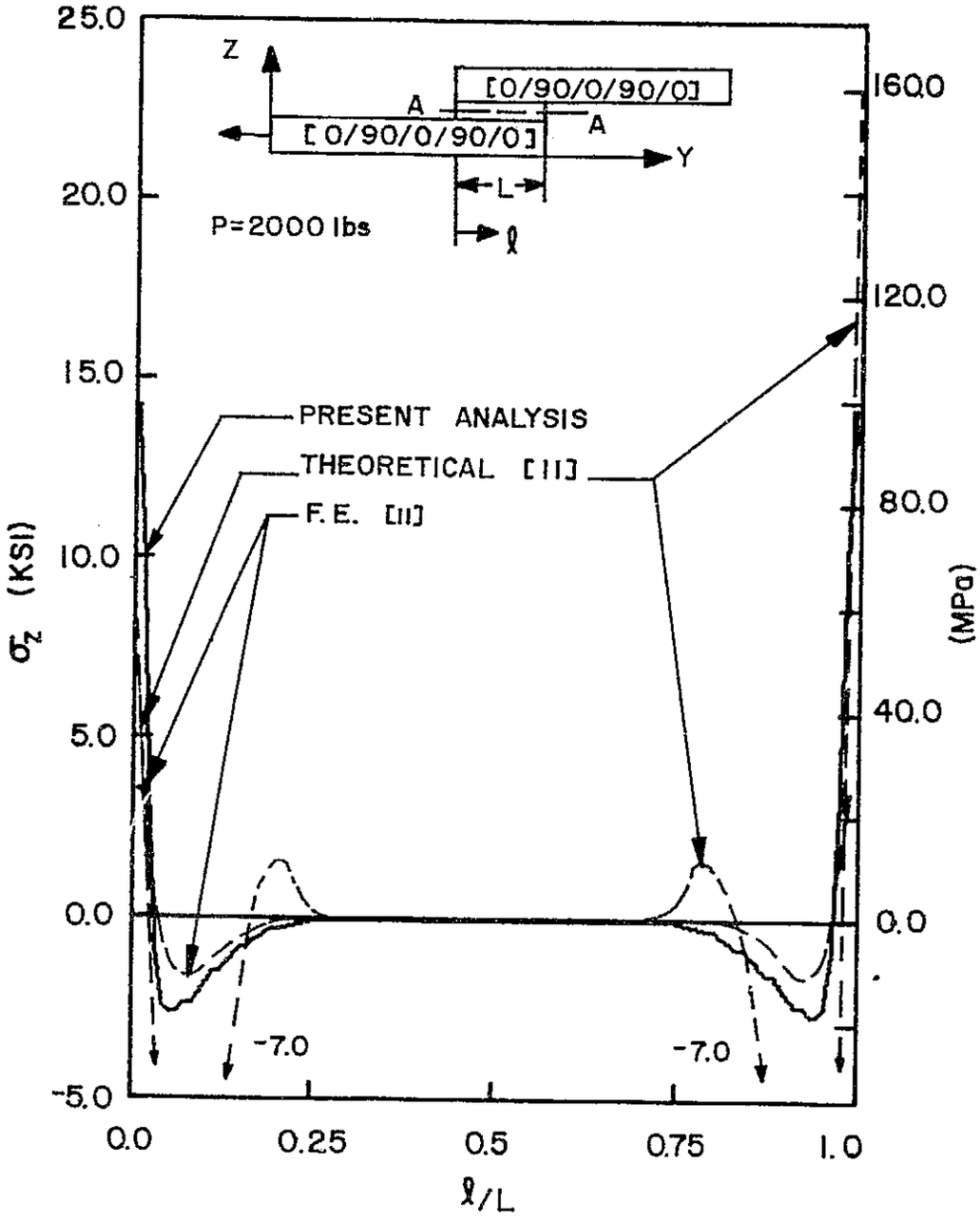

Figure 37. Nonlinear Mechanical Adhesive σ_z Stresses of a Single Lap Joint with [0/90/0/90/0] B/E Adherends and AF-126-2 Adhesive

Metlbond 1113.

Comparing Fig's. 36 and 37, it can be seen that for all solutions except the finite element solution of [11], the peel stresses are larger than the shear stresses. This verifies the statement made about the effects of the overlap length, L, upon the magnitudes of the shearing and peel stresses in an earlier section (5.5.1.1). For this joint, with a large adherend overlap, the peel stresses are dominant with respect to maximum value. If the magnitudes were compared with respect to ultimate strengths however, it is believed that the shearing stresses would again dominate. It is not known what these ultimate strenths are however, and therefore this comparison cannot be made.

The curing stresses for this joint are presented in Fig. 38. As was shown for the elastic results, the only significant curing stresses are σ_x^T and σ_y^T. This is again due to the identical adherends and the material properties of the adherends and adhesive. It is interesting that even though the values of the curing stress components σ_z^T and σ_{yz}^T are insignificant, they reach peak values nearly an order of magnitude larger than in any other joint with identical adherends. Since these curing components (σ_x^T and τ_{yz}^T) are negligible, the stresses presented in the previous two figures (36 and 37) can be considered either mechanical or combined mechanical and curing stresses.

The magnitudes of the curing components σ_x^T and σ_y^T with respect to the ultimate extensional strength of the adhesive is not known because as was stated earlier, this ultimate strength is not known. The analyses of [11] ignore the effects of curing, and while this does not affect

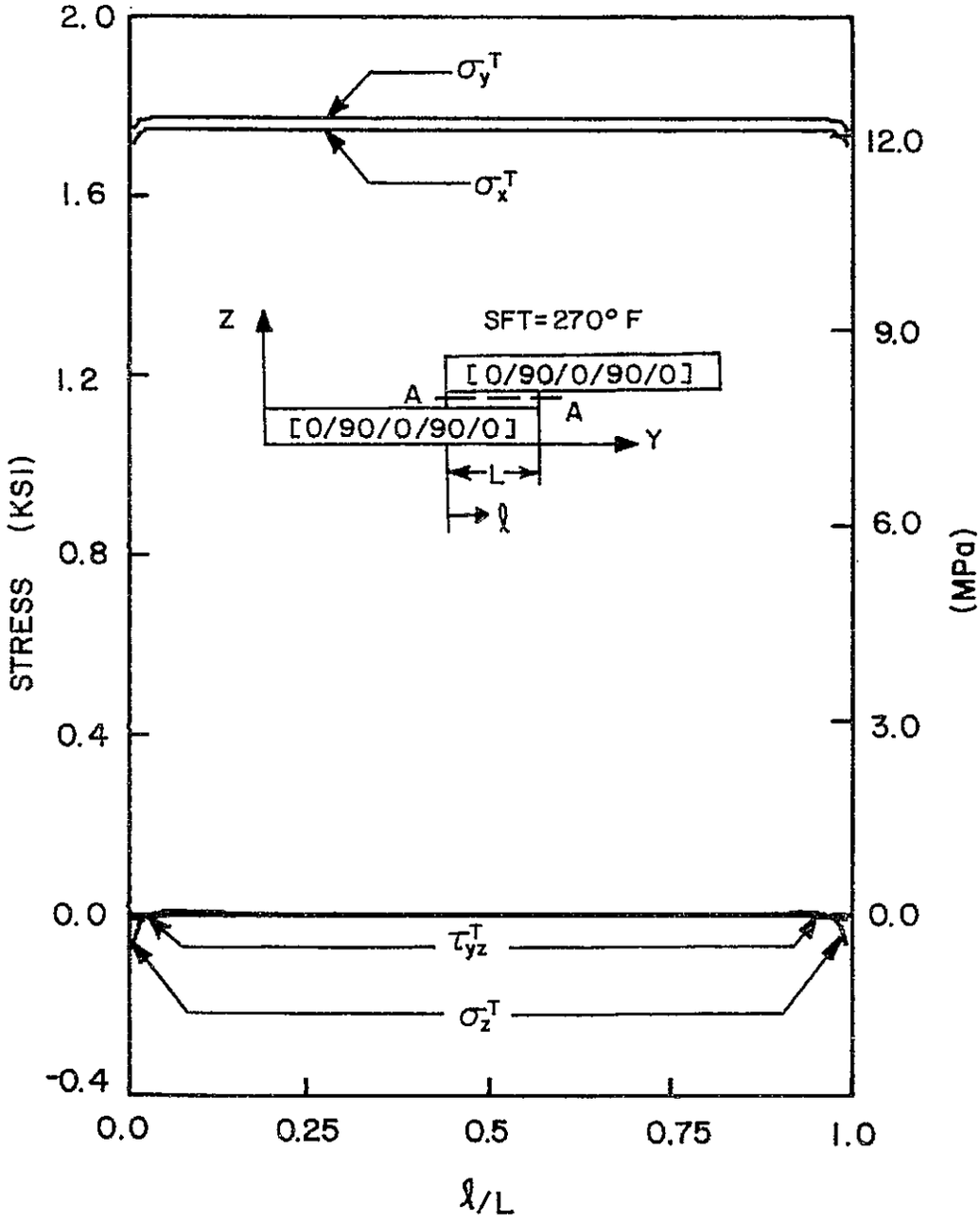

Figure 38. Nonlinear Curing Adhesive Stresses of a Single Lap Joint with [0/90/0/90] B/E Adherends and AF-126-2 Adhesive

the σ_z and τ_{yz} stress components, it can be seen that curing is significant in the two components of stress not presented in [11] (σ_x and σ_y).

Fig's. 39 and 40 present the combined mechanical and curing stresses, σ_y^{M+T} and σ_x^{M+T} of this joint. These distributions reveal that the curing stresses (Fig. 38) are of the same sign as the mechanically induced stresses and therefore would be detrimental to the performance of the joint under tensile loading.

5.6.1.3 [0] Graphite-polyimide Adherends and Metlbond 1113 Adhesive

Nonlinear curing stresses for this joint are not plotted as the significant components (σ_x^T and σ_y^T) are uniform throughout the adhesive. The numerical values for these stresses can be found in Table 7. This table presents a comparison between elastic and nonlinear results for this joint. For these curing stresses, the elastic solution underestimates the σ_x^T and σ_y^T components by 10 percent and 5 percent respectively.

The mechanical loading of this joint was analyzed utilizing the 2-dimensional formulation (Chapter 3). This was done because for this joint, the two formulations produce negligible differences in the stress components σ_y^M, σ_z^M, and τ_{yz}^M. The similarity in results is due to the relatively small difference in magnitudes of the adherend transverse stiffness (E_x) and the adhesive extensional stiffness. Combined mechanically and curing induced adhesive stresses are presented in Fig's. 41, 42, and 43. As in the lap shear joint (Fig. 30) only the adhesive

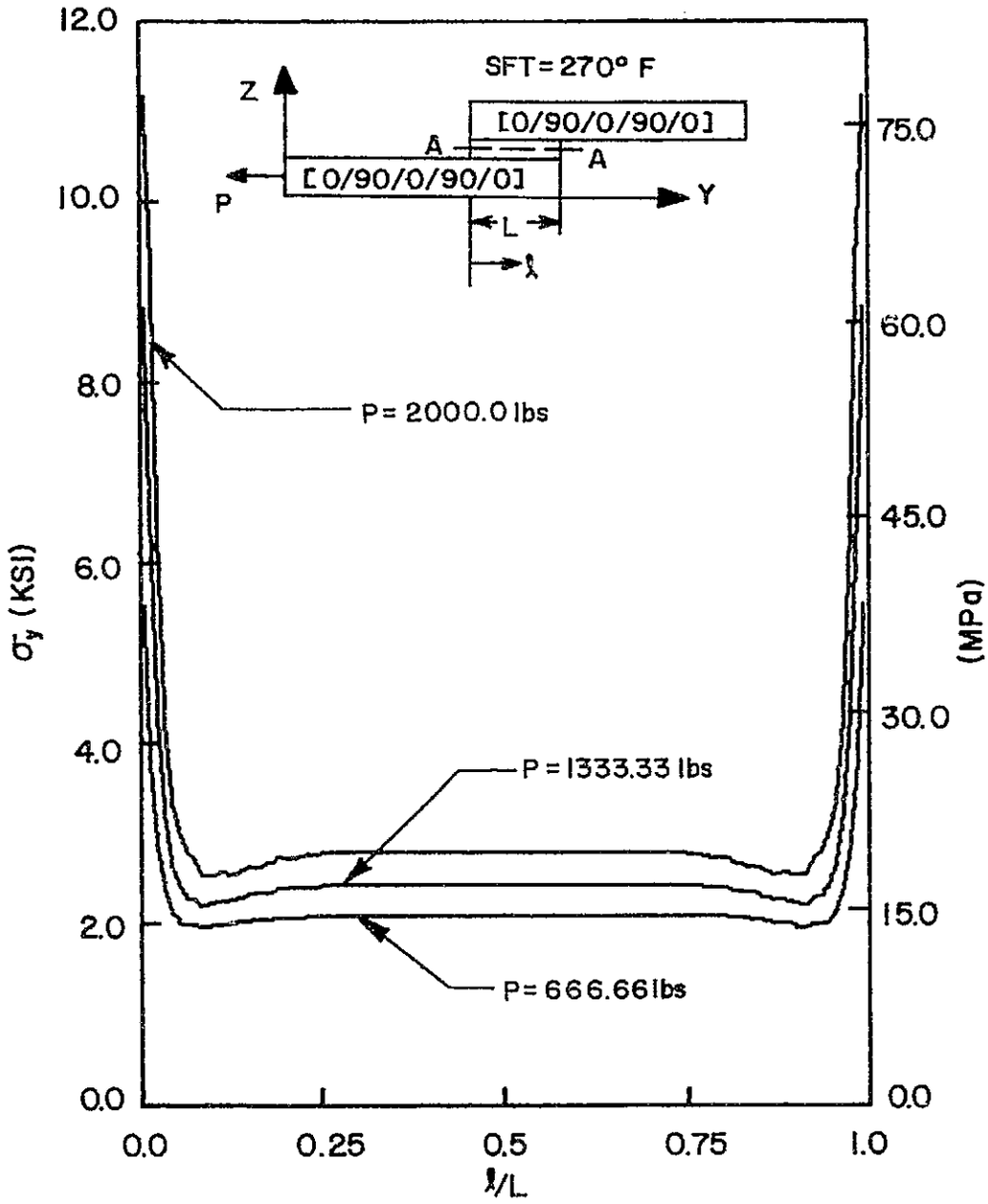

Figure 39. Nonlinear Mechanical and Curing Adhesive σ_y Stresses of a Single Lap Joint with [0/90/0/90/0] B/E Adherends and AF-126-2 Adhesive

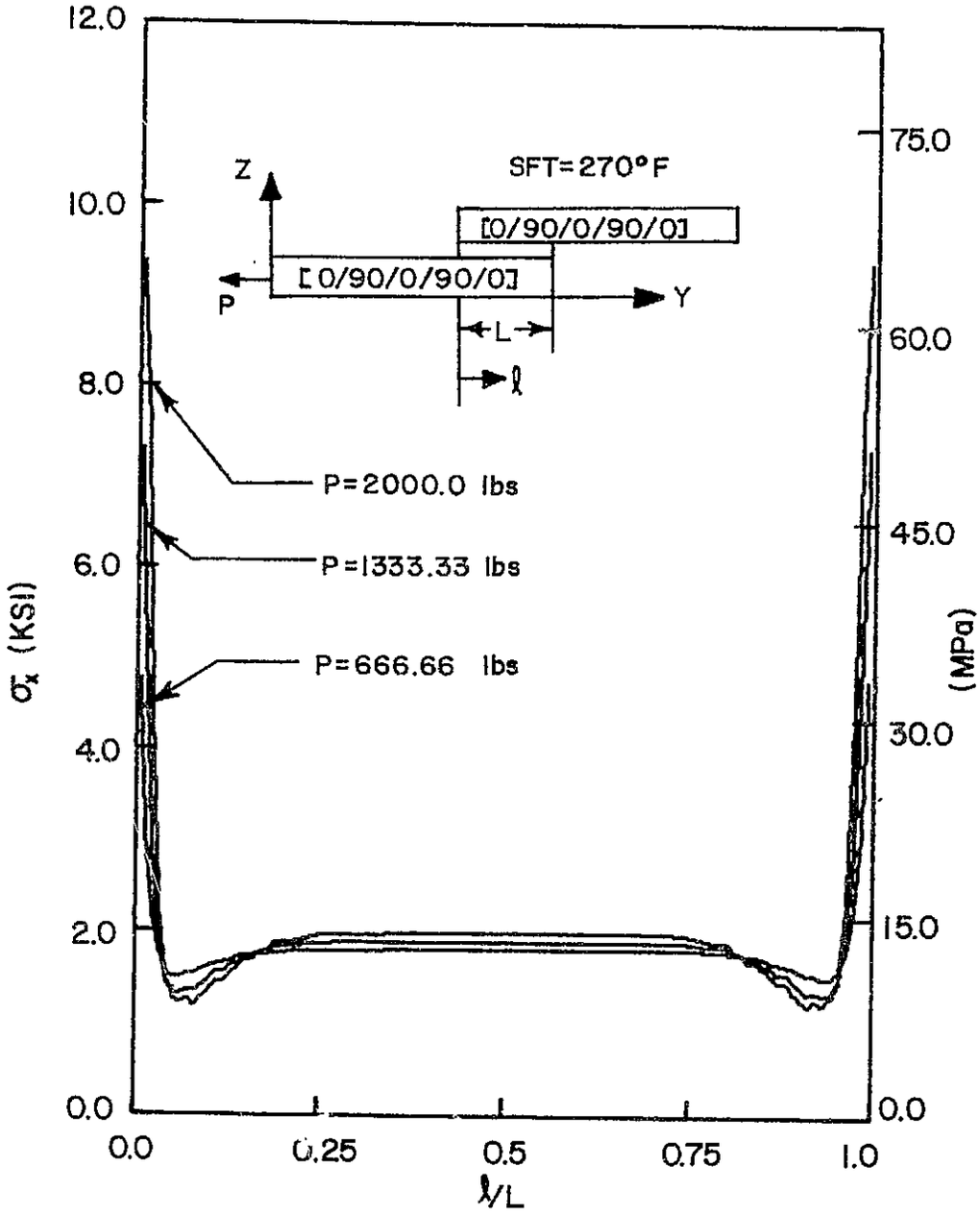

Figure 40. Nonlinear Mechanical and Curing Adhesive σ_x Stresses of a Single Lap Joint with [0/90/0/90/0] B/E Adherends and AF-126-2 Adhesive

TABLE 7

Comparison of Elastic and Nonlinear Adhesive Stresses for a Single Lap Joint with [0] Gr/Pi Adherends and Metlbond 1113 Adhesive

Type of Analysis	Curing Stresses SFT = 270°F (ksi)		Peak Mechanical Stresses (ksi)		
	σ_x	σ_y	σ_y	σ_z	τ_{yz}
Elastic	0.68	1.3	2.8	3.8	8.0
Non-linear	0.76	1.4	2.8	3.8	4.4
Difference	10%	5%	0%	0%	82%

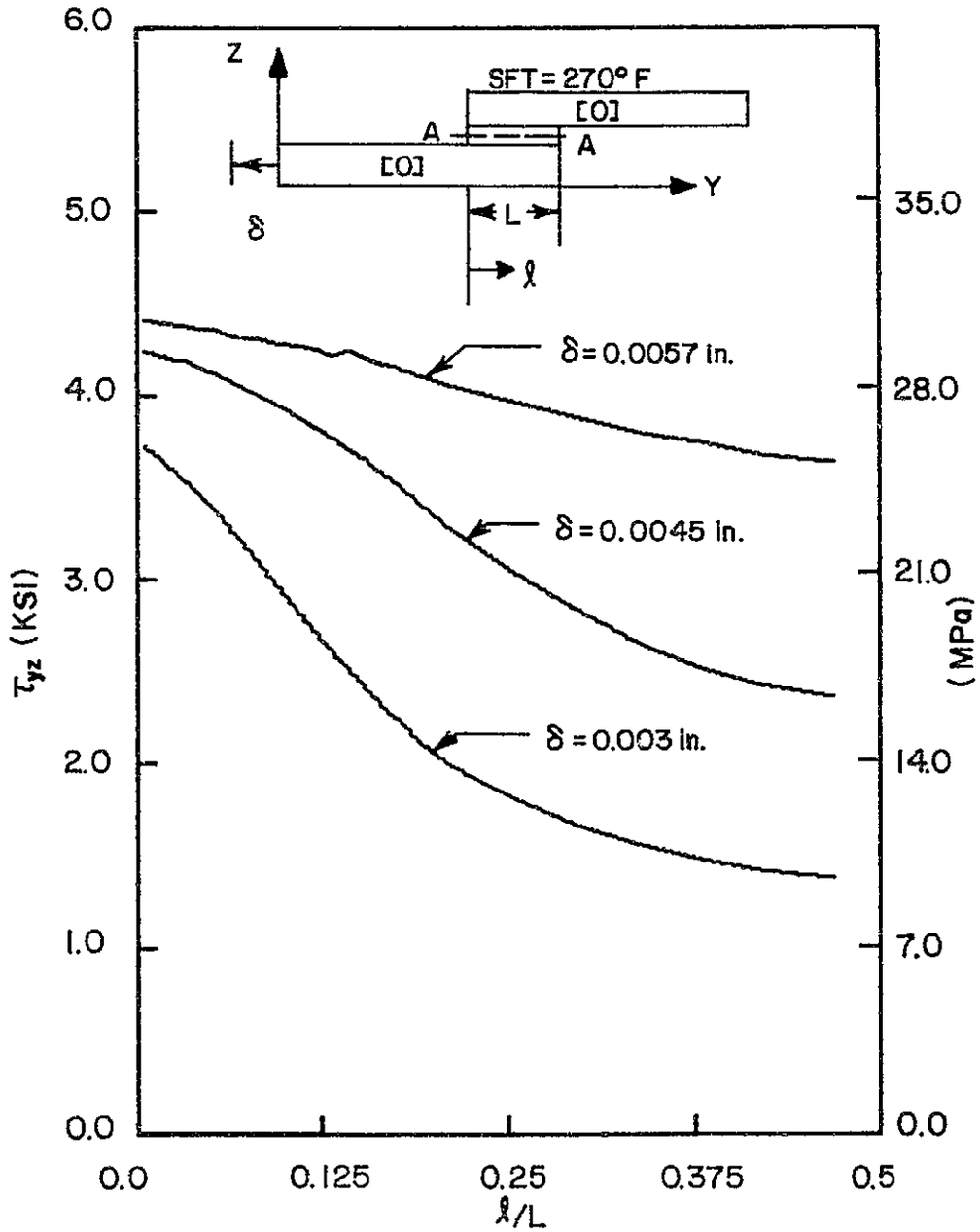

Figure 41. Nonlinear Mechanical and Curing Adhesive σ_{yz} Stresses of a Single Lap Joint with [0] Gr/Pi Adherends and Metlbond 1113 Adhesive

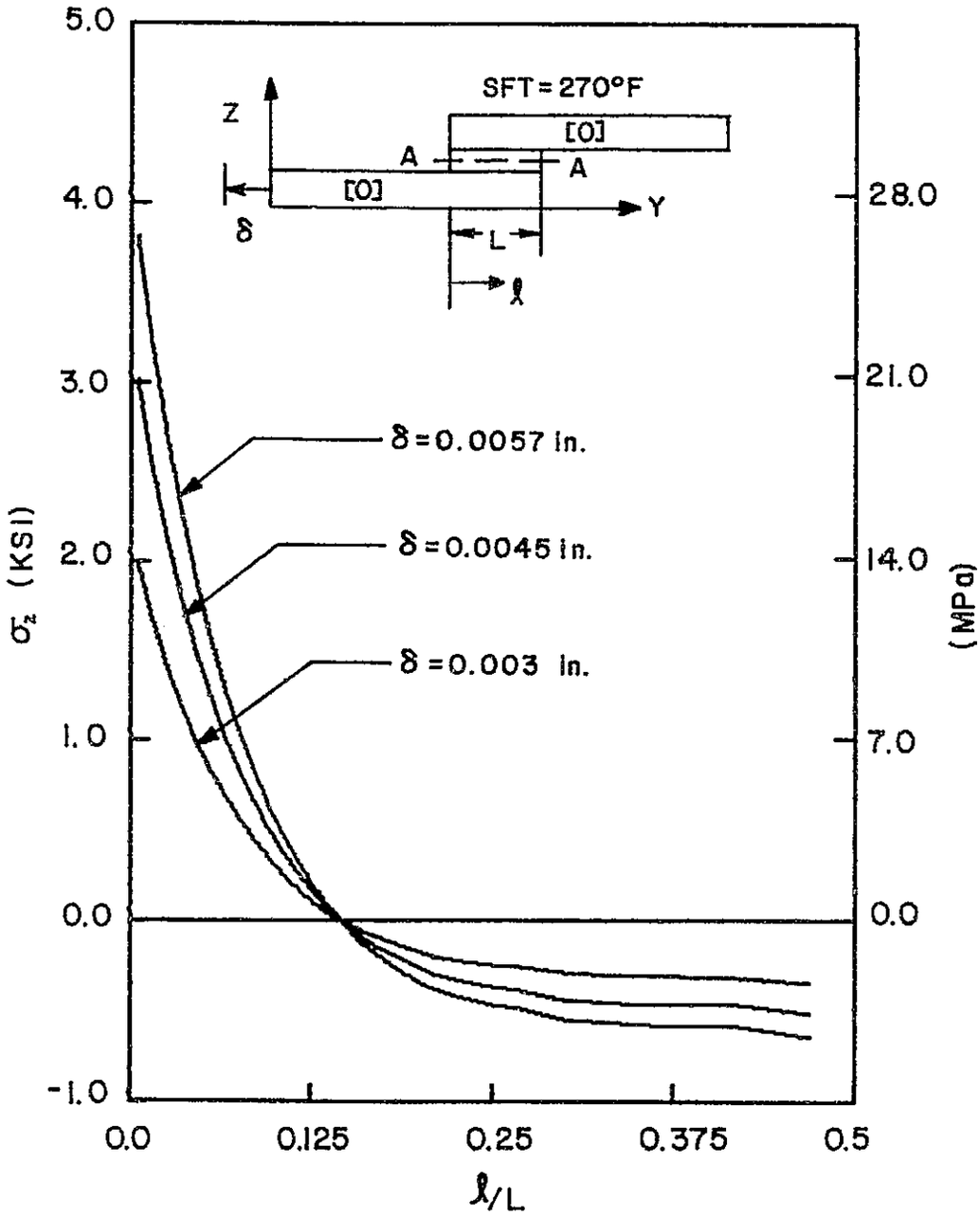

Figure 42. Nonlinear Mechanical and Curing Adhesive σ_z Stresses of a Single Lap Joint with [0] Gr/Pi Adherends and Metlbond 1113 Adhesive

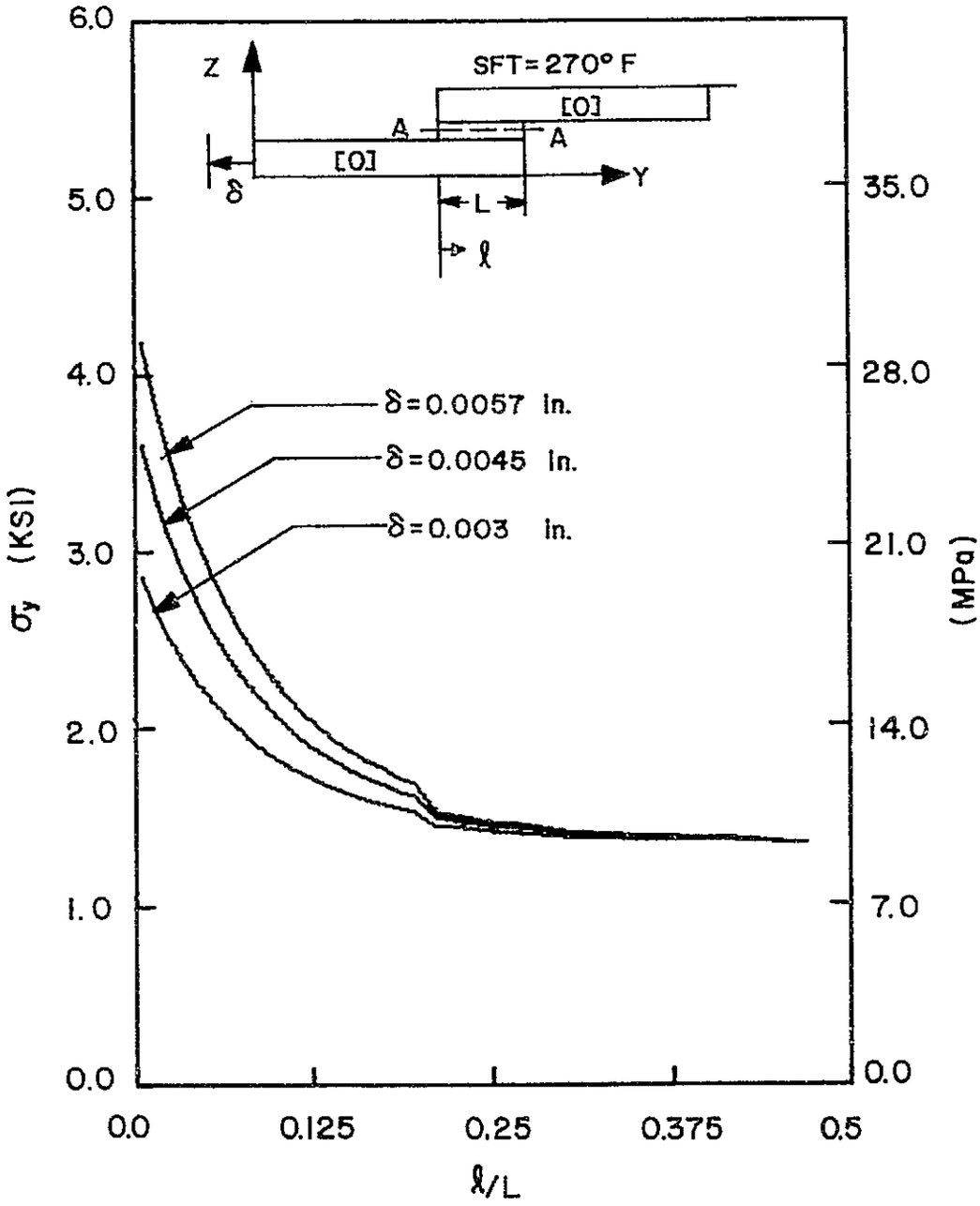

Figure 43. Nonlinear Mechanical and Curing Adhesive σ_y Stresses of a Single Lap Joint with [0] Gr/Pi Adherends and Metlbond 1113 Adhesive

shearing stresses for this joint (Fig. 41) exhibit nonlinear effects. Comparisons between elastic and nonlinear mechanically induced stresses are presented in Table 7. These comparisons show that the σ_y^M and σ_z^M stress components behave linearly throughout the range of mechanical loading applied. The shearing stress is decidedly nonlinear though, with the elastic solution predicting stresses 82 percent higher than the nonlinear results indicate.

5.6.1.4 $[\pm 45]_s$ Graphite-Polyimide Adherends and Metlbond 1113 Adhesive

The nonlinear curing stresses for this joint are not plotted for the same reasons as the previous joint. The numerical values of the two significant curing stresses are presented in Table 8 which presents a comparison of elastic and nonlinear results for this joint. This comparison shows a six percent increase in the curing stresses for the nonlinear analysis.

Combined mechanical and curing adhesive stresses for this joint are shown in Fig's 44, 45, 46 and 47. Again, it is seen that nonlinear behavior is present in only the shear stresses. It is unfortunate that the maximum loading for this joint did not produce a peak shear stress corresponding to the ultimate strength. This would have produced much more pronounced nonlinear effects. Comparisons between elastic and nonlinear mechanical adhesive stresses are also presented in Table 8. It is seen that at the maximum load level attained, the nonlinear results predict a peak shear stress 28 percent below the elastic results. The elastic mechanical results are determined as the first

TABLE 8

Comparison of Elastic and Nonlinear Adhesive Stresses for a Single Lap Joint with $[\pm 45]_s$ Gr/Pi Adherends and Metlbond 1113 Adhesive

Type of Analysis	Curing Stresses SFT = 270°F (ksi)		Peak Mechanical Stresses (ksi)			
	σ_x	σ_y	σ_x	σ_y	σ_z	τ_{yz}
Elastic	1.5	1.5	1.3	2.6	2.9	5.1
Nonlinear	1.6	1.6	1.3	2.6	2.9	4.0
Difference	6%	6%	0%	0%	0%	28%

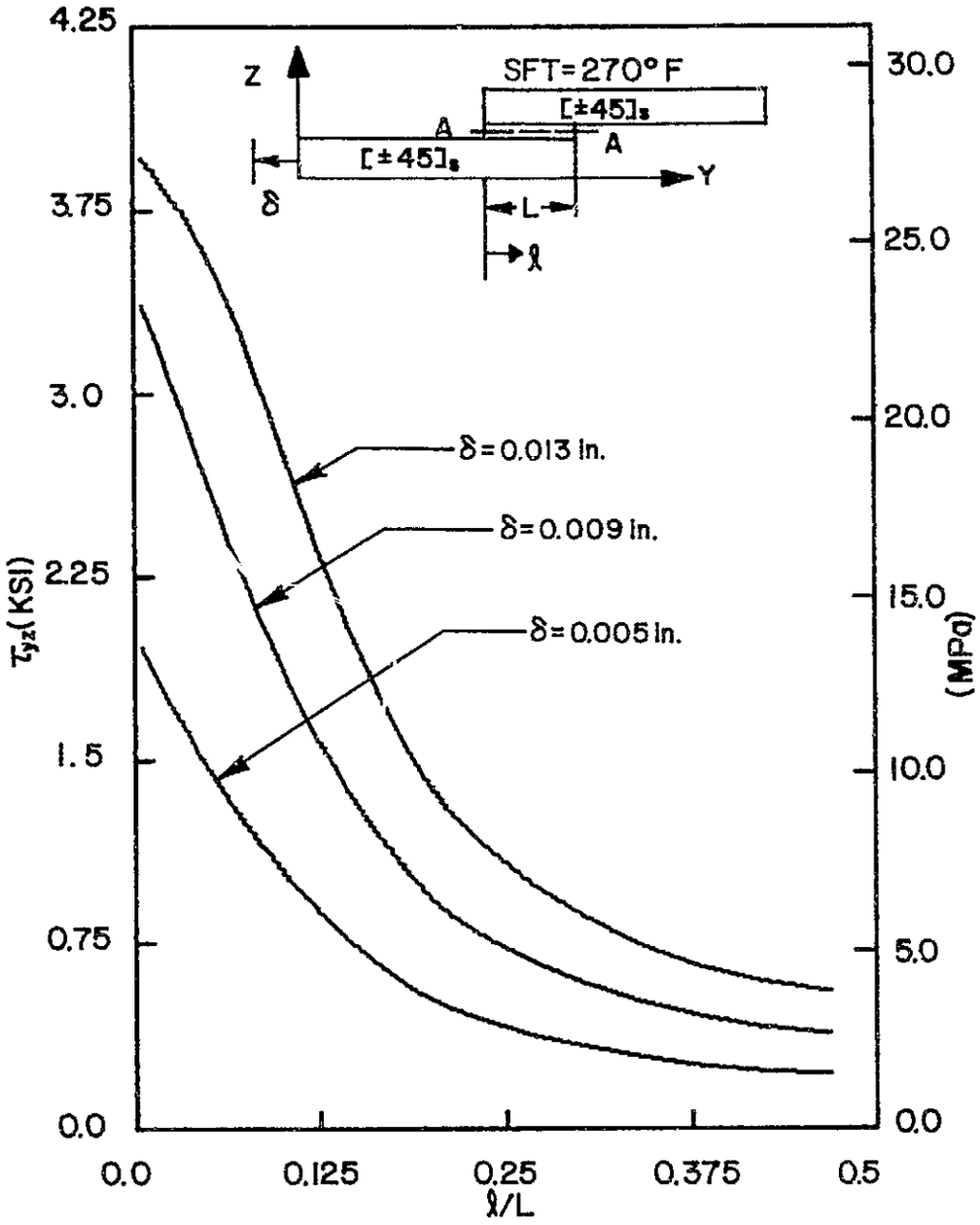

Figure 44. Nonlinear Mechanical and Curing Adhesive τ_{yz} Stresses of a Single Lap Joint with $[\pm 45]_s$ Gr/Pi Adherends and Metlbond 1113 Adhesive

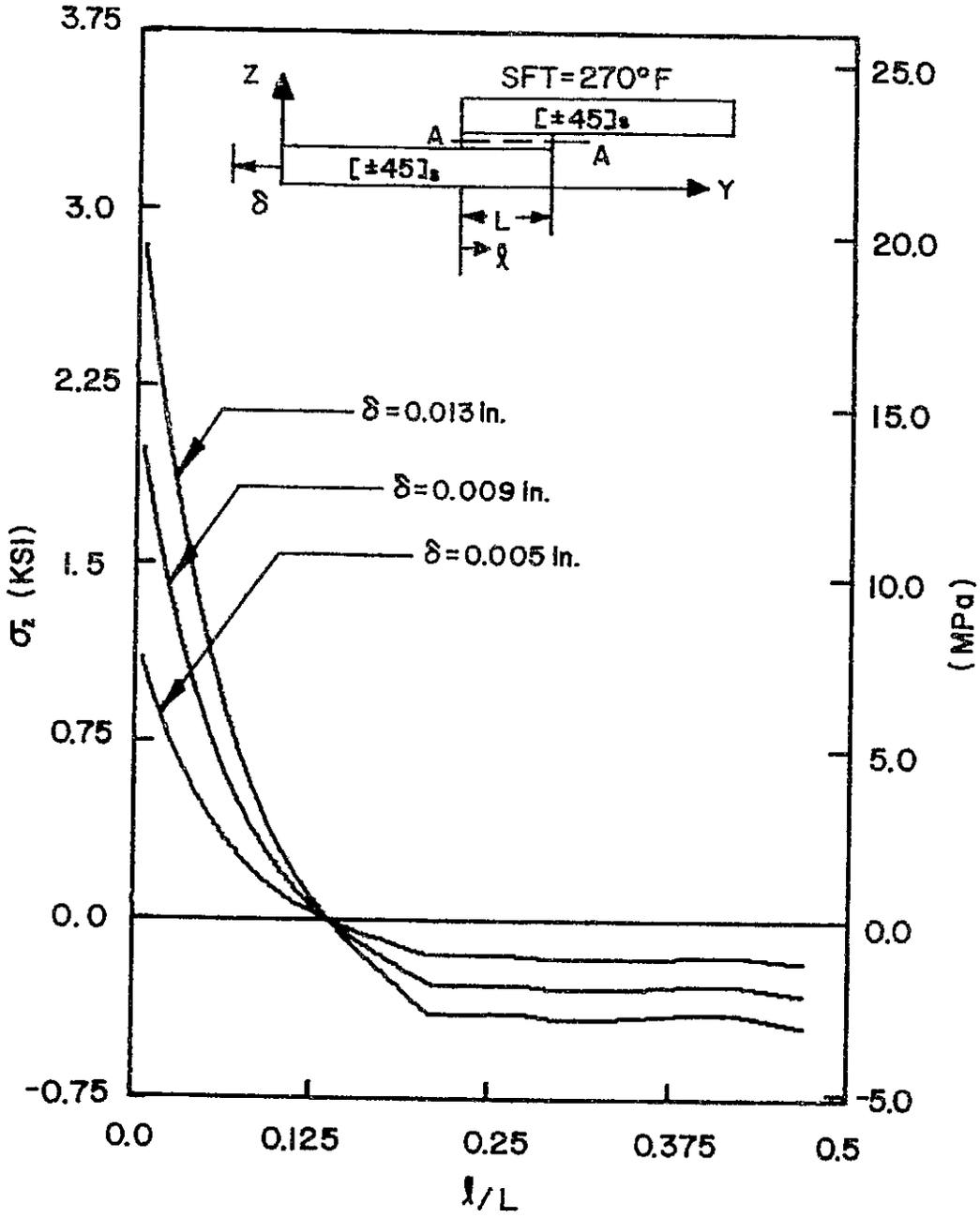

Figure 45. Nonlinear Mechanical and Curing Adhesive σ_z Stresses of a Single Lap Joint with $[\pm 45]_s$ Gr/Pi Adherends and Metlbond 1113 Adhesive

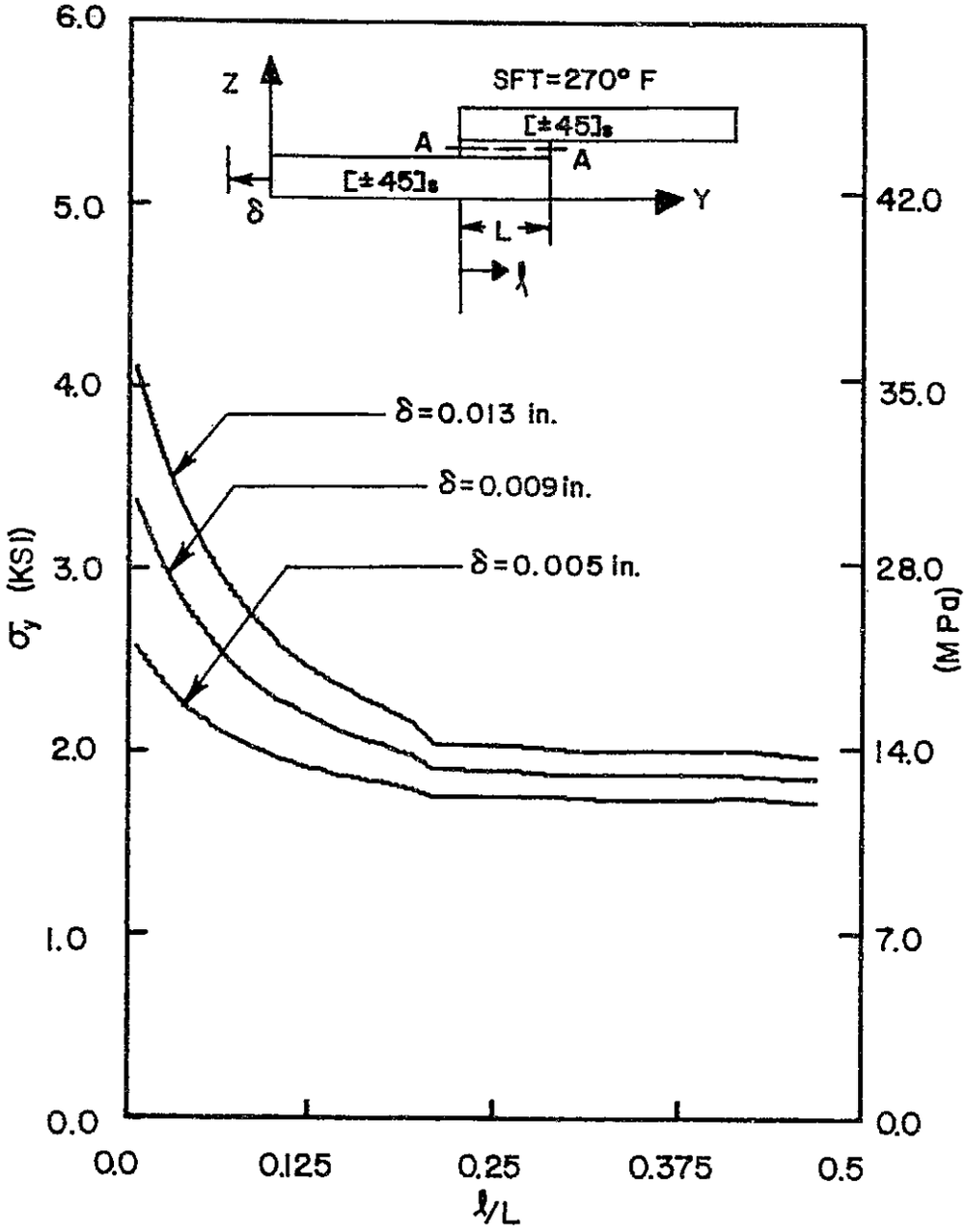

Figure 46. Nonlinear Mechanical and Curing Adhesive σ_y Stresses of a Single Lap Joint with $[\pm 45]_s$ Gr/Pi Adherends and Metlbond 1113 Adhesive

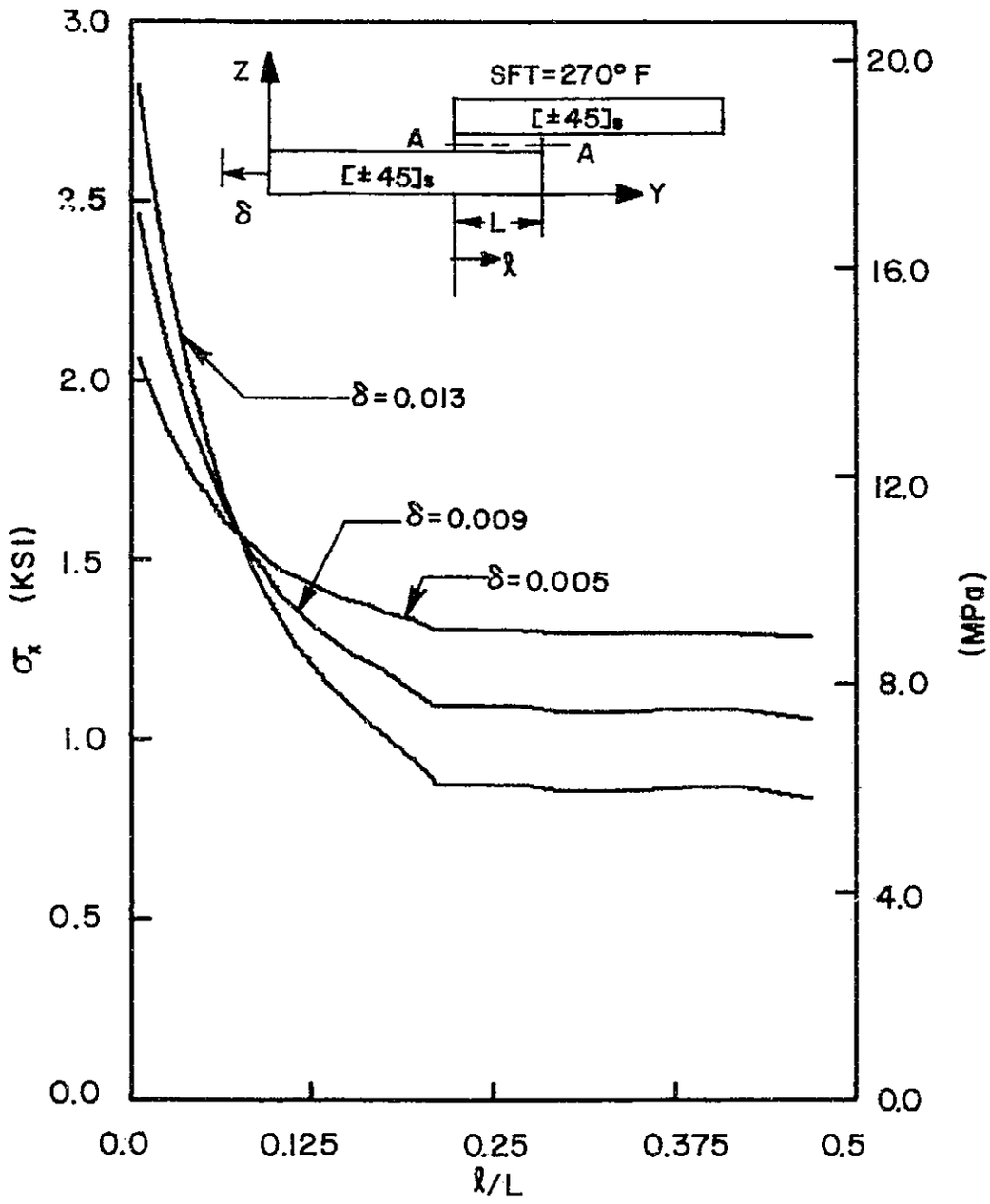

Figure 47. Nonlinear Mechanical and Curing Adhesive σ_x Stresses of a Single Lap Joint with $[\pm 45]_s$ Gr/Pi Adherends and Metlbond 1113 Adhesive

increment of the nonlinear results scaled to the maximum displacement load. It is somewhat surprising that the nonlinear analysis does not predict lower stress components σ_x^M, σ_y^M, and σ_z^M for this and the previous joint. It can be explained however by considering the final magnitudes of these stress components. All are relatively low on the extensional stress-strain response of the adhesive. At these stress levels the curve is very linear resulting in very linear stress predictions.

5.6.2 Double Lap Joints

5.6.2.1 Titanium Adherends Metlbond 1113 Adhesive

Comparisons of elastic and nonlinear curing stresses for this joint are shown in Table 9. Once more, the two nonzero components of curing stress (σ_x^T and σ_y^T) were uniform and they are not plotted. Here again, an increase in the nonlinear results over the elastic case is seen.

Combined stresses for this joint are presented in Fig's. 48, 49, 50 and 51. In these figures only the shear curves show pronounced nonlinearities, as before, but Table 9 indicates that the other stresses (σ_x, σ_y, and σ_z) are slightly reduced for the nonlinear analysis. The reason this joint should exhibit nonlinear behavior where the previous joints did not is not immediately discernable. The most obvious difference between this joint and the previous ones is the restriction placed upon the w displacements at the midplane of the inner adherend by the symmetry of the double lap.

5.6.2.2 [0] and [90] Graphite-Polyimide Adherends and Metlbond 1113 Adhesive

Curing stresses for this joint are presented in Fig. 52. These

TABLE 9

Comparison of Elastic and Nonlinear Adhesive Stresses for a Double Lap Joint with Ti Adherends and Metlbond 1113 Adhesive

Type of Analysis	Curing Stresses SFT = 270°F (ksi)		Peak Mechanical Stresses (ksi)			
	σ_x	σ_y	σ_x	σ_y	σ_z	τ_{yz}
Elastic	1.20	1.20	1.63	1.97	2.92	6.18
Nonlinear	1.25	1.25	1.58	1.91	2.8	4.4
Difference	4%	4%	3%	3%	4%	40%

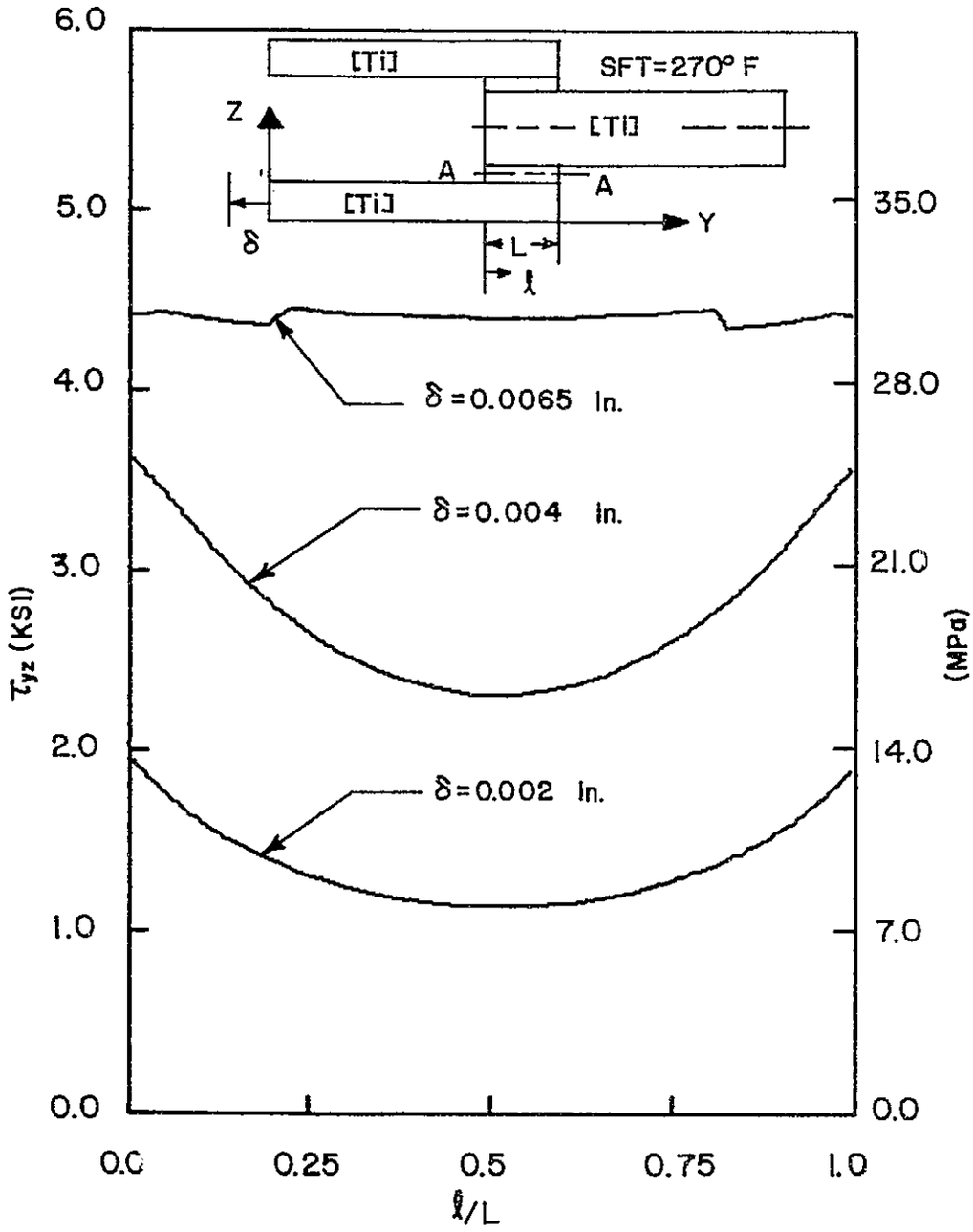

Figure 48. Nonlinear Mechanical and Curing Adhesive τ_{yz} Stresses of a Double Lap Joint with Titanium Adherends and Metlbond 1113 Adhesive

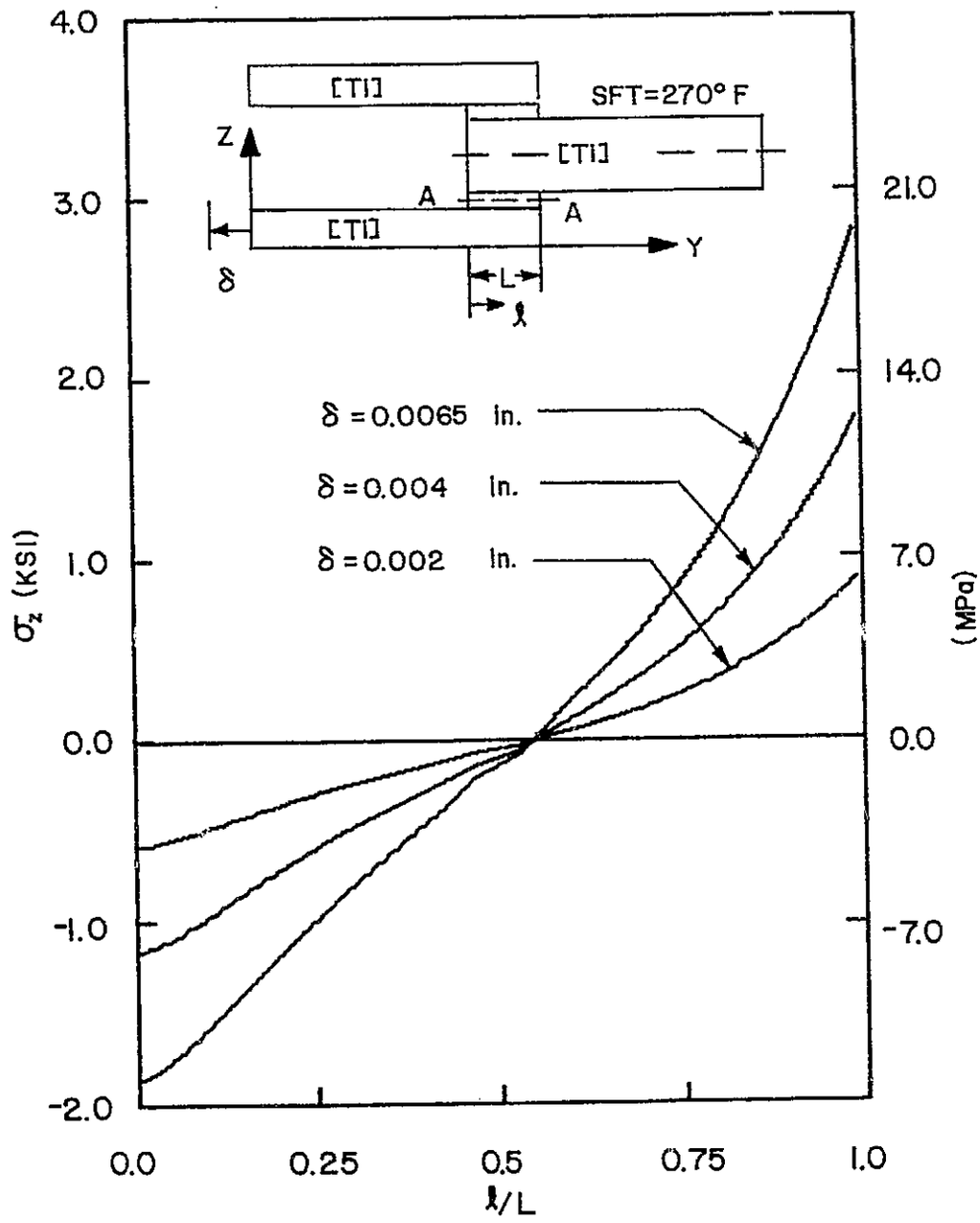

Figure 49. Nonlinear Mechanical and Curing Adhesive σ_z Stresses of a Double Lap Joint with Titanium Adherends and Metlbond 1113 Adhesive

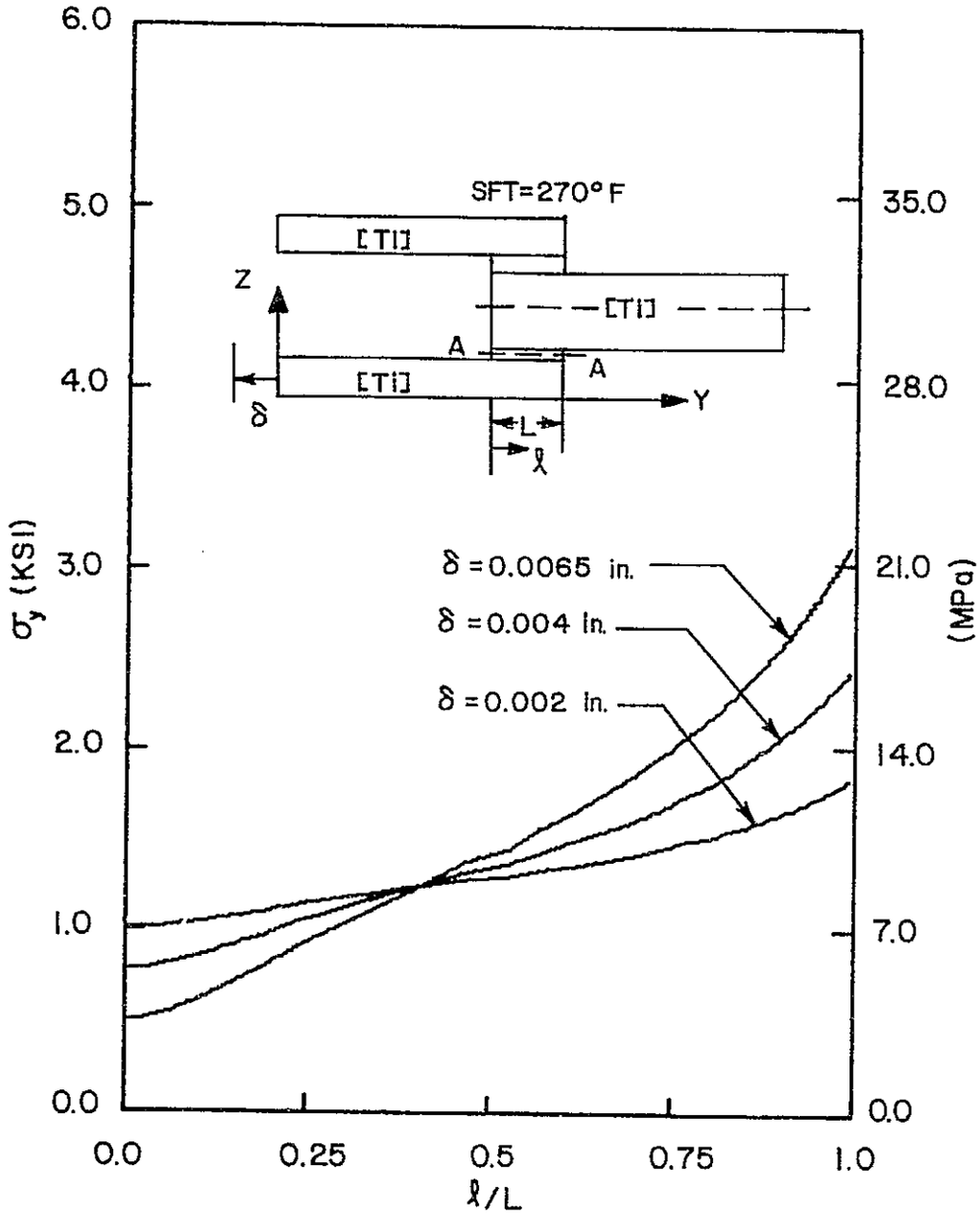

Figure 50. Nonlinear Mechanical and Curing Adhesive σ_y Stresses of a Double Lap Joint with Titanium Adherends and Metlbond 1113 Adhesive

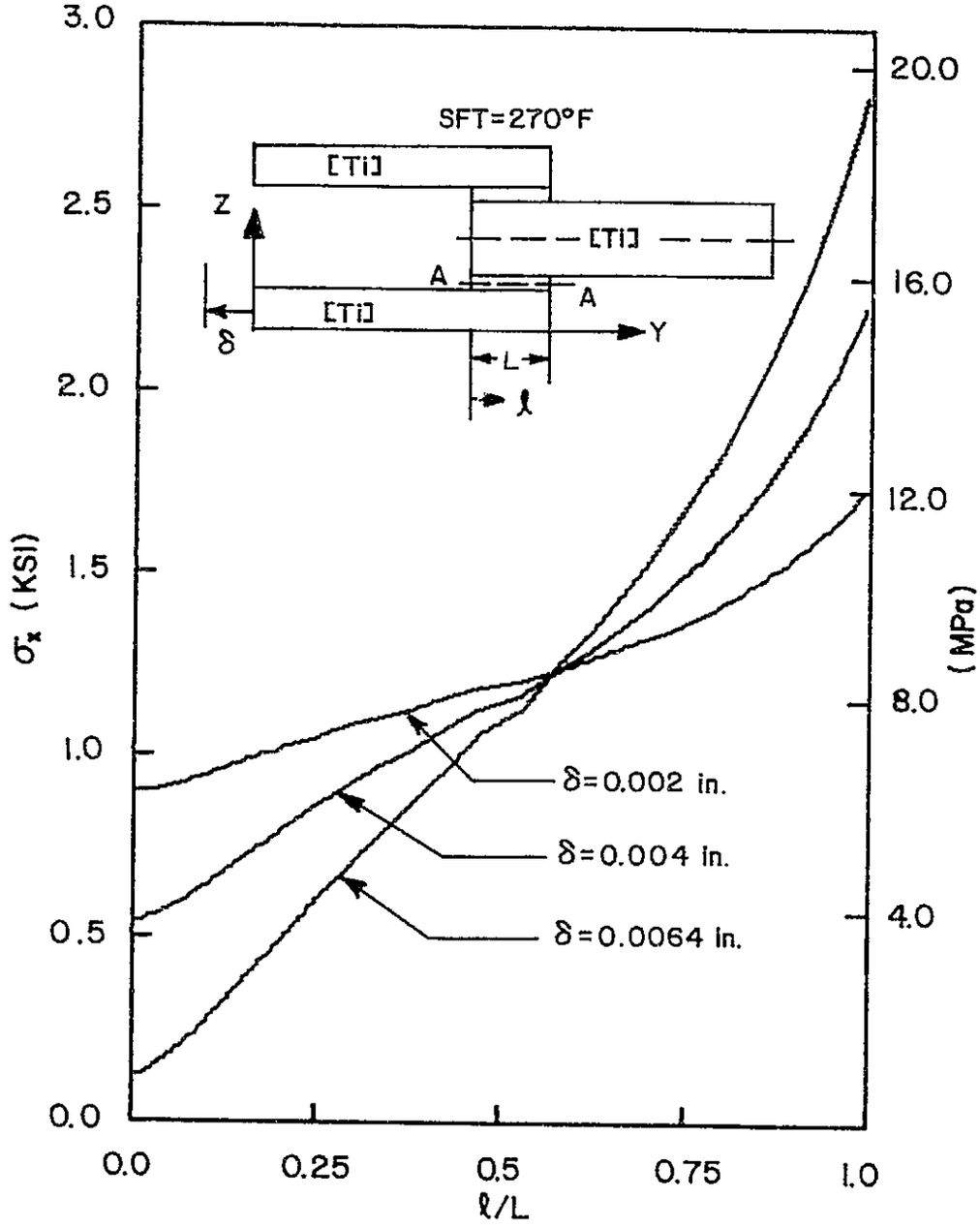

Figure 51. Nonlinear Mechanical and Curing Adhesive σ_x Stresses of a Double Lap Joint with Titanium Adherends and Metlbond 1113 Adhesive

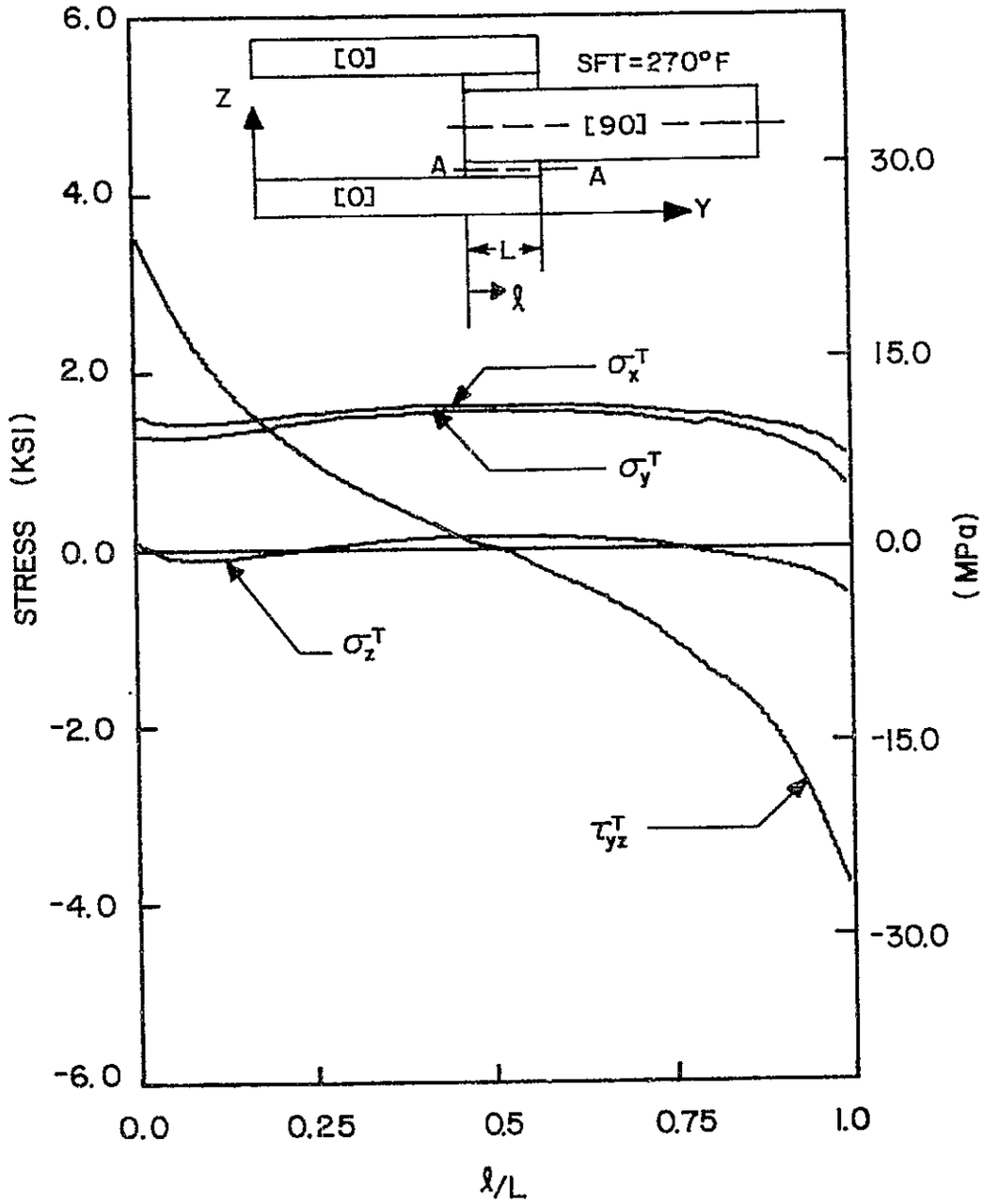

Figure 52. Nonlinear uring Adhesive Stresses of a Double Lap Joint with [0] and [90] Gr/Pi Adherends and Metlbond 1113 Adhesive

distributions appear very similar to the elastic curing stresses for the same joint (Fig. 21). Comparisons between these two analyses are shown in Table 10. It can be seen that the nonlinear curing stresses differ from the elastic results between 2 percent and 6 percent. The 23 percent difference shown for σ_z near $\ell/L = 0$ is probably exagerated by the low magnitudes of these stresses. It can be seen in Table 10 that the nonlinear effects cause an increase in the σ_x^T and σ_y^T curing stresses as shown in previous results. However, the σ_z^T and τ_{yz}^T stresses are decreased by the nonlinear behavior. These two stresses are related through equilibrium (section 5.5.1.1) and it is therefore appropriate that both change in the same fashion. This decrease is due to the high values of shear stress produced by curing and the low adhesive modulus at these values.

Fig's. 53, 54, 55, and 56 present combined mechanical and curing adhesive stresses for this joint. Comparing Fig's. 52 and 53 it can be seen that the curing stresses are very beneficial to the performance of this joint. In Fig. 53, as the displacement load level increases, the shear stresses near $\ell/L = 1$ are seen to increase more rapidly than at $\ell/L = 0$. Thus, the shear stresses near $\ell/L = 1$ would be much larger than the shear stress near $\ell/L = 0$ for mechanical loading only. However, the curing shear stresses near $\ell/L = 1$ have the opposite sign of the mechanical shear stresses in this region and are of relatively large magnitude. Therefore, a large portion of the mechanically induced shear stresses are negated by the curing shear stress and thus the joint is capable of carrying an increased load.

TABLE 10

Comparison of Elastic and Nonlinear Adhesive Curing Stresses for a Double Lap Joint with [0] and [90] Gr/Pi Adherends and Metlbond 1113 Adhesive

Type of Analysis	Curing Stresses SFT = 270° (ksi)							
	σ_x		σ_y		σ_z		τ_{yz}	
	$\ell/L=0$	$\ell/L=1$	$\ell/L=0$	$\ell/L=1$	$\ell/L=0$	$\ell/L=1$	$\ell/L=0$	$\ell/L=1$
Elastic	1.47	1.03	1.26	0.67	0.092	-0.53	3.6	-4.0
Nonlinear	1.53	1.08	1.32	0.71	0.12	-0.51	3.53	-3.8
Difference	4%	5%	5%	6%	23%	4%	2%	5%

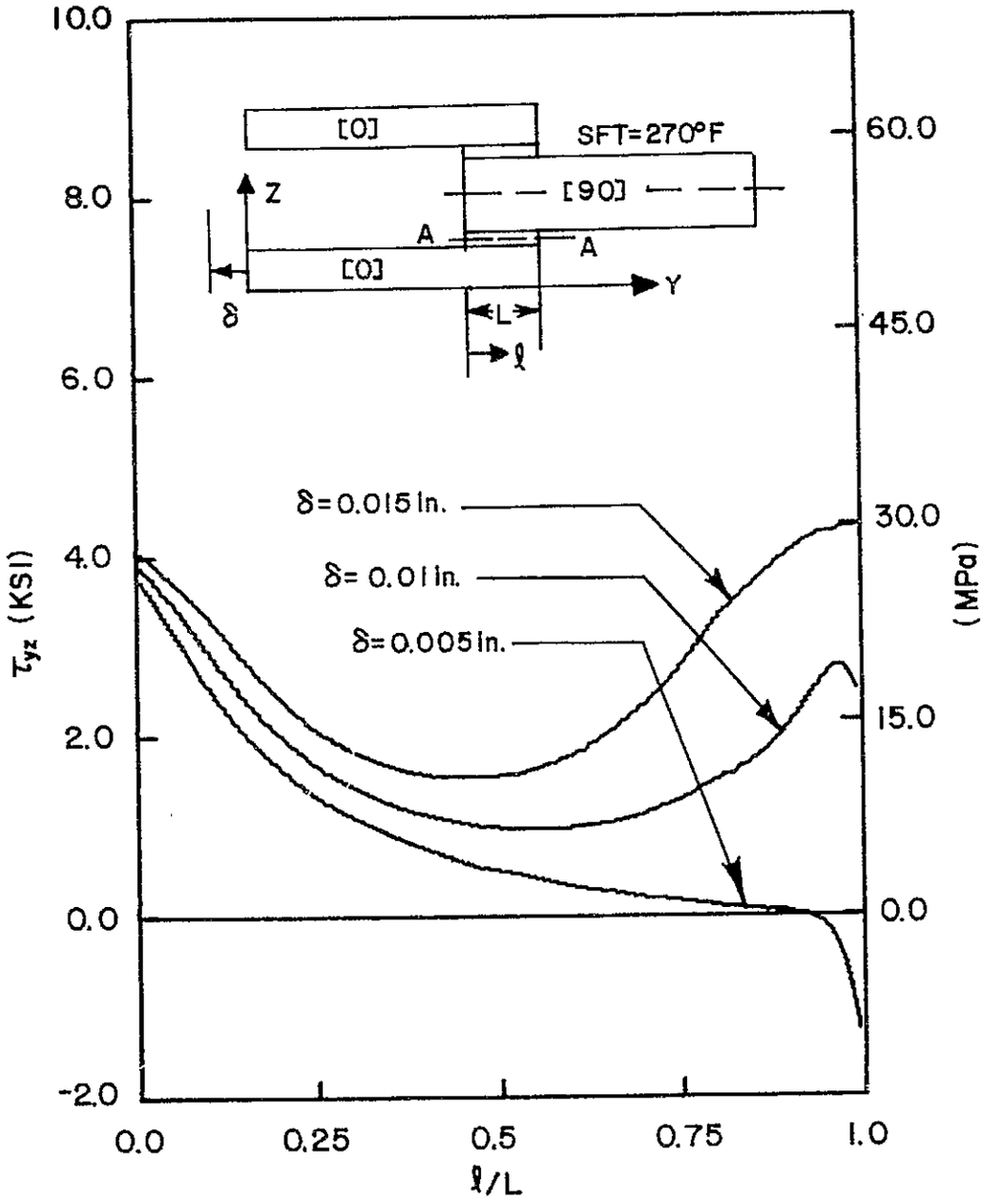

Figure 53. Nonlinear Mechanical and Curing Adhesive τ_{yz} Stresses of a Double Laop Joint with [0] 1113 Adhesive

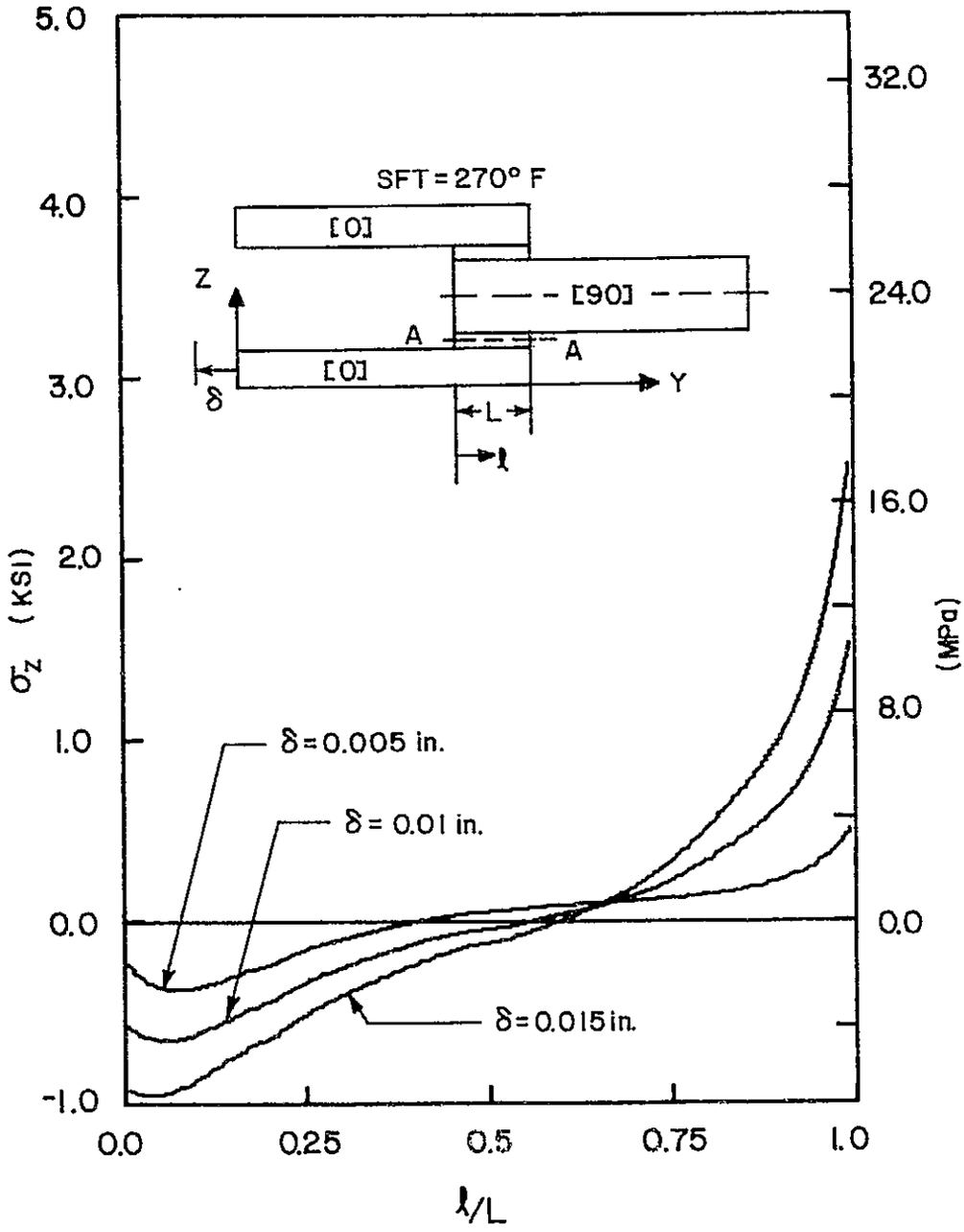

Figure 54. Nonlinear Mechanical and Curing Adhesive σ_z Stresses of a Double Laop Joint with [0] and [90] Gr/Pi Adherends and Metlbond 1113 Adhesive

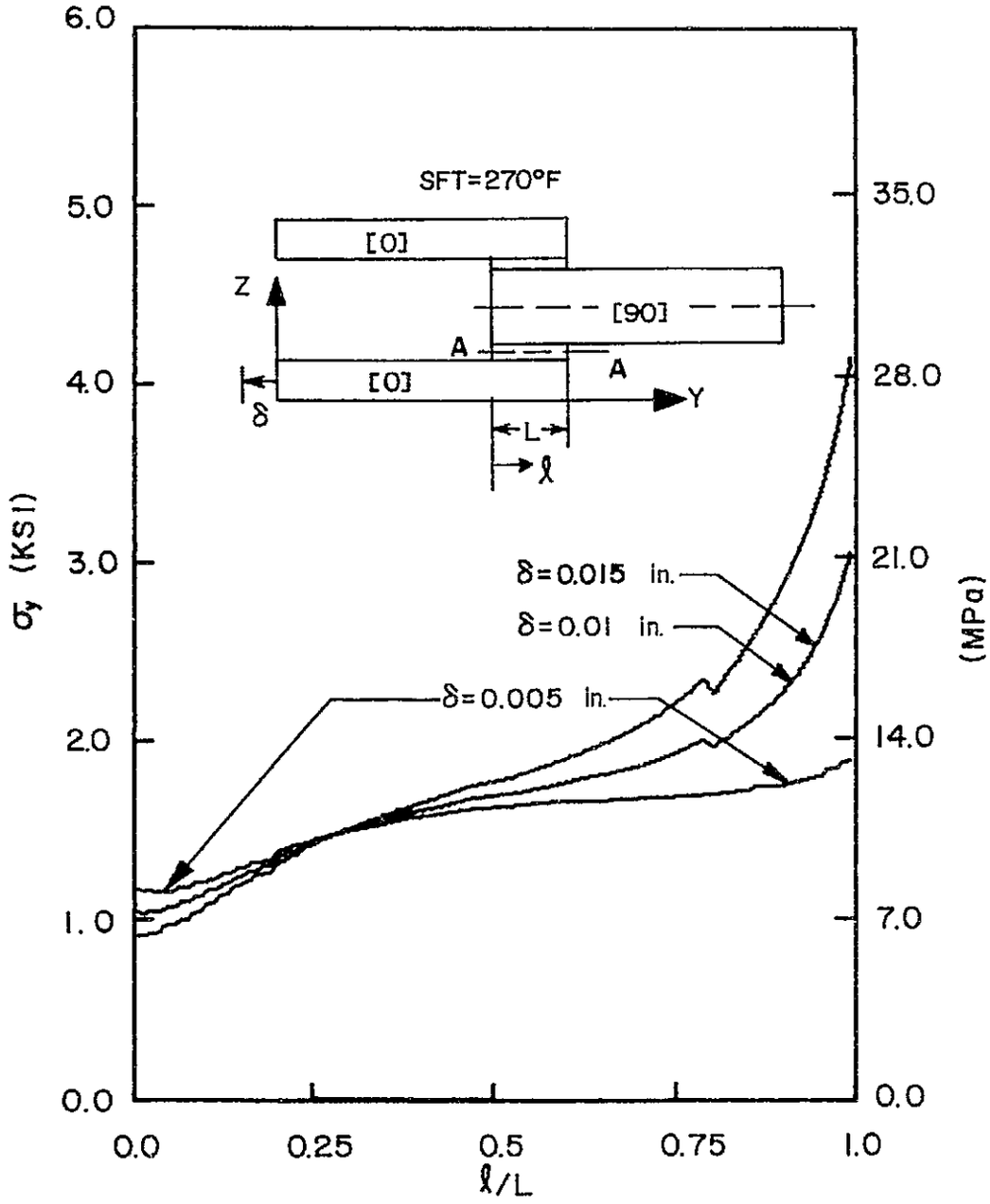

Figure 55. Nonlinear Mechanical and Curing Adhesive σ_y Stresses of a Double Laop Joint with [0] and [90] Gr/Pi Adherends and Metlbond 1113 Adhesive

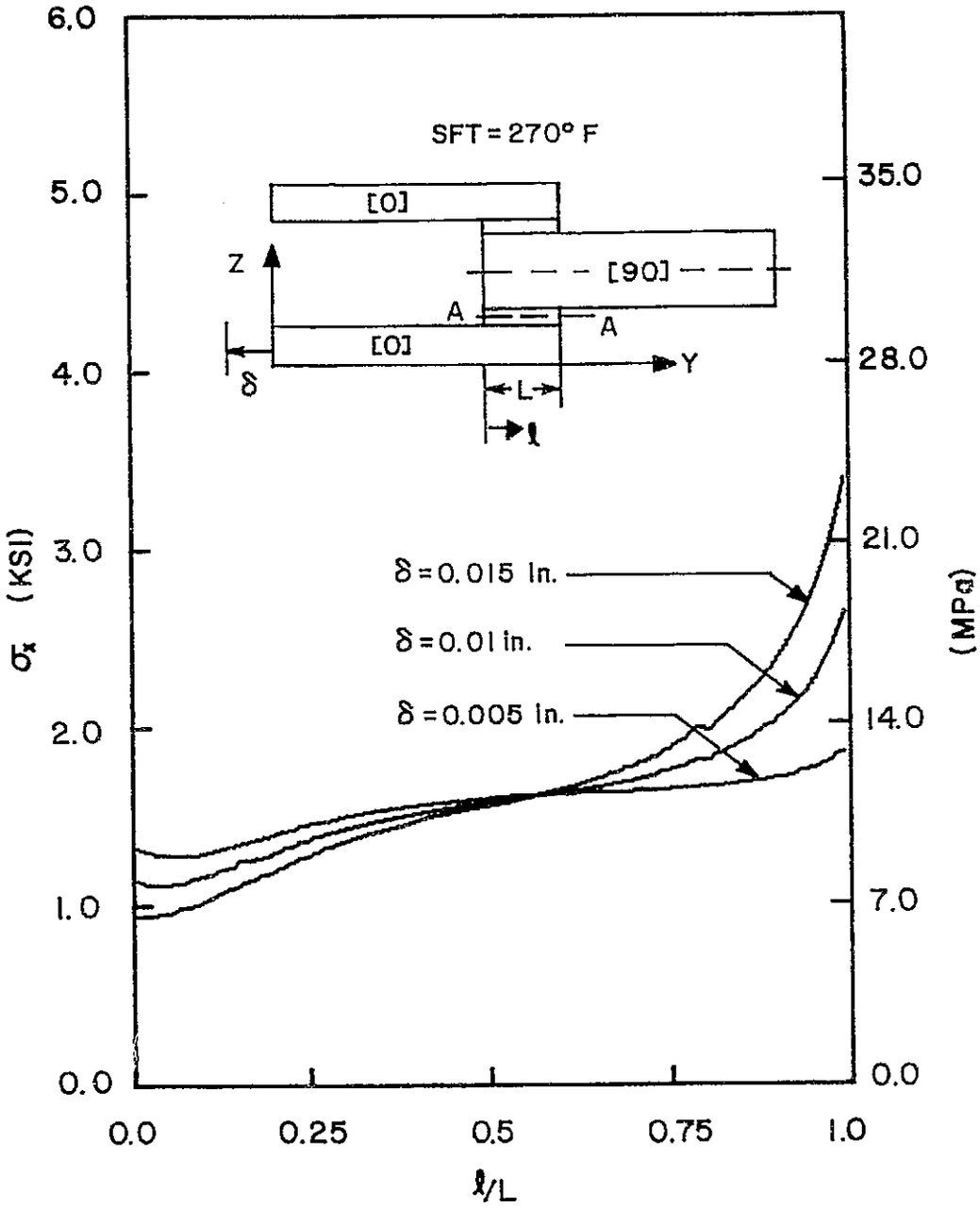

Figure 56. Nonlinear Mechanical and Curing Adhesive σ_x Stresses of a Double Laop Joint with [0] and [90] Gr/Pi Adherends and Metlbond 1113 Adhesive

Chapter 6

SUMMARY AND CONCLUSIONS

The present analysis has been concerned with the nonlinear analysis of bonded joints. Upon reviewing the results presented, the following conclusions can be made with respect to the joint materials and geometries studied.

1. The effects of adhesive nonlinearities greatly influence the shear stress predictions in the adhesive layer of bonded joints.
2. The effects of adhesive nonlinearities have little influence upon the normal stress components in the adhesive layer of bonded joints.
3. Adherend nonlinear behavior has little effect upon the adhesive stresses in bonded joints.
4. Residual curing stresses are significant in adhesive bonded joints. These curing stresses are detrimental in joints with similar adherends, but may be beneficial in joints with differing adherends.
5. Residual curing stresses are significant in bonded joints with differing adherends and no adhesive.
6. Residual curing stresses are not significantly influenced by material nonlinearities or temperature dependent properties.
7. Adherend stiffness has profound effects upon mechanically induced stresses in bonded joints. Stresses

produced in the adhesive layer of adhesive bonded joints and along the adherend-adherend interface in bonded joints without adhesives are higher for stiffer adherends. In adhesive bonded joints with differing adherends, maximum adhesive stresses correspond to the more flexible adherend.

8. Adhesive and interfacial stresses are non-uniform with maximum values produced near the edges of the overlap region.
9. Adhesive bonded double lap joints are more efficient single lap joints due to a more uniform stress distribution in double lap joints.
10. A quasi 3-dimensional analysis predicts a more flexible joint response than a 2-dimensional formulation. A larger displacement load is required in a quasi 3-dimensional analysis to predict adhesive stresses comparable to those of a 2-dimensional analysis.
11. A quasi 3-dimensional analysis demonstrates the effects of adherend transverse stiffness and thermal coefficient of expansion upon the residual curing stresses.
12. Adhesive stresses are not significantly influenced by different symmetric loadings. Force loadings produce results similar to displacement loadings.

13. The method of solution presented satisfies static equilibrium very closely.

This analysis has shown that future areas of study might include the following:

1. Analysis capability for out of plane bending and warpage.
2. Better representation of stress-strain response as a function of temperature, and moisture.
3. Nonlinear analysis of the effects of moisture in bonded joints.
4. Inclusion of a capability to allow Poisson Ratios to vary as a function of strain, temperature, and moisture.
5. Allowing failure strengths to vary as functions of temperature and moisture.
6. Consistent modeling of the interactions of temperature and moisture.

BIBLIOGRAPHY

1. Renieri, G. D., Herakovich, C. T., "Nonlinear Analysis of Laminated Fibrous Composites," VPI&SU Report VPI-E-76-10, June, 1976.

2. Goland, M., Reissner, E., "The Stresses in Cemented Joints," J. Applied Mechanics, Vol. 1, No. 1, pp. 17-27, March, 1944.

3. Erodogan, F., Ratwani, M., "Stress Distribution in Bonded Joints," J. Composite Materials, Vol. 5, pp. 378-393, July, 1971.

4. Barker, R. M., Hatt, F., "Analysis of Bonded Joints in Vehicular Structures," VPI-E-73-16, 1973.

5. Sainsburg-Carter, J. B., "Automated Design of Bonded Joints," ASME paper no. 72-WA/DE-13, July, 1972.

6. Wah, T., "Stress Distribution in a Bonded Anisotropic Lap Joint," J. Engineering Materials and Technology, Vol. 95, pp. 174-181, July, 1973.

7. Hart-Smith, L. J., "Analysis and Design of Advanced Composite Bonded Joints," NASA CR 2218, January, 1973.

8. Sharpe, W. N., Jr., Muha, T. J., "The Comparison of Experimental and Theoretical Shear Stress in the Adhesive Layer of a Lap Joint Model," Proceedings of the Army Symposium on Solid Mechanics, 1974: The Role of Mechanics in Design of Structural Joints," AMMRC MS 74-8, September, 1974.

9. Renton, J. W., Vinson, J. R., "On the Behavior of Bonded Joints in Composite Material Structures," Engineering Fracture Mechanics, Vol. 7, pp. 41-60, 1975.

10. Renton, W. J., Vinson, J. R., "The Efficient Design of Adhesive Bonded Joints," AIAA, ASME, SAE, 16th Structures, Structural Dynamics, and Materials Conference, AIAA paper no. 75-798, May, 1975.

11. Grimes, G. C., Greimann, L. F., Wah, T., Commerford, G. E., Blackstone, W. R., Wolfe, G. K., "The Development of Nonlinear Analysis Methods for Bonded Joints in Advanced Filamentary Composite Structures," AFFDL-TR-72-97, September, 1972.

12. DasGutpa, S., Sharma, S. P., "Stresses in an Adhesive Lap Joint," ASME paper no. 75-WA/DE-18, July, 1975.

13. Renton, W. J., "The Symmetric Lap Shear Test - What Good is it?", Esperimental Mechanics, pp. 409-415, November, 1975.

14. Wetherhold, R., Vinson, J. R., "An Analytical Model for Bonded Joint Analysis in Composite Structures Including Hygrothermal Effects," Fourth National Conference on Composite Materials: Testing and Design, May, 1976.

15. Birchfield, E. B., Cole, R. T., Impellizzeri, L. F., "Reliability of Step-Lap Bonded Joints," AFFDL-TR-72-26, April, 1975.

16. Wilson, E. L., Bathe, K., Doherty, W. P., "Direct Solution of Large Systems of Linear Equations," Computers and Structures," Vol. 4, pp. 363-372, 1974.

17. Ramberg, W., Osgood, W. B., "Description of Stress-Strain Curves by Three Parameters," NASA TN 902, 1943.

18. Bergner, H. W., Davis, J. G., Herakovich, C. T., "Analysis of Shear Test Methods for Composite Laminates," VPI-E-77-14, April, 1977.

19. Daniel, I. M., Liber, T., "Lamination Residual Stresses in Fiber Composites," NASA CR-134826, May, 1975.

20. Sancaktar, E., "Shear Behavior of a Viscoelastic Structural Adhesive," present work on Ph.D. dissertation.

21. Renieri, M. P., Herakovich, C. T., Brinson, H. F., "Rate and Time Dependent Behavior of Structural Adhesives," VPI-E-76-7, April, 1976.

22. Sessler, J. G., Weiss, V., "Aerospace Structural Metals Handbook," AFML-TR-68-115, January, 1968.

23. Gibbs, H. H., "Status Report: NR-150 Polyimide Binders and Adhesives," Proceedings SAMPE Conference, Spring 1976.

24. Petit, P. H. Waddoups, M. E., "A Method for Predicting the Nonlinear Behavior of Laminated Composites," J. Composite Materials, Vol. 3, 1969, 2-19.

25. Kaminski, B. E., Lemon, G. H., McKague, E. L., "Development of Engineering Data for Advanced Composite Materials," AFML-TR-70-108, 1972.

26. Viswanithan, C. N., Davis, J. G., Herakovich, C. T., "Tensile and Compressive Behavior of Borsic/Aluminum Composite Laminates," VPI-E-75-12, June, 1975.

27. Marceau, A., Scardino, W., "Durability of Adhesive Bonded Joints," AFML-TR-75-3, February, 1975.

28. Sturgeon, J. B., "Tensile Tests on Lap Joints in Carbon Fibre Reinforced Plastics," RAE-TR-70159, August, 1970.

29. Pipes, R. B., Vinson, J. R., Chou, T., "On the Hygrothermal Response of Laminated Composite Systems," J. Composite Materials, Vol. 10, pp. 129-148, April, 1976.

30. Verette, R. M., "Temperature/Humidity Effects on the Strength of Graphite/Epoxy Laminates," AIAA Paper No. 75-1011, August, 1975.

31. Whitney, J. B., Ashton, J. E., "Effect of Environment on the Elastic Response of Layered Composite Plates," AIAA Journal, Vol. 9, No. 9, September, 1971.

32. Grimes, G. C., Greimann, L. F., "Analysis of Discontinuities, Edge Effects, and Joints," Composite Materials, Vol. 8, Part II, pp. 135-230, 1975.

APPENDIX A

ELEMENTAL STIFFNESS MATRIX

Equations (A.1) represent the equilibrium equations for applied strain loading. Equ's (A.2) represent the equilibrium equations in average force loadings. In these equations, [K] is the symmetric elemental stiffness matrix, $\varepsilon_x\{S\}$ and $\{T\}$ are force vectors corresponding to the applied strain and temperature change respectively, $\{F\}$ is the vector of applied forces, and $\{x\}$ is the vector of unknown nodal displacements.

$$\underset{(9x9)}{[K]^{(\ell)}}\underset{(9x1)}{\{x\}^{(\ell)}} + \underset{(9x1)}{\varepsilon_x\{S\}^{(\ell)}} = \underset{(9x1)}{\{F\}^{(\ell)}} \tag{A.1}$$

$$\underset{(10x10)}{[K]^{(\ell)}}\underset{(10x1)}{\{x\}^{(\ell)}} - \underset{(10x1)}{\{T\}^{(\ell)}} = \underset{(10x1)}{\{F\}^{(\ell)}} \tag{A.2}$$

Defining the following terms

$$a = (Z_2-Z_3)/2$$

$$b = (Y_3-Y_2)/2$$

$$c = (Z_3-Z_1)/2$$

$$d = (Y_1-Y_3)/2$$

$$e = (Z_1-Z_2)/2$$

$$g = (Y_2-Y_1)/2$$

A^{ℓ} = the area of element (ℓ)

F^{*} = average normal force

where Y_1 through Y_3 and Z_1 through Z_3 are the coordinates of the nodal points of element ℓ in the Y-Z plane, the element of the matricies of Equ. (A.1) can be defined as follows.

$$K_{11} = (\bar{C}_{55}b^2 + \bar{C}_{66}a^2)/A^{\ell} \qquad K_{22} = (\bar{C}_{55}d^2 + \bar{C}_{66}c^2)/A^{\ell}$$

$$K_{12} = (\bar{C}_{55}bd + \bar{C}_{66}ac)/A^{\ell} \qquad K_{23} = (\bar{C}_{55}dg + \bar{C}_{66}ce)/A^{\ell}$$

$$K_{13} = (\bar{C}_{55}bg + \bar{C}_{66}ae)/A^{\ell} \qquad K_{24} = (\bar{C}_{26}ac + \bar{C}_{45}db)/A^{\ell}$$

$$K_{14} = (\bar{C}_{26}a^2 + \bar{C}_{45}b^2)/A^{\ell} \qquad K_{25} = (\bar{C}_{26}c^2 + \bar{C}_{45}d^2)/A^{\ell}$$

$$K_{15} = (\bar{C}_{26}ca + \bar{C}_{45}bd)/A^{\ell} \qquad K_{26} = (\bar{C}_{26}ec + \bar{C}_{45}dg)/A^{\ell}$$

$$K_{16} = (\bar{C}_{26}ea + \bar{C}_{45}bg)/A^{\ell} \qquad K_{27} = (\bar{C}_{36}bc + \bar{C}_{45}da)/A^{\ell}$$

$$K_{17} = (\bar{C}_{36}ba + \bar{C}_{45}ba)/A^{\ell} \qquad K_{28} + (\bar{C}_{36}dc + \bar{C}_{45}dc)/A^{\ell}$$

$$K_{18} = (\bar{C}_{36}da + \bar{C}_{45}bc)/A^{\ell} \qquad K_{29} = (\bar{C}_{36}gc + \bar{C}_{45}de)/A^{\ell}$$

$$K_{19} = (\bar{C}_{36}ga + \bar{C}_{45}be)/A^{\ell}$$

$$K_{33} = (\bar{C}_{55}g^2 + \bar{C}_{66}e^2)/A^{\ell} \qquad K_{44} = (\bar{C}_{22}a^2 + \bar{C}_{44}b^2)/A^{\ell}$$

$$K_{34} = (\bar{C}_{26}ae + \bar{C}_{45}gb)/A^{\ell} \qquad K_{45} = (\bar{C}_{22}ac + \bar{C}_{44}bd)/A^{\ell}$$

$$K_{35} = (\bar{C}_{26}ce + \bar{C}_{45}bd)/A^{\ell} \qquad K_{46} = (\bar{C}_{22}ae + \bar{C}_{44}bg)/A^{\ell}$$

$$K_{36} = (\bar{C}_{26}e^2 + \bar{C}_{45}g^2)/A^{\ell} \qquad K_{47} = (\bar{C}_{44}ba + \bar{C}_{23}ab)/A^{\ell}$$

$$K_{37} = (\bar{C}_{36}be + \bar{C}_{45}ga)/A^{\ell} \qquad K_{48} = (\bar{C}_{44}bc + \bar{C}_{23}ad)/A^{\ell}$$

$K_{38} = (\bar{C}_{36}de + \bar{C}_{45}gc)/A^{\ell}$ $\quad K_{49} = (\bar{C}_{44}be + \bar{C}_{23}ag)/A^{\ell}$

$K_{39} = (\bar{C}_{36}ge + \bar{C}_{45}ge)/A^{\ell}$

$K_{55} = (\bar{C}_{22}c^2 + \bar{C}_{44}d^2)/A^{\ell}$ $\quad K_{66} = (\bar{C}_{22}e^2 + \bar{C}_{44}g^2)/A^{\ell}$

$K_{56} = (\bar{C}_{22}ce + \bar{C}_{44}dg)/A^{\ell}$ $\quad K_{67} = (\bar{C}_{44}ga + \bar{C}_{23}eb)/A^{\ell}$

$K_{57} = (\bar{C}_{44}da + \bar{C}_{23}cb)/A^{\ell}$ $\quad K_{68} = (\bar{C}_{44}gc + \bar{C}_{23}eg)/A^{\ell}$

$K_{58} = (\bar{C}_{44}dc + \bar{C}_{23}cd)/A^{\ell}$ $\quad K_{69} = (\bar{C}_{44}ge + \bar{C}_{23}eg)/A^{\ell}$

$K_{59} = (\bar{C}_{44}de + \bar{C}_{23}cg)/A^{\ell}$

$K_{77} = (\bar{C}_{33}b^2 + \bar{C}_{44}a^2)/A^{\ell}$ $\quad K_{88} = (\bar{C}_{33}d^2 + \bar{C}_{44}c^2)/A^{\ell}$

$K_{78} = (\bar{C}_{33}bd + \bar{C}_{44}ac)/A^{\ell}$ $\quad K_{89} = (\bar{C}_{33}dg + \bar{C}_{44}ce)/A^{\ell}$

$K_{79} = (\bar{C}_{33}bg + \bar{C}_{44}ae)/A^{\ell}$ $\quad K_{99} = (\bar{C}_{33}g^2 + \bar{C}_{44}e^2)/A^{\ell}$

$S_1 = \bar{C}_{16}\ a \quad S_2 = \bar{C}_{16}\ c \quad S_3 = \bar{C}_{16}\ e$

$S_4 = \bar{C}_{12}\ a \quad S_5 = \bar{C}_{12}\ c \quad S_6 = \bar{C}_{12}\ e$

$S_7 = \bar{C}_{13}\ b \quad S_8 = \bar{C}_{13}\ d \quad S_9 = \bar{C}_{13}\ g$

$x_1 = u_1 \quad x_2 = u_2 \quad x_3 = u_3$

$x_4 = v_1 \quad x_5 = v_2 \quad x_6 = v_3$

$x_7 = w_1 \quad x_8 = w_2 \quad x_9 = w_3$

$$F_1 = f_x^1 \qquad F_2 = f_x^2 \qquad F_3 = f_x^3$$
$$F_4 = f_y^1 \qquad F_5 = f_y^2 \qquad F_3 = f_y^3$$
$$F_7 = f_z^1 \qquad F_8 = f_z^2 \qquad F_8 = f_z^3$$

where f's are nodal forces.

For Equ's. (A.2) the previously defined terms apply plus the following additional terms

$$K_{110} = \bar{C}_{16}a \qquad K_{210} = \bar{C}_{16}c \qquad K_{310} = \bar{C}_{16}e$$
$$K_{410} = \bar{C}_{12}a \qquad K_{510} = \bar{C}_{12}c \qquad K_{610} = \bar{C}_{16}e$$
$$K_{710} = \bar{C}_{13}b \qquad K_{810} = \bar{C}_{13}d \qquad K_{910} = \bar{C}_{13}g$$
$$K_{1010} = \bar{C}_{11}A^{\ell}$$

$$X_{10} = \bar{\xi}_x \qquad F_{10} = F^*$$

$$T_1 = (\bar{C}_{16} + \varepsilon_x^T + \bar{C}_{26}\varepsilon_y^T + \bar{C}_{36}\varepsilon_z^T + \bar{C}_{66}\gamma_{xy}^T)a$$

$$T_2 = (\bar{C}_{16}\varepsilon_x^T + \bar{C}_{26}\varepsilon_y^T + \bar{C}_{36}\varepsilon_z^T + \bar{C}_{66}\gamma_{xy}^T)c$$

$$T_3 = (\bar{C}_{16}\varepsilon_x^T + \bar{C}_{26}\varepsilon_y^T + \bar{C}_{36}\varepsilon_z^T + \bar{C}_{66}\gamma_{xy}^T)e$$

$$T_4 = (\bar{C}_{12}\varepsilon_x^T + \bar{C}_{22}\varepsilon_y^T + \bar{C}_{23}\varepsilon_z^T + \bar{C}_{26}\gamma_{xy}^T)a$$

$$T_5 = (\bar{C}_{12}\varepsilon_x^T + \bar{C}_{22}\varepsilon_y^T + \bar{C}_{23}\varepsilon_z^T + \bar{C}_{26}\gamma_{xy}^T)c$$

$$T_6 = (\bar{C}_{12}\varepsilon_x^T + \bar{C}_{22}\varepsilon_y^T + \bar{C}_{23}\varepsilon_z^T + \bar{C}_{26}\gamma_{xy}^T)e$$

$$T_7 = (\bar{C}_{13}\varepsilon_x^T + \bar{C}_{23}\varepsilon_y^T + \bar{C}_{33}\varepsilon_z^T + \bar{C}_{36}\gamma_{xy}^T)b$$

$$T_8 = (\bar{C}_{13}\varepsilon_x^T + \bar{C}_{23}\varepsilon_y^T + \bar{C}_{33}\varepsilon_z^T + \bar{C}_{36}\gamma_{xy}^T)d$$

$$T_9 = (\bar{C}_{13}\varepsilon_x^T + \bar{C}_{23}\varepsilon_y^T + \bar{C}_{33}\varepsilon_z^T + \bar{C}_{36}\gamma_{xy}^T)g$$

$$T_{10} = (\bar{C}_{11}\varepsilon_x^T + \bar{C}_{12}\varepsilon_y^T + \bar{C}_{13}\varepsilon_z^T + \bar{C}_{16}\gamma_{xy}^T)A^{\ell}$$

where

$$\varepsilon_x^T = (m^2\alpha_1 + n^2\alpha_2)\Delta T$$

$$\varepsilon_y^T = (n^2\alpha_1 + m^2\alpha_2)\Delta T$$

$$\varepsilon_z^T = \alpha_3\Delta T$$

$$\gamma_{xy}^T = 2mn(\alpha_1-\alpha_2)\Delta T$$

For moisture analysis the vector {T} is identical except α_1, α_2 and α_3 are replaced by β_1, β_2 and β_3.

APPENDIX B

ADDENDA TO RFERENCE [1]

During the process of modifying the program developed by Renieri and Herakovich [1] it was discovered that a coding error had been made in the equations for the transformation matrices. (Chap. 3, Equ's. 3.9.) This was corrected and the nonlinear stress-strain response predictions of Ref. [1] were regenerated using the same data and finite element model. In the majority of cases the differences proved to be negligible. For the cases where the differences were significant, comparisons between results obtained from the corrected program and experiment are presented. It should be noted that the coding errors applied only to the nonlinear results presented in Ref. [1] and not the elastic results. It should also be noted that no attempt to define failure was made by this investigator and that the last point plotted does not necessarily correspond to failure.

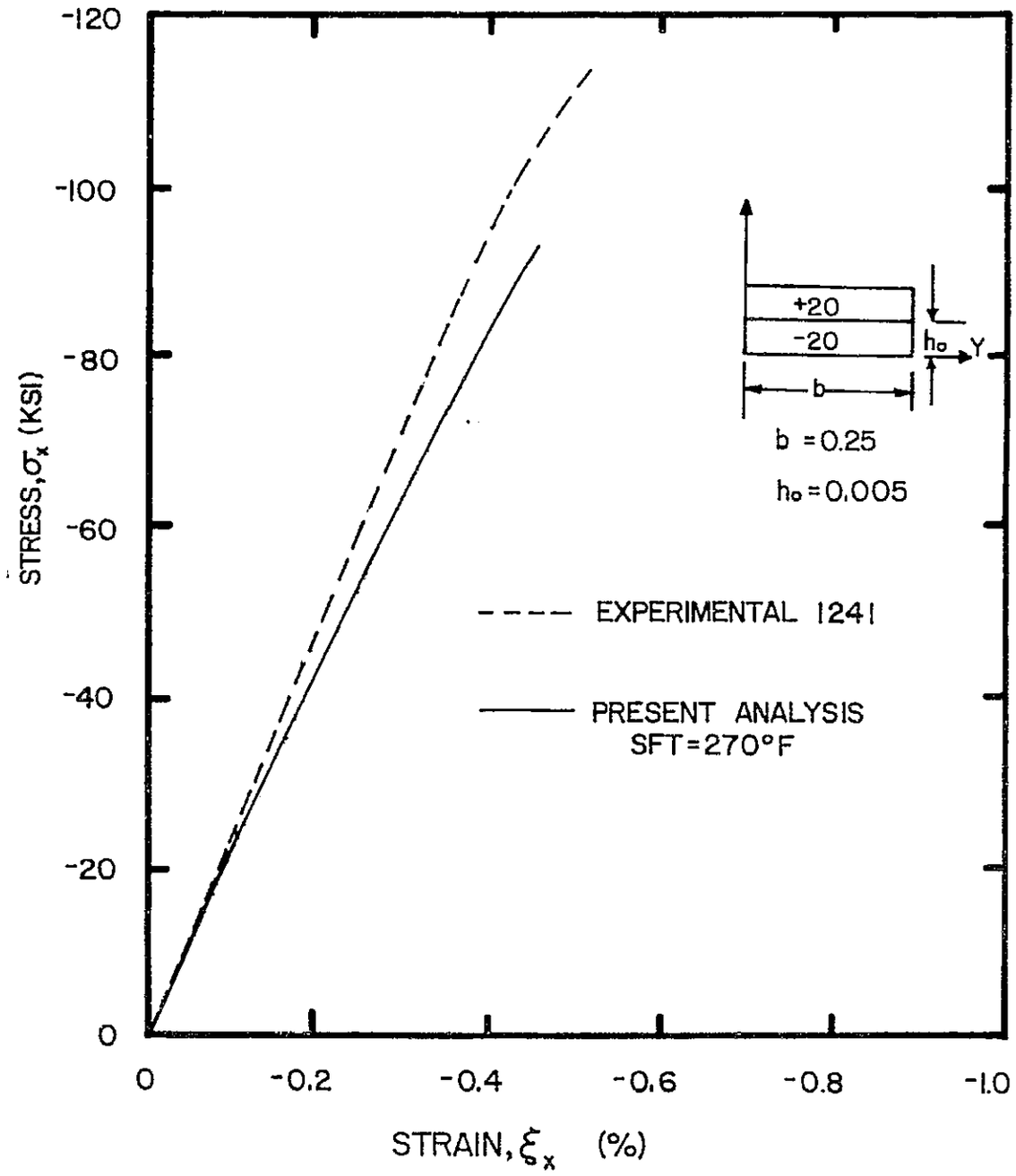

Figure B.1. Compression Stress-Strain Behavior of $[\pm 20]_s$ Boron/Epoxy Laminate-Sandwich Beam Data

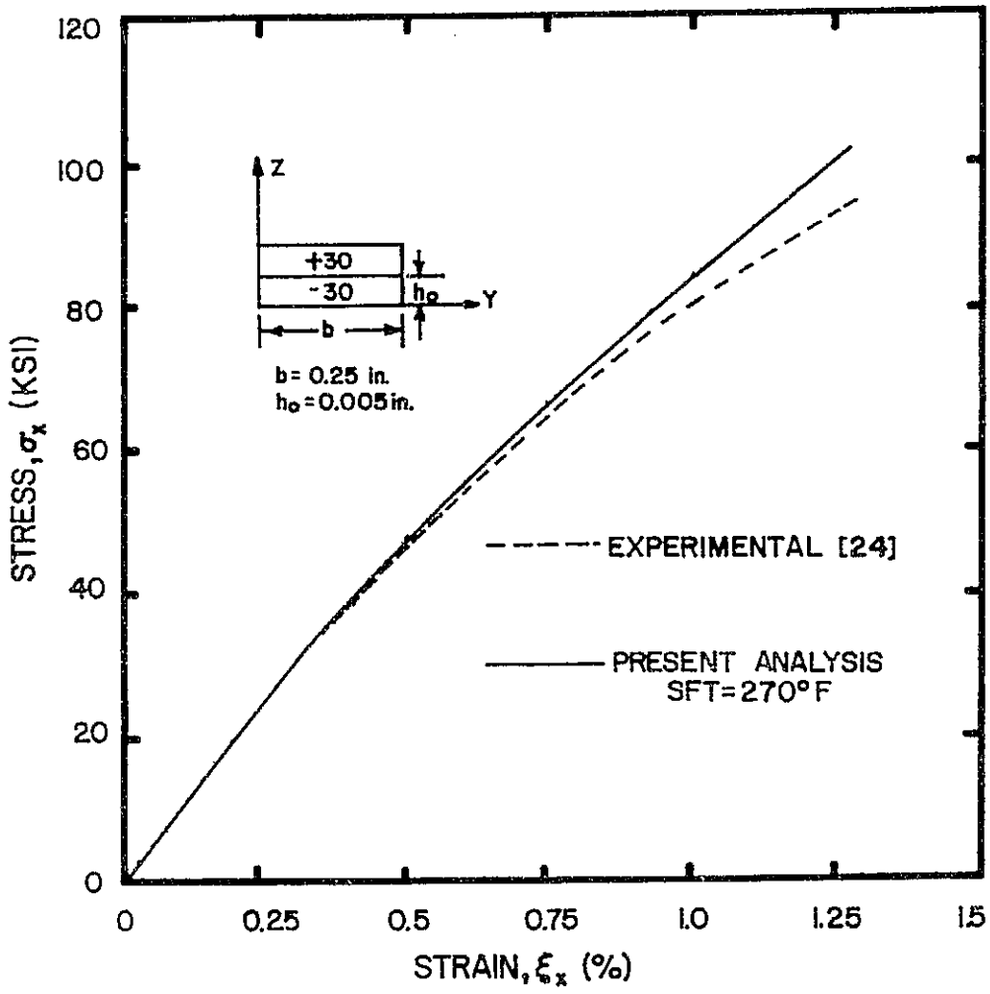

Figure B.2. Tensile Stress-Strain Behavior of $[\pm 30]_s$ B/E Laminate-Sandwich Beam Data

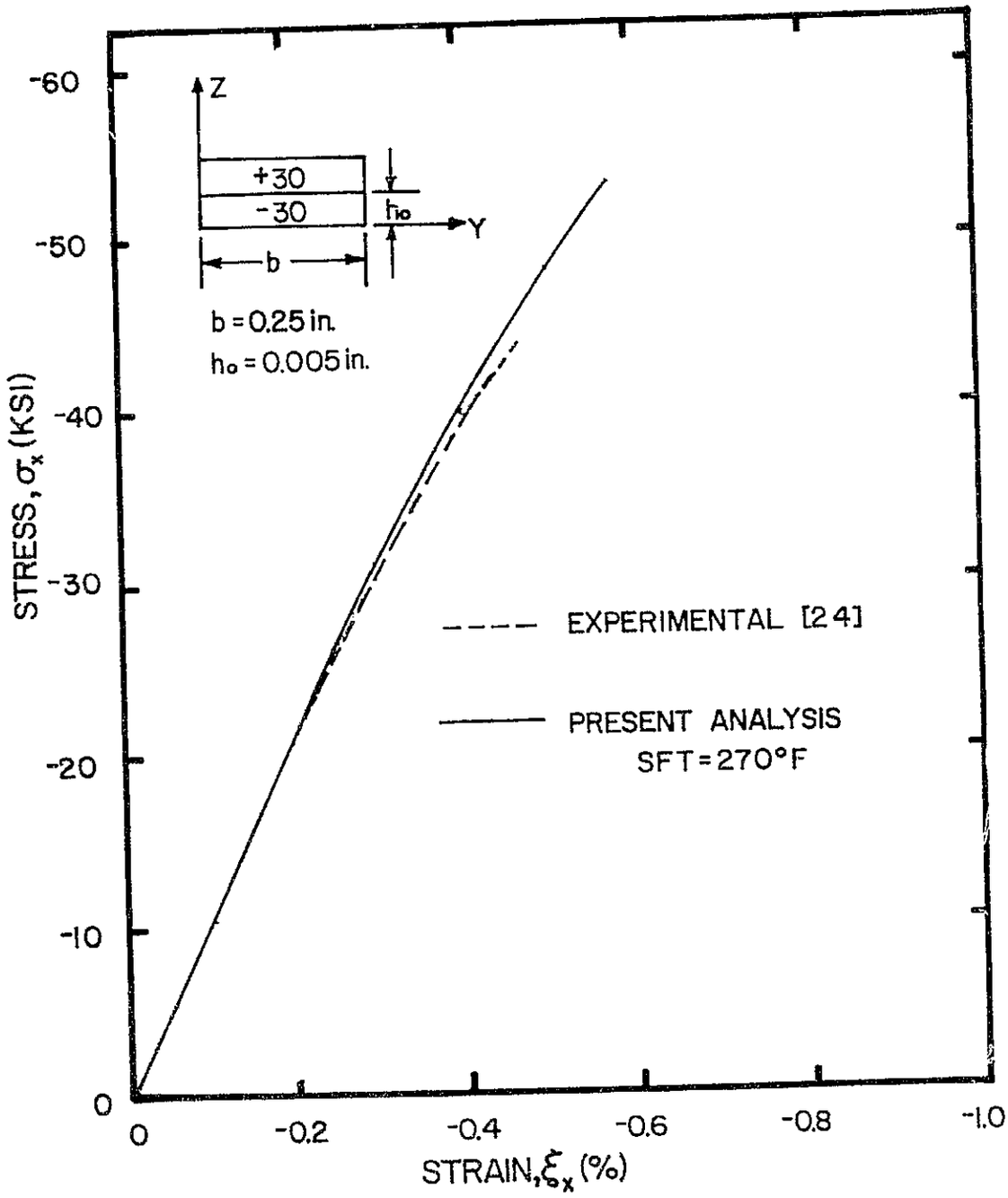

Figure B.3 Compressive Stress-Strain Behavior of $[\pm 30]_s$ B/E Laminate-Sandwich Beam Data

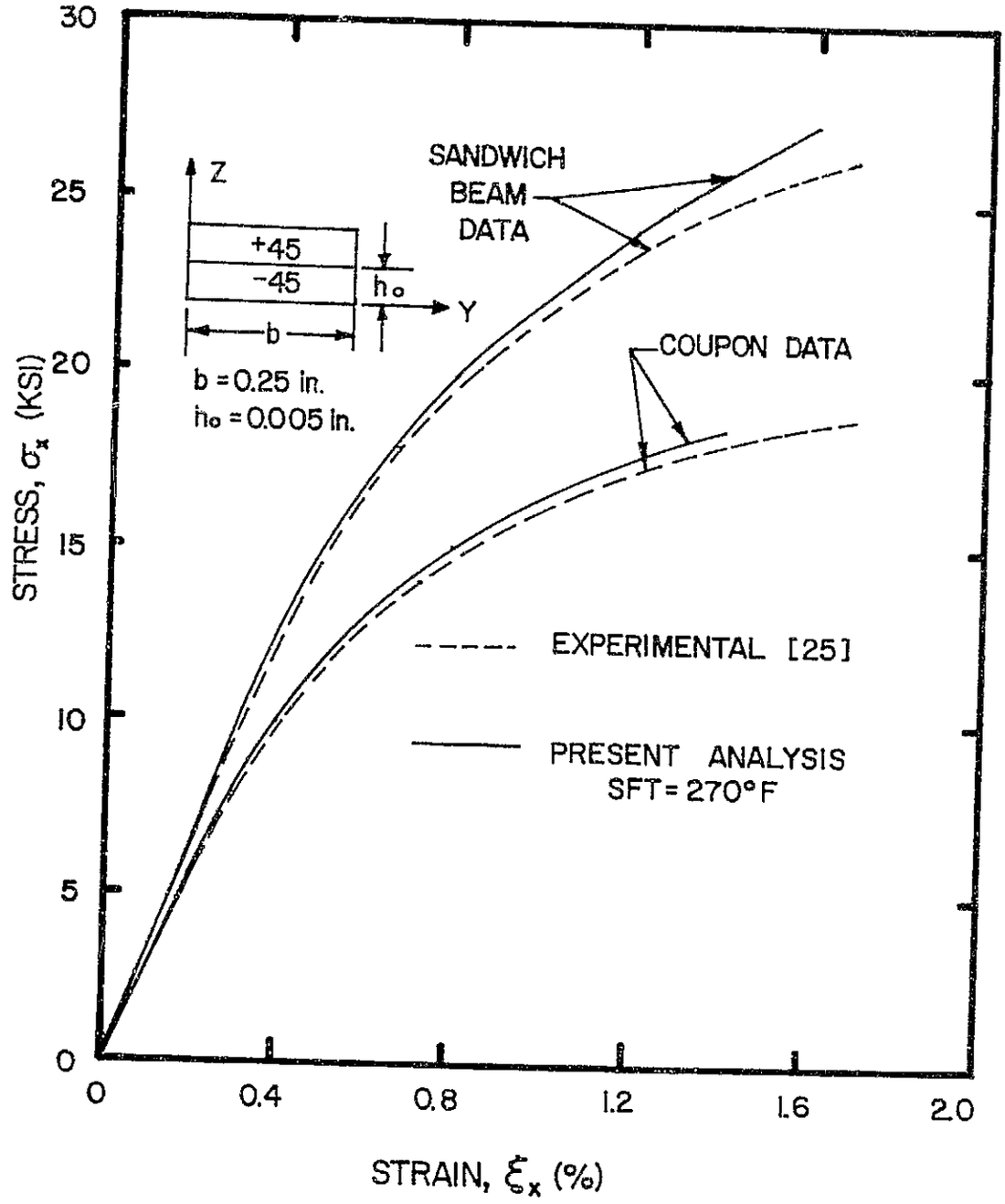

Figure B.4. Tensile Stress-Strain Behavior of $[\pm 45]_s$ B/E Laminate

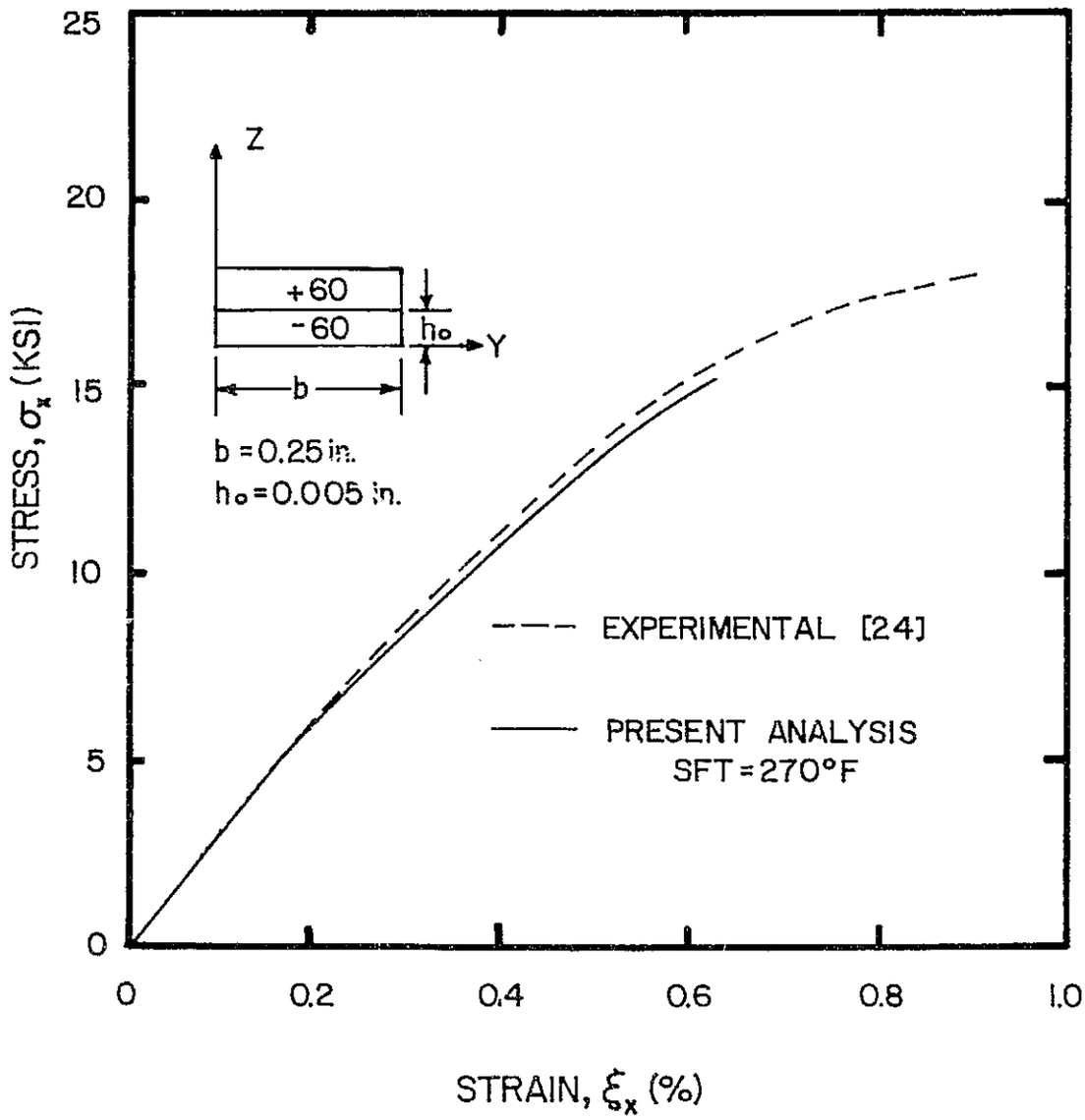

Figure B.5. Tensile Stress-Strain Behavior of $[\pm 60]_s$ B/E Laminate-Sandwich Beam Data

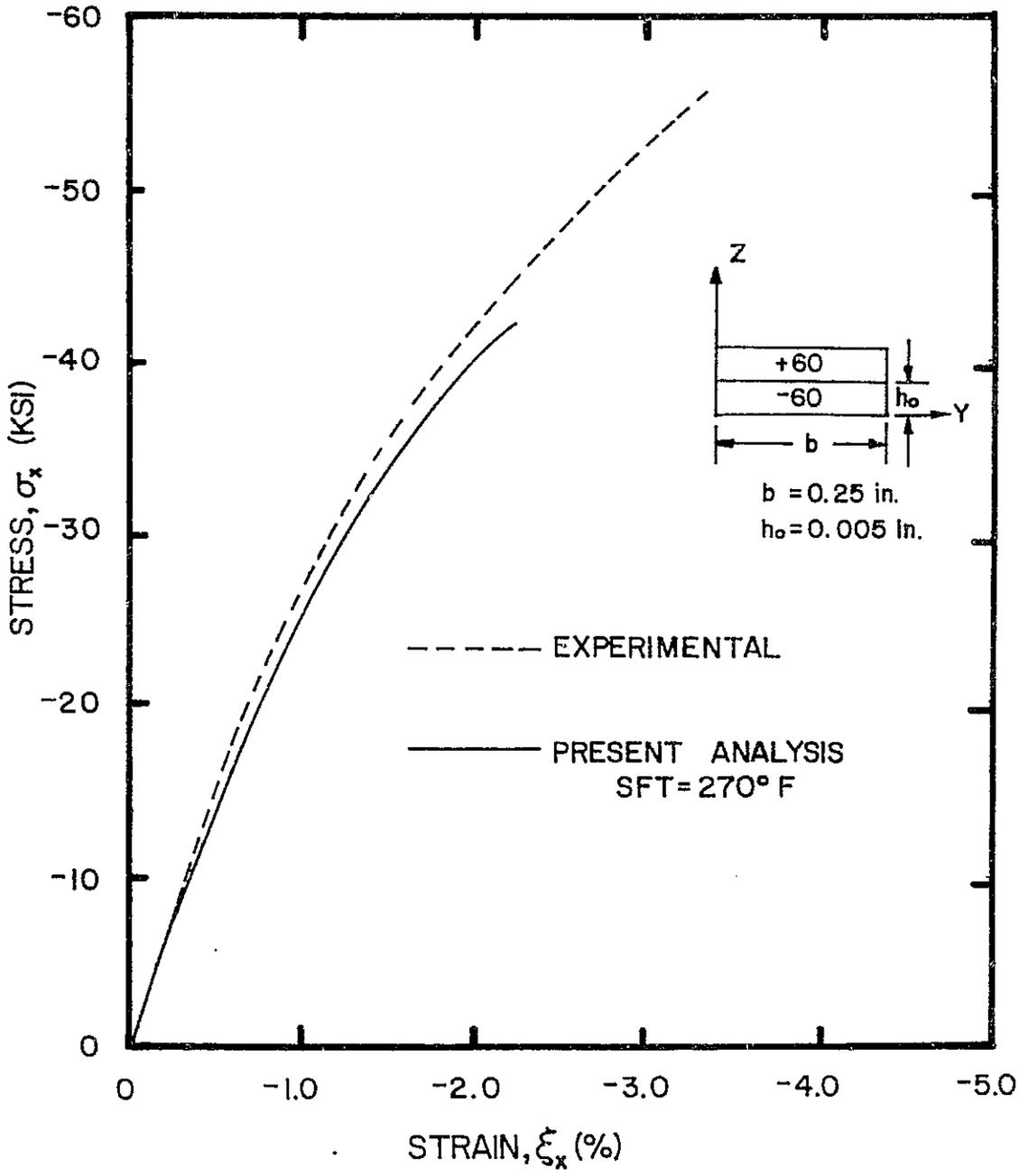

Figure B.6. Compressive Stress-Strain Behavior of $[\pm 60]_s$ B/E Laminate-Sandwich Beam Data

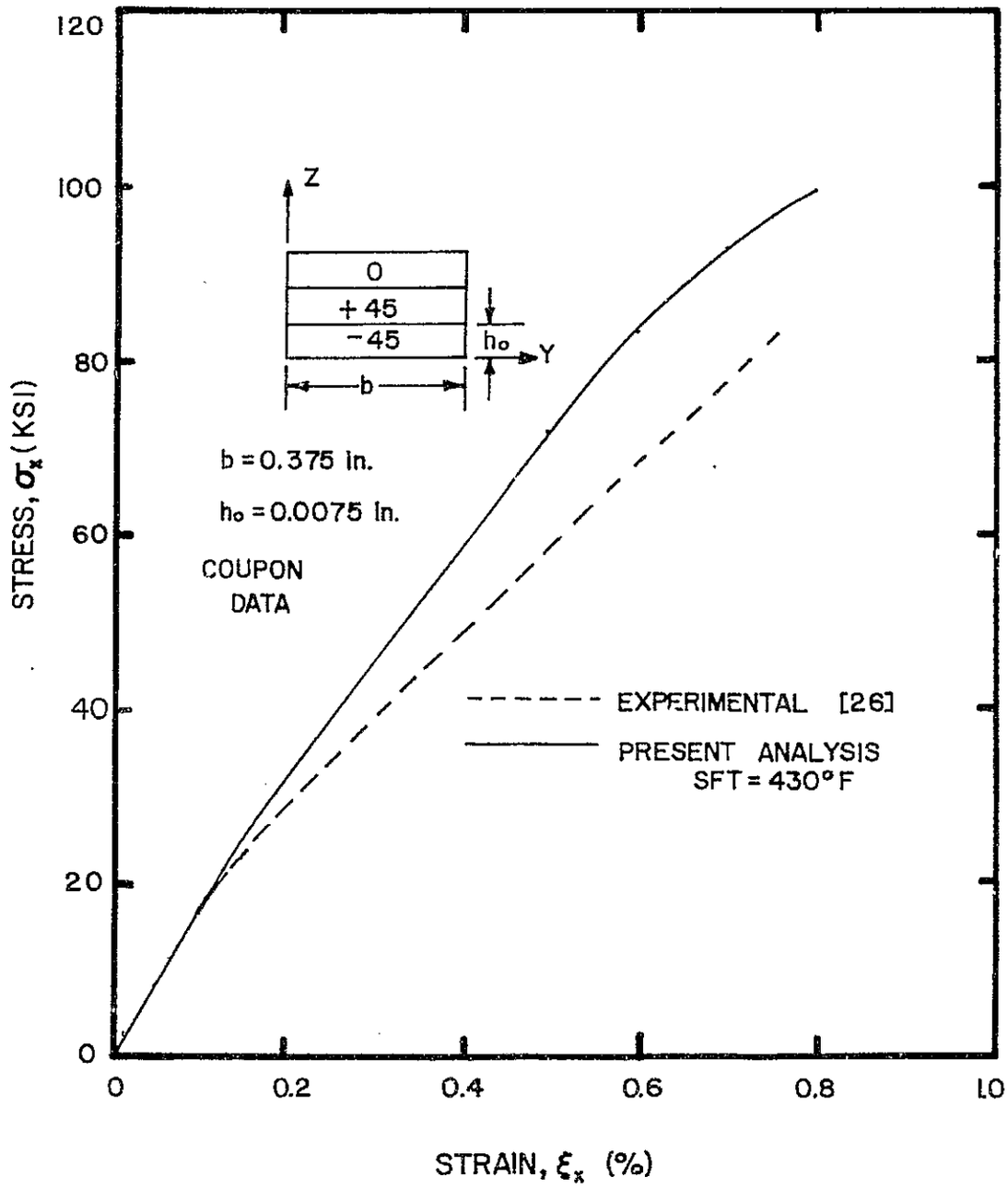

Figure B.7. Tensile Stress-Strain Behavior of $[0/\pm45]_s$ Bs/Al Laminate

APPENDIX C

MATERIAL PROPERTIES

This appendix contains all of the material properties used for this study. The data presented represents typical data from the literature. References are provided where appropriate. Fig's. C.1 through C.7 represent the stress-strain response of the materials used. Table C.1 contains the Ramberg-Osgood coefficients for these materials and Table C.2 contains the temperature dependent properties.

In Table C.1 the symbol σ^* refers to the stress at which the Ramberg-Osgood coefficients n_2 and k_2 become applicable.

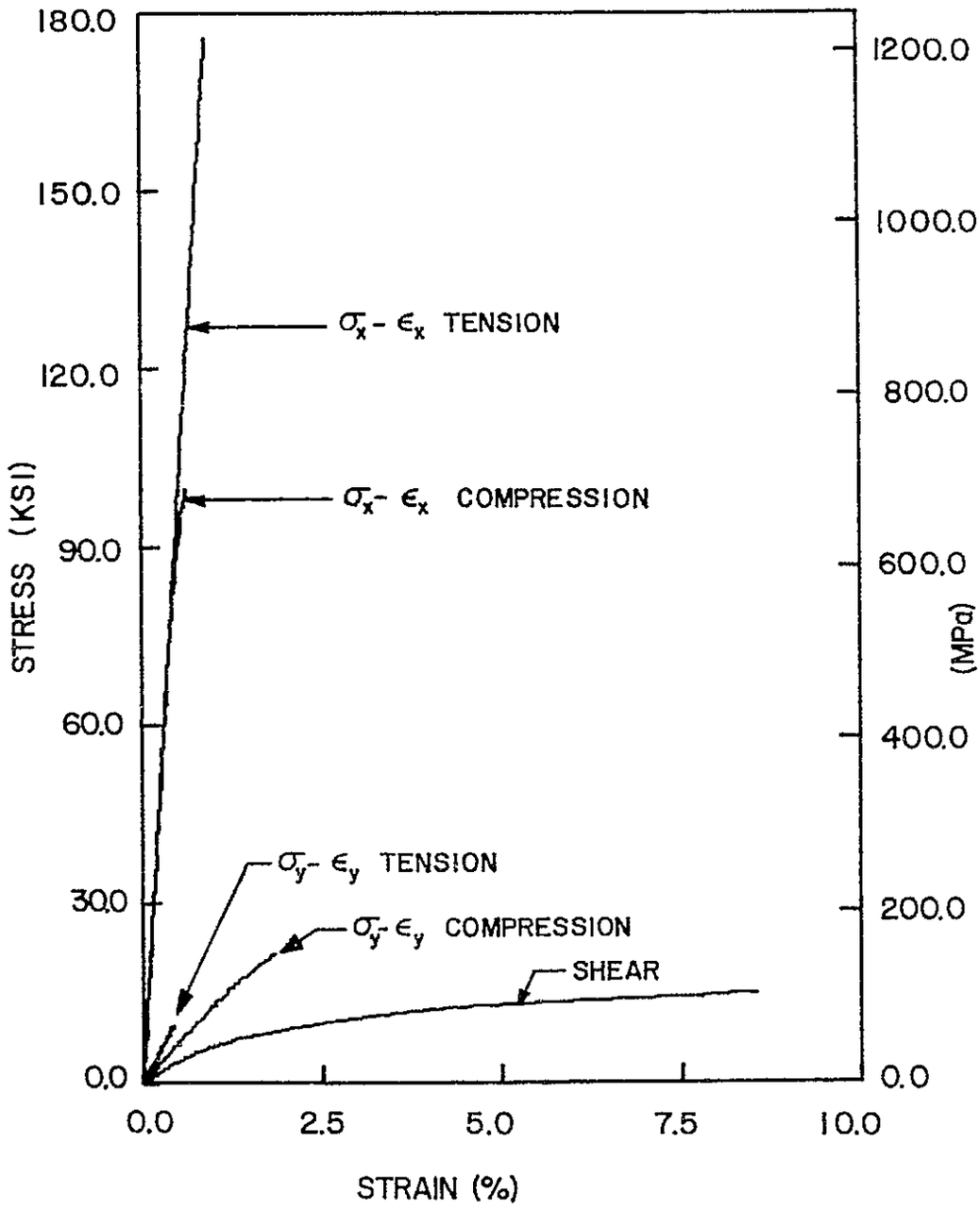

Figure C.1. Stress-Strain Response of Unidirectional Gr/Pi

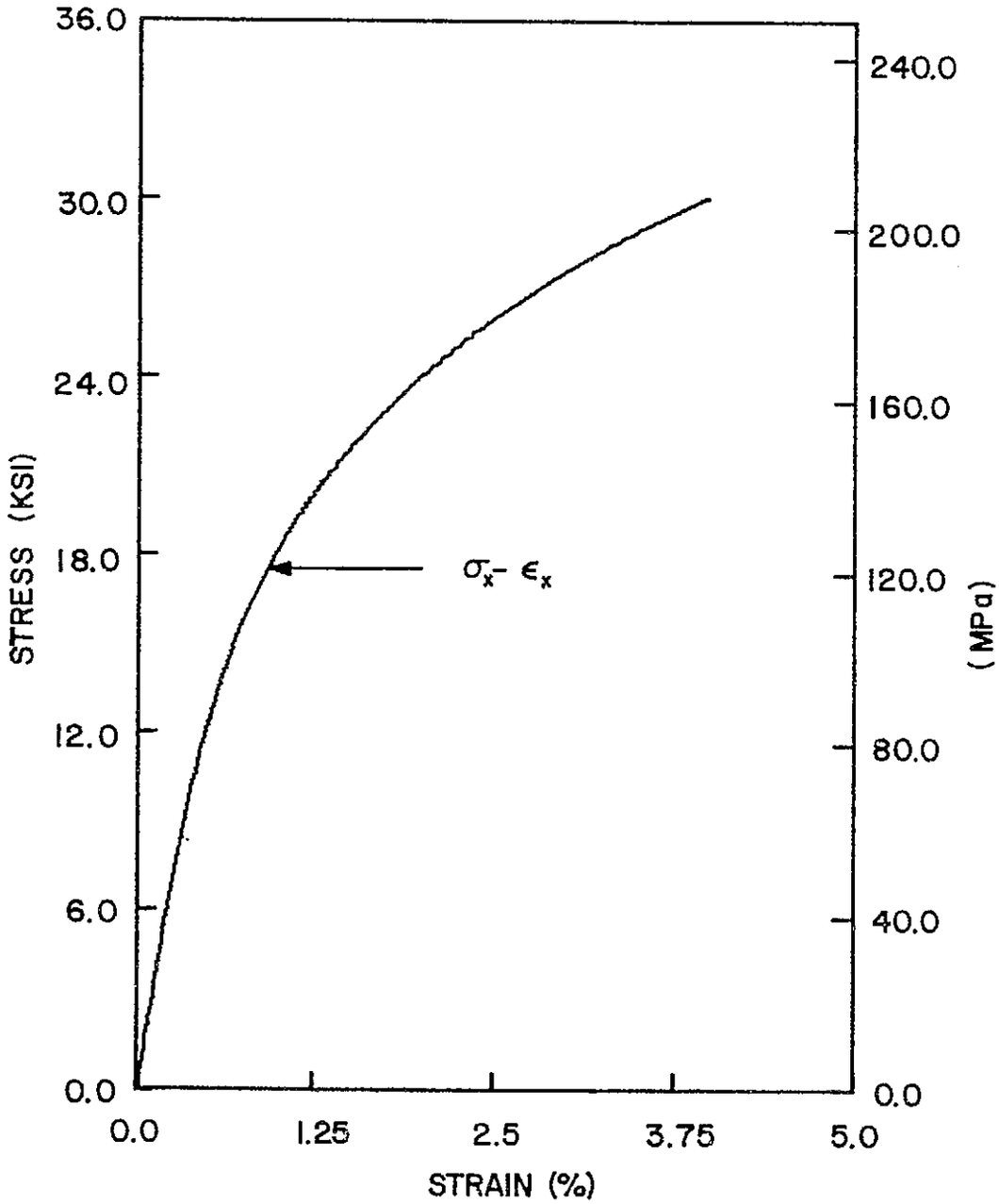

Figure C.2. Stress-Strain Response of $[\pm 45]_s$ Laminate Gr/Pi

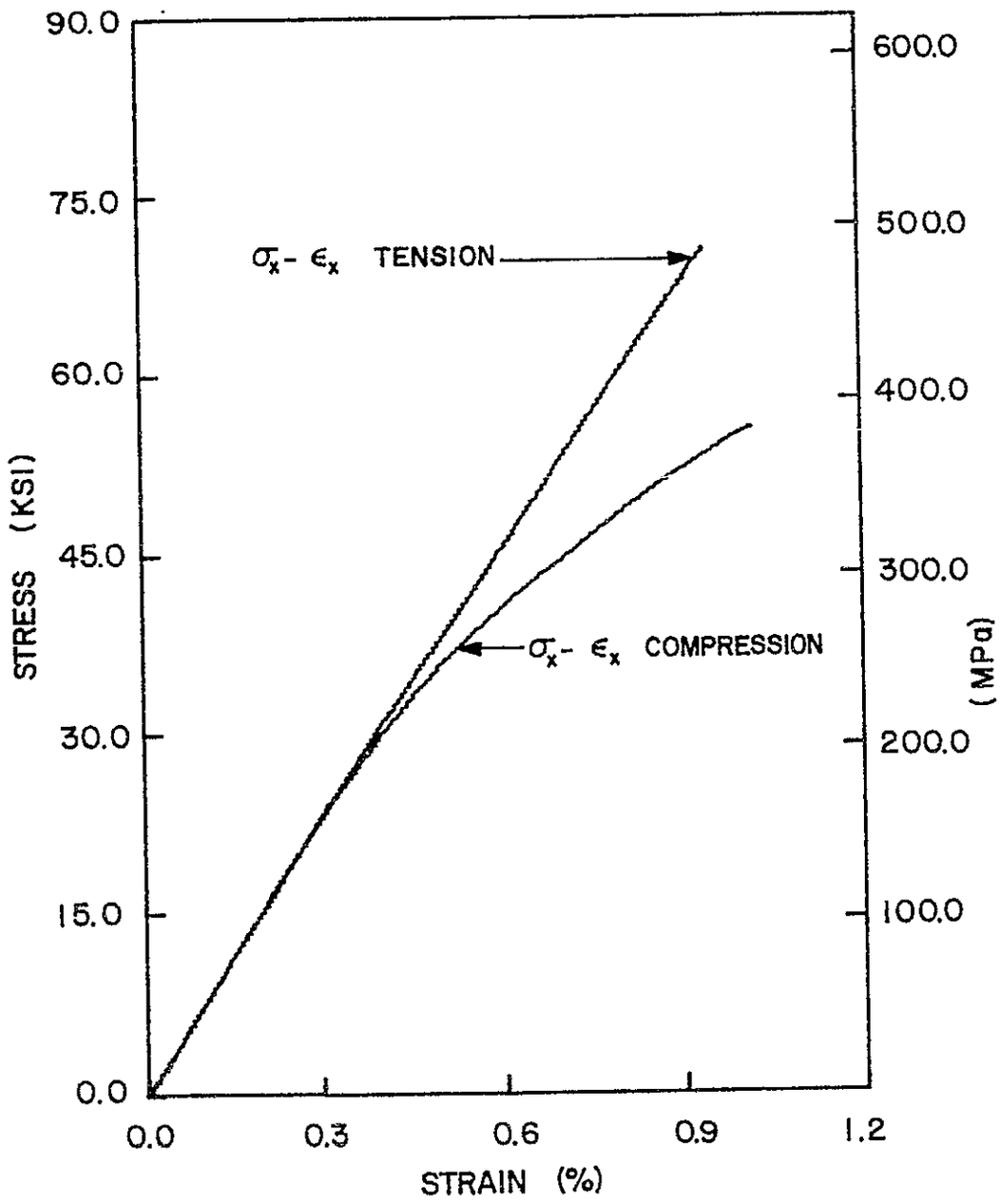

Figure C.3. Stress-Strain Response of $[0/\pm45/90]_s$ Laminate Gr/Pi

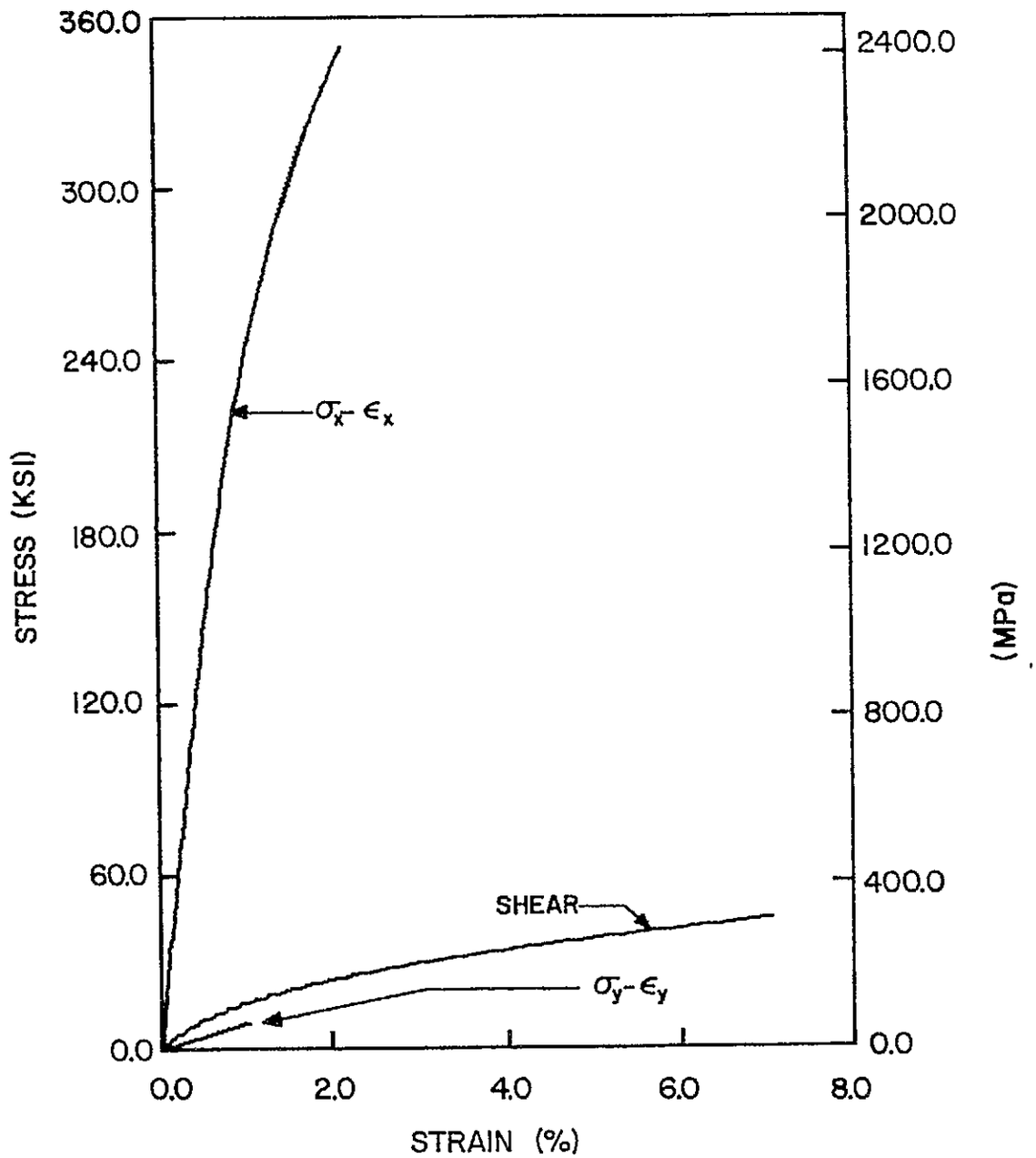

Figure C.4. Stress-Strain Response of Unidirectional B/E
Ref. [15]

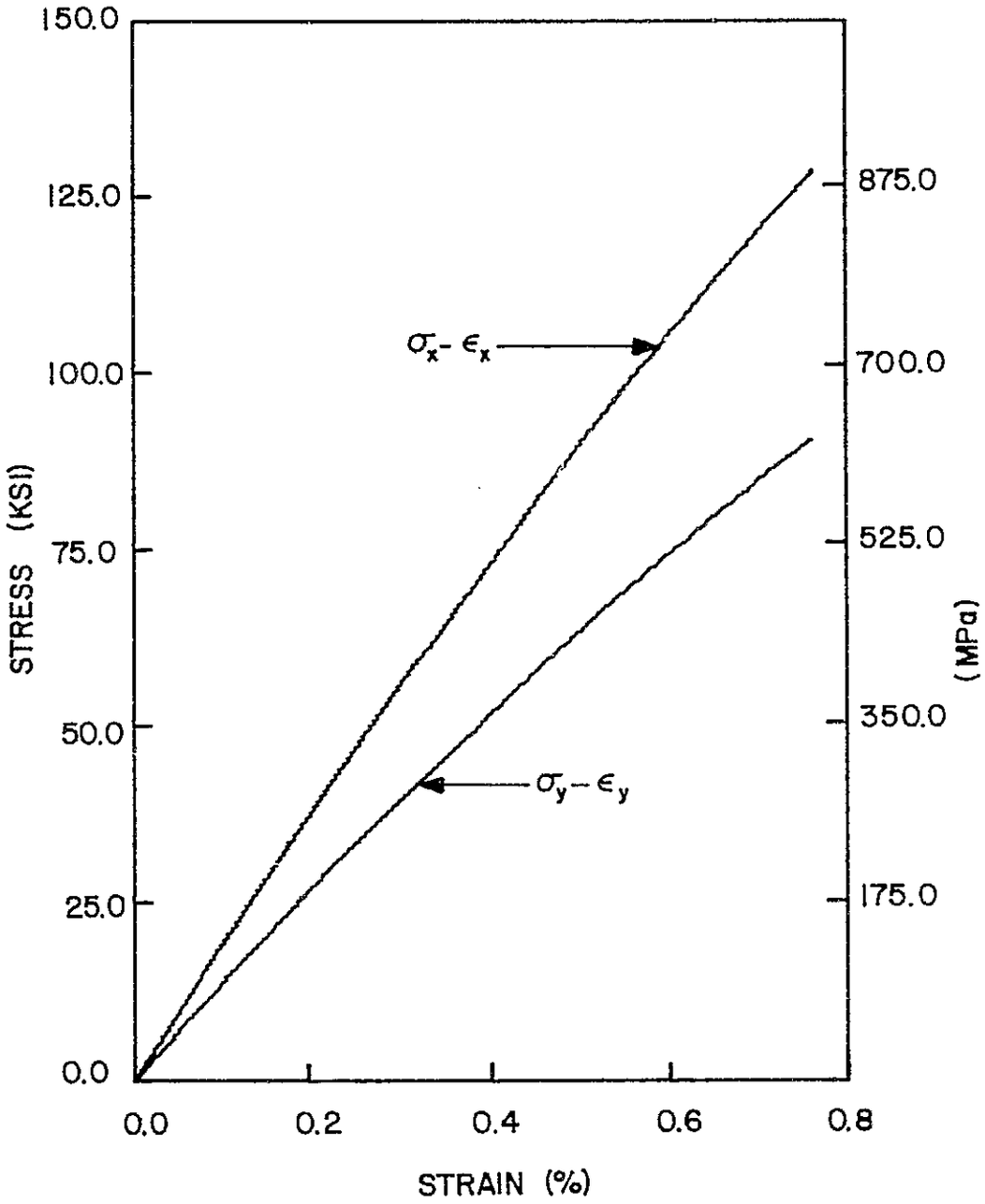

Figure C.5. Stress-Strain Response of [0/90/0/90/0] Laminate B/E

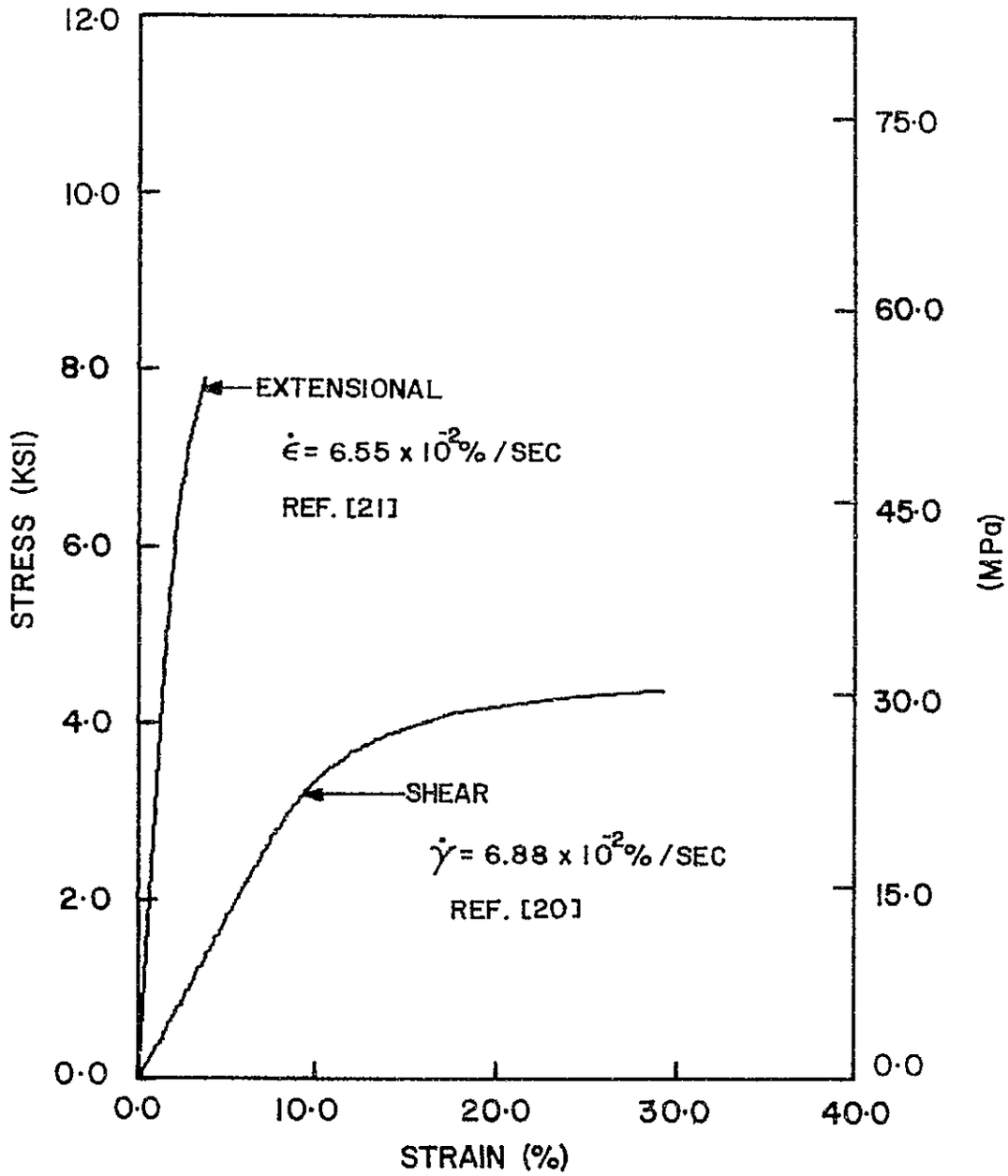

Figure C.6. Stress-Strain Response of Metlbond 1113 Adhesive

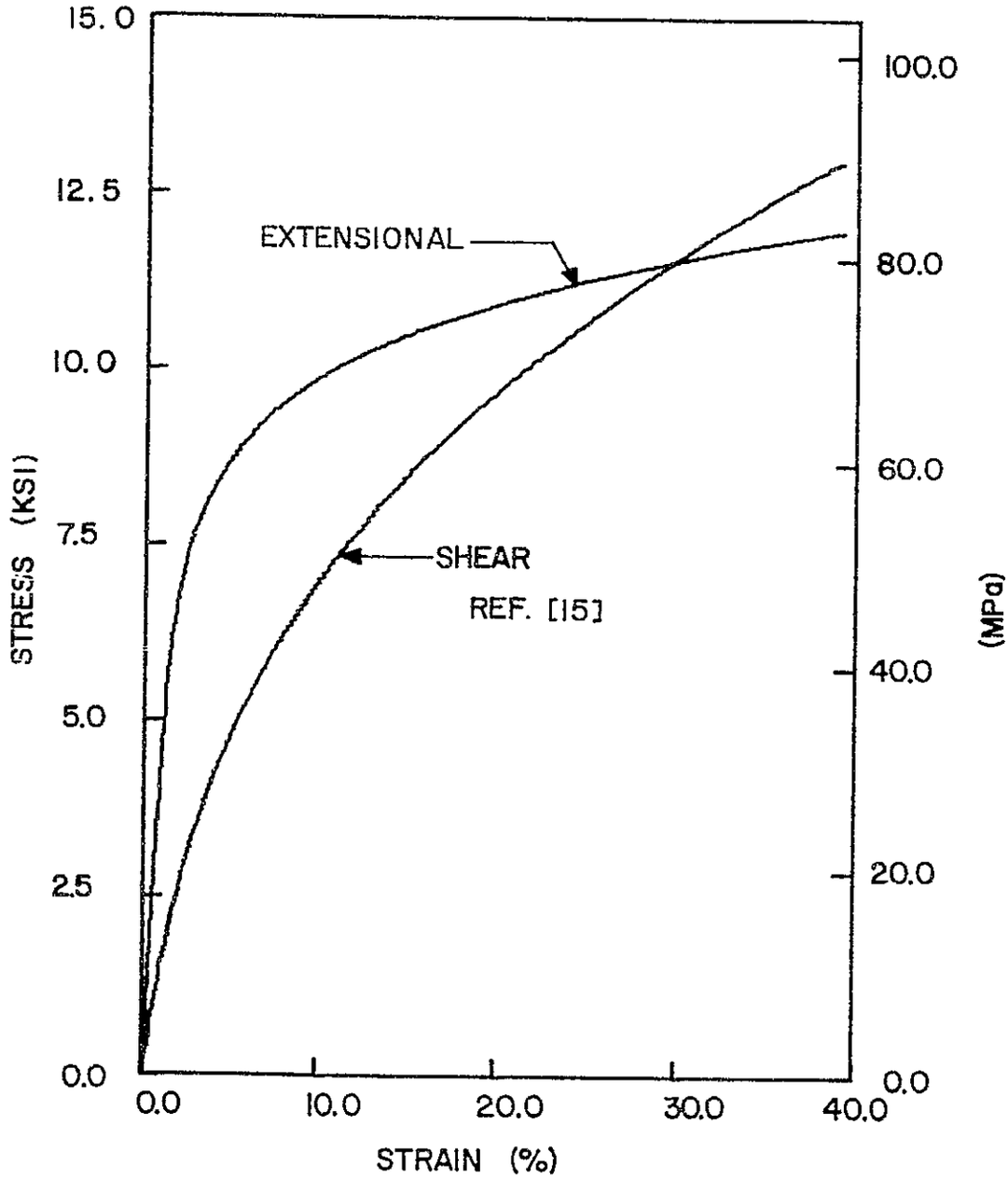

Figure C.7. Stress-Strain Response of AF-126-2 Adhesive

TABLE C.1 Ramberg-Osgood Coefficients

Matl.	Curve	Elastic Modulus (MSI)	ν	Elastic Limit (KSI)	n_1	K_1 (PSI^{-n_1})	σ^* (KSI)	n_2	K_2 (PSI^{-n_2})	Ultimate Stress (KSI)
Unidirectional GR/PI	E_{xx} Tension	19.0	.21 (ν_{xy})							176.0
	E_{xx} Comp.	19.0	.21 (ν_{xy})	38.0	9.593	1.1087×10^{-51}	16.8			100.0
	E_{yy} Tension	2.2	.21 (ν_{yz})							9.7
	E_{yy} Comp.	1.8	.21 (ν_{yz})	0.872	1.253	1.9509×10^{-8}	16.8	2.0661	7.181×10^{-12}	21.8
	E_{zz} Tension	2.2	.21 (ν_{xz})							9.7
	E_{zz} Comp	1.8	.21 (ν_{xz})	0.872	1.253	1.9509×10^{-8}	16.8	2.0661	7.181×10^{-12}	21.8
	G_{yz}	0.85		0.1	3.411	2.7474×10^{-16}	12.6	5.316	4.254×10^{-24}	15.0
	G_{xz}	0.85		0.1	3.411	2.7474×10^{-16}	12.6	5.316	4.254×10^{-24}	15.0
	G_{xy}	0.85		0.1	3.411	2.7474×10^{-16}	12.6	5.316	4.254×10^{-24}	15.0

TABLE C.1 Cont.

Matl.	Curve	Elastic Modulus (MSI)	ν	Elastic Limit (KSI)	n_1	K_1 (PSI^{-n_1})	σ^* (KSI)	n_2	K_2 (PSI^{-n_2})	Ultimate Stress (KSI)
$[\pm 45]_s$ GR/PI	Exx Tension	2.95	.75 (ν_{xy})	1.2	4.064	1.856×10^{-20}				30.1
	Exx Comp.	2.95	.75 (ν_{xy})	1.2	4.064	1.856×10^{-20}				30.1
	Eyy Tension	2.95	.21 (ν_{yz})	1.2	4.064	1.856×10^{-20}				30.1
	Eyy Comp.	2.95	.21 (ν_{yz})	1.2	4.064	1.856×10^{-20}				30.1
	Ezz Tension	2.2	.21 (ν_{xz})							9.7
	Ezz Comp.	1.8	.21 (ν_{xz})		1.253	1.9509×10^{-8}	16.8	2.0661	7.181×10^{-12}	21.8
	G_{yz}	0.85		0.1	3.411	2.7474×10^{-16}	12.6	5.3158	4.254×10^{-24}	15.0
	G_{xz}	0.85		0.1	3.411	2.7474×10^{-16}	12.6	5.3158	4.254×10^{-24}	15.0
	G_{xy}	5.1								15.0

TABLE C.1 Cont.

Matl.	Curve	Elastic Modulus (MSI)	ν	Elastic Limit (KSI)	n_1	K_1 (PSI^{-n_1})	σ^* (KSI)	n_2	K_2 (PSI^{-n_2})	Ultimate Stress (KSI)
$[0/\pm45/90]_s$ GR/PI	E_{xx} Tension	7.75	.30 (ν_{xy})	2.0	2.422	5.332×10^{-16}				70.6
	E_{xx} Comp.	7.75	.30 (ν_{xy})	2.16	5.538	2.243×10^{-29}	44.7	3.904	8.872×10^{-29}	55.6
	E_{yy} Tension	7.75	.21 (ν_{yz})	2.0	2.422	5.332×10^{-16}				70.6
	E_{yy} Comp.	7.75	.21 (ν_{yz})	2.16	5.538	2.243×10^{-29}	44.7	3.904	8.872×10^{-29}	55.6
	E_{zz} Tension	2.2	.21 (ν_{xz})							9.7
	E_{zz} Comp.	1.8	.21 (ν_{xz})	0.87	1.253	1.9509×10^{-8}	16.8	2.0661	7.181×10^{-12}	21.8
	G_{yz}	0.85		0.1	3.411	2.747×10^{-16}	12.6	5.316	4.254×10^{-24}	15.0
	G_{xz}	0.85		0.1	3.411	2.747×10^{-16}	12.6	5.316	4.254×10^{-24}	15.0
	G_{xy}	2.97								15.0

TABLE C.1 Cont.

Matl.	Curve	Elastic Modulus (MSI)	ν	Elastic Limit (KSI)	n_1	K_1 (PSI^{-n1})	σ^* (KSI)	n_2	K_2 (PSI^{-n2})	Ultimate Stress (KSI)
Unidirectional B/E*	E_{xx} Tension	29.6	.21 (ν_{xy})	1.0	4.463	1.8534×10^{-27}				200.5
	E_{xx} Comp.	29.6	.53 (ν_{xy})	1.0	4.463	1.8534×10^{-27}				350.0
	E_{yy} Tension	2.75	.35 (ν_{yz})	1.0	2.541	8.1604×10^{-14}				9.6
	E_{yy} Comp.	2.75	.35 (ν_{yz})	1.0	2.541	8.1604×10^{-14}				45.0
	E_{zz} Tension	2.75	.35 (ν_{xz})	1.0	2.541	8.1604×10^{-14}				9.6
	E_{zz} Comp.	2.75	.35 (ν_{xz})	1.0	2.541	8.1604×10^{-14}				45.0
	G_{yz}	0.933		0.1	2.991	7.8797×10^{-15}				9.5
	G_{xz}	0.933		0.1	2.991	7.8797×10^{-15}				9.5
	G_{xy}	0.933		0.1	2.991	7.8797×10^{-15}				9.5

* Ref [11].

TABLE C.1 Cont.

Matl.	Curve	Elastic Modulus (MSI)	ν	Elastic Limit (KSI)	n_1	K_1 (PSI^{-n_1})	σ^* (KSI)	n_2	K_2 (PSI^{-n_2})	Ultimate Stress (KSI)
[0/90/0/90/0] B/E	E_{xx} Tension	18.9	.031 (ν_{xy})	5.16	3.351	6.0822×10^{-21}				129.0
	E_{xx} Comp.	18.9	.108 (ν_{xy})	5.16	3.351	6.0822×10^{-21}				129.0
	E_{yy} Tension	13.5	.35 (ν_{yz})	5.44	3.05	6.7331×10^{-19}				90.7
	E_{yy} Comp.	13.5	.35 (ν_{yz})	5.44	3.05	6.7731×10^{-19}				90.7
	E_{zz} Tension	2.75	.35 (ν_{xz})	1.0	2.45	8.1604×10^{-14}				9.6
	E_{zz} Comp.	2.75	.35 (ν_{xz})	1.0	2.45	8.1604×10^{-14}				45.0
	G_{yz}	0.933		0.1	2.991	7.8797×10^{-15}				9.5
	G_{xz}	0.933		0.1	2.991	7.8797×10^{-15}				9.5
	G_{xy}	0.933		0.1	2.991	7.8797×10^{-15}				9.5

TABLE C.1 Cont.

Matl.	Curve	Elastic Modulus (MSI)	ν	Elastic Limit (KSI)	n_1	K_1 (PSI^{-n_1})	σ^* (KSI)	n_2	K_2 (PSI^{-n_2})	Ultimate Stress (KSI)
Metlbond 1113	Exten.*	0.325	.366	1.58	7.907	2.039×10^{-33}				7.902
	Shear**	0.0363		1.32	10.45	1.032×10^{-39}	4.14	16.67	3.162×10^{-62}	4.39
AF-126-2	Exten.	0.455	.30	1.58	7.907	2.039×10^{-33}				12.0
	Shear***	0.175		0.1	2.684	2.88×10^{-12}				13.0
Titanium 6Al-4V	Exten. +	15.8	.34							130.0
	Shear +	6.0								68.9
Aluminum 2024-T4	Exten. +	10.6	.33							44.0
	Shear +	4.0								25.0

* Ref. [21]. + Ref. [22].

** Ref. [20].

*** Ref. [11].

TABLE C.2 Thermal Properties

Matl.	Temp. °F	% E_{xx}	% E_{yy}	% E_{zz}	% G_{yz}	% G_{xz}	% G_{xy}	α_1 (in/in/°F)	α_2 (in/in/°F)	α_3 (in/in/°F)
Unidirectional GR/PI	0.0	100.0	100.0	100.0				0.0*	14.1×10^{-6}*	14.1×10^{-6}*
	60.0				100.0**	100.0**	100.0**			
	400.0				93.0**	93.0**	93.0**			
	500.0				75.0**	75.0**	75.0**			
	550.0	115.0	50.0	50.0				0.0*	14.1×10^{-6}*	14.1×10^{-6}*
$[\pm 45]_s$ GR/PI	0.0			100.0						14.1×10^{-6}
	60.0				100.0	100.0				
	70.0	100.0	100.0				100.0	1.7×10^{-6}	1.7×10^{-6}	
	400.0	94.0	94.0		93.0	93.0	107.0	1.04×10^{-6}	1.04×10^{-6}	
	500.0	78.0	78.0		75.0	75.0	111.0	$.864 \times 10^{-6}$	$.864 \times 10^{-6}$	
	550.0			50.0						14.1×10^{-6}

* Ref. [19].

** Ref. [23].

TABLE C.2 Cont.

Matl.	Temp. °F	% E_{xx}	% E_{yy}	% E_{zz}	% G_{yz}	% G_{xz}	% G_{xy}	α_1 (in/in/°F)	α_2 (in/in/°F)	α_3 (in/in/°F)
$[0/\pm45/90]_s$ GR/PI	0.0			100.0						14.1×10^{-6}
	60.0				100.0	100.0				
	70.0	100.0	100.0				100.0	1.7×10^{-6}	1.7×10^{-6}	
	400.0	105.0	105.0		93.0	93.0	105.0	1.04×10^{-6}	1.04×10^{-6}	
	500.0	106.0	106.0		75.0	75.0	106.0	$.864\times10^{-6}$	$.864\times10^{-6}$	
	550.0			50.0						14.1×10^{-6}
Metlbond 1113	0.0	103.0	103.0	103.0	103.0	103.0	103.0	15.5×10^{-6}	15.5×10^{-6}	15.5×10^{-6}
	100.0	98.0	98.0	98.0	98.0	98.0	98.0	16.5×10^{-6}	16.5×10^{-6}	16.5×10^{-6}
	200.0	90.0	90.0	90.0	90.0	90.0	90.0	18.0×10^{-6}	18.0×10^{-6}	18.0×10^{-6}
	300.0	68.0	68.0	68.0	68.0	68.0	68.0	20.25×10^{-6}	20.25×10^{-6}	20.25×10^{-6}
	350.0	50.0	50.0	50.0	50.0	50.0	50.0	22.0×10^{-6}	22.0×10^{-6}	22.0×10^{-6}

TABLE C.2 Cont.

Matl.	Temp. °F	% E_{xx}	% E_{yy}	% E_{zz}	% G_{yz}	% G_{xz}	% G_{xy}	α_1 (in/in/°F)	α_2 (in/in/°F)	α_3 (in/in/°F)
Unidirectional B/E*	0.0	100.0	120.0	120.0	104.0	104.0	104.0	2.2×10^{-6}	9.6×10^{-6}	9.6×10^{-6}
	100.0	100.0	92.0	92.0	97.0	97.0	97.0	2.32×10^{-6}	1.11×10^{-5}	1.11×10^{-5}
	200.0	100.0			83.0	83.0	83.0	2.4×10^{-6}	1.34×10^{-5}	1.34×10^{-5}
	250.0	100.0			60.0	60.0	60.0			
	300.0	100.0	45.0	45.0	45.0	45.0	45.0	2.7×10^{-6}	1.68×10^{-5}	1.68×10^{-5}
[0/90/0/90/0] B/E	0.0	102.0	103.0	120.0	104.0	104.0	104.0	2.91×10^{-6}	3.45×10^{-6}	9.6×10^{-6}
	100.0	100.0	100.0	92.0	97.0	97.0	97.0	2.99×10^{-6}	3.51×10^{-6}	1.11×10^{-5}
	200.0	98.0	96.0		83.0	83.0	83.0	3.04×10^{-6}	3.55×10^{-6}	1.34×10^{-5}
	250.0				60.0	60.0	60.0			
	300.0	97.0	93.0	45.0	45.0	45.0	45.0	3.26×10^{-6}	3.71×10^{-6}	1.68×10^{-5}

* Ref. [1].

TABLE C.2 Cont.

Matl.	Temp. °F	% E_{xx}	% E_{yy}	% E_{zz}	% G_{yz}	% G_{xz}	% G_{xy}	α_1 (in/in/°F)	α_2 (in/in/°F)	α_3 (in/in/°F)
Titanium* 6Al-4V	0.0	101.3	101.3	101.3	101.3	101.3	101.3	4.7×10^{-6}	4.7×10^{-6}	4.7×10^{-6}
	70.0	100.0	100.0	100.0	100.0	100.0	100.0			
	400.0	95.0	95.0	95.0	95.0	95.0	95.0	5.2×10^{-6}	5.2×10^{-6}	5.2×10^{-6}
	800.0							5.6×10^{-6}	5.6×10^{-6}	5.6×10^{-6}
Aluminum* 2024-T4	0.0	104.0	104.0	104.0	104.0	104.0	104.0	12.1×10^{-6}	12.1×10^{-6}	12.1×10^{-6}
	70.0	100.0	100.0	100.0	100.0	100.0	100.0			
	200.0	99.0	99.0	99.0	99.0	99.0	99.0	12.9×10^{-6}	12.9×10^{-6}	12.9×10^{-6}
	250.0							13.0×10^{-6}	13.0×10^{-6}	13.0×10^{-6}
	300.0	94.3	94.3	94.3	94.3	94.3	94.3	13.1×10^{-6}	13.1×10^{-6}	13.1×10^{-6}
	400.0	88.7	88.7	88.7	88.7	88.7	88.7	13.2×10^{-6}	13.2×10^{-6}	13.2×10^{-6}
	500.0	80.2	80.2	80.2	80.2	80.2	80.2	13.5×10^{-6}	13.5×10^{-6}	13.5×10^{-6}

* Ref. [23].

APPENDIX D

Computer Program NONCOM1

NONCOM1 FORTRAN USERS GUIDE

Cards 1-5 (20A4)

Column	Contents
1-80	Title Cards

Card 6 (6I6)

Column		Contents
1-6	NE	= Number of elements
7-12	NDS	= Number of nodes
13-18	NDIFM	= Number of different materials
19-24	NANG	= Number of different angles
25-30	IELET	= Operating temperature indicator
		0 for 70°
		> 0 for any other temperature
31-36	IELEM	= Operating moisture content indicator
		0 for 0% moisture
		> 0 for elevated moisture content

Card 7 (6I6)

Column		Contents
1-6	NLOADS	= Number of load cases
7-12	NPSS(1)	= Load type number 1
13-18	NPSS(2)	= Load type number 2
etc.	Repeated NLOADS times	
	NPSS(J)	= 1 for axial strain
		= 2 for thermal

= 3 for axial force

= 4 for hygroscopic

Card 8 (5I6)

Column		Contents
1-6	NINCRT(1)	= Number of load increments for load case 1
7-12	NINCRT(2)	= Number of load increments for load case 2
etc.	Repeated NLOADS times	

Card 9 (5I6)

Column		Contents
1-6	KEY(1)	= Print indicator for grid
7-12	KEY(2)	= Print indicator for strains
13-18	KEY(3)	= Print indicator for stresses
19-24	KEY(4)	= Print indicator for equivalent stresses
25-30	KEY(5)	= Print indicator for displacements
		KEY(I) = 0 for printing

Card 10 (10I6) I=1, NLOADS

Column		Contents
1-6	LINCPR(1,I)	= First increment of load case I to print stresses, strains, and displacements
7-12	LINCPR(2,I)	= Last increment of load case I to print
etc.	Repeated NLOADS times	

Card 11 (2F12.6)

Column		Contents
1-12	SMY	= Scale factor for Y-coordinates

13-24 SMZ = Scale factor for Z-coordinates

The following card is repeated NLOADS times N=1,NLOADS

Card 12 (2F12.6)

Column		Contents
1-12	ALOADS(1,N)	= Load increment for first load case
13-24	ALOADS(2,N)	= Initial load state before applying increment

Card 13 is omitted if IELET = 0

Card 13 (F12.6)

Column		Contents
1-12	DELTOT	= Constant temperature for non-thermal loading

Card 14 is omitted if IELEM = 0

Card 14 (F12.6)

Column		Contents
1-12	DELMOT	= Constant moisture content for non-hygroscopic loading

The following cards are repeated NDIFM times

K=1,NDIFM (Cards 15-28)

Card 15 (5E12.6)

Column		Contents
1-12	EK11(K,1)	= E_{11} tension modulus
13-24	EK11(K,2)	= E_{11} compression modulus
25-36	EK22(K,1)	= E_{22} tension modulus
37-48	EK22(K,2)	= E_{22} compression modulus
49-60	EK33(K,1)	= E_{33} tension modulus
61-72	EK33(K,2)	= E_{33} compression modulus

Card 16 3E12.6

Column		Contents
1-12	GK23(K)	= G_{23} modulus
13-24	GK13(K)	= G_{13} modulus
25-36	GK12(K)	= G_{12} modulus

Card 17 (6E12.6)

Column		Contents
1-12	SP1(K,1)	= Elastic limit stress for $\sigma_1 - \varepsilon_1$ tension
13-24	N1(1,K,1)	= Ramberg-Osgood coefficient n_1 for $\sigma_1 - \varepsilon_1$ tension
25-36	K1(1,K,1)	= Ramberg-Osgood coefficient K_1 for $\sigma_1 - \varepsilon_1$ tension
37-48	SPI1(K,1)	= Bilinear intersect stress for $\sigma_1 - \varepsilon_1$ tension
49-60	N1(2,K,1)	= Ramberg-Osgood coefficient n_2 for $\sigma_1 - \varepsilon_1$ tension
61-72	K1(2,K,1)	= Ramberg-Osgood coefficient K_2 for $\sigma_1 - \varepsilon_1$ tension

Card 18 (6E12.6)

Column		Contents
1-12	SP1(K,2)	=
13-24	N1(1,K,2)	=
25-36	K1(1,K,2)	= Same as Card 17 but for $\sigma_1 - \varepsilon_1$
37-48	SP1(K,2)	= compression
49-60	N1(2,K,2)	=
61-72	K1(2,K,2)	=

Card 19 (6E12.6)

Column			Contents
1-12	SP2(K,1)	=	
13-24	N2(1,K,1)	=	
25-36	K2(1,K,1)	=	Same as Card 17 but for $\sigma_2 - \varepsilon_2$
37-48	SPI2(K,1)	=	tension
49-60	N2(2,K,1)	=	
61-72	K2(2,K,1)	=	

Card 20 (6E12.6)

Column			Contents
1-12	SP2(K,2)	=	
13-24	N2(1,K,2)	=	
25-36	K2(1,K,2)	=	Same as Card 17 but for $\sigma_2 - \varepsilon_2$
37-48	SPI2(K,2)	=	compression
49-60	N2(2,K,2)	=	
61-72	K2(2,K,2)	=	

Card 21 (6E12.6)

Column			Contents
1-12	SP33(K,1)	=	
13-24	N33(1,K,1)	=	
25-36	K33(1,K,1)	=	Same as Card 17 but for $\sigma_3 - \varepsilon_3$
37-48	SPI33(K,1)	=	tension
49-60	N33(2,k,1)	=	
61-72	K33(2,K,1)	=	

Card 22 (6E12.6)

Column			Contents
1-12	SP33(K,2)	=	
13-24	N33(1,K,2)	=	
25-36	K33(1,K,2)	=	Same as Card 17 but for σ_3 - ε_3
37-48	SPI33(K,2)	=	compression
49-60	N33(2,K,2)	=	
61-72	K33(2,K,2)	=	

Card 23 (6E12.6)

Column			Contents
1-12	SP23(K)	=	
13-24	N23(1,K)	=	
25-36	K23(1,K)	=	Same as Card 17 but for τ_{23} - γ_{23}
37-48	SPI23(K)	=	shear
49-60	N23(2,K)	=	
61-72	K23(2,K)	=	

Card 24 (6E12.6)

Column			Contents
1-12	SP13(K)	=	
13-24	N13(1,K)	=	
25-36	K13(1,K)	=	Same as Card 17 but for τ_{13} - γ_{13}
37-48	SPI13(K)	=	shear
49-60	N13(2,K)	=	
61-72	K13(2,K)	=	

Card 25 (6E12.6)

Column			Contents
1-12	SP3(K)	=	
13-24	N3(1,K)	=	
25-36	K3(1,K)	=	Same as Card 17 but for $\tau_{12} - \gamma_{12}$
37-48	SPI3(K)	=	shear
49-60	N3(2,K)	=	
61-72	K3(2,K)	=	

Card 26 (5E12.6)

Column		Contents
1-12	SL1(1,K)	= Ultimate stress for $\sigma_1 - \varepsilon_1$ tension
13-24	SL1(2,K)	= Ultimate stress for $\sigma_1 - \varepsilon_1$ compression
25-36	SI2(1,K)	= Ultimate stress for $\sigma_2 - \varepsilon_2$ tension
37-48	SL2(2,K)	= Ultimate stress for $\sigma_2 - \varepsilon_2$ compression
49-60	SL33(1,K)	= Ultimate stress for $\sigma_3 - \varepsilon_3$ tension
61-72	SL33(2,K)	= Ultimate stress for $\sigma_3 - \varepsilon_3$ compression

Card 27 (3E12.6)

Column		Contents
1-12	SL23(K)	= Ultimate stress for $\tau_{23} - \gamma_{23}$
13-24	SL13(K)	= Ultimate stress for $\tau_{13} - \gamma_{13}$
25-36	SL3(1,K)	= Ultimate stress for $\tau_{12} - \gamma_{12}$

Card 28 (6E12.6)

Column		Contents
1-12	UK12(K,1)	= Poisson's ratio ν_{12} in tension
13-24	UK12(K,2)	= Poisson's ratio ν_{12} in compression

25-36	UK23(K,1)	= Poisson's ratio ν_{23} in tension
37-48	UK23(K,2)	= Poisson's ratio ν_{23} in compression
49-60	UK13(K,1)	= Poisson's ratio ν_{13} in tension
61-72	UK13(K,2)	= Poisson's ratio ν_{13} in compression

If no thermal analysis is required skip to card 40

The following cards are repeated NDIFM times

K=1,NDIFM (Cards 29-39)

Card 29 (6I12)

Column		Contents
1-12	NT1(K)	= Number of linear segmented points for E_{11} modulus percent retention curve
13-24	NT2(K)	= Number of linear segmented points for E_{22} modulus percent retention curve
25-36	NT33(K)	= Number of linear segmented points for E_{33} modulus percent retention curve
37-48	NT23(K)	= Number of linear segmented points for G_{23} modulus percent retention curve
49-60	NT13(K)	= Number of linear segmented points for G_{13} modulus percent retention curve
61-72	NT3(K)	= Number of linear segmented points for G_{12} modulus percent retention curve

Card 30 (3I12)

Column		Contents
1-12	NT4(K)	= Number of linear segmented points for α_1 thermal coefficient curve

13-24	NT5(K)	= Number of linear segmented points for α_2 thermal coefficient curve
25-36	NTALP3(K)	= Number of linear segmented points for α_3 thermal coefficient curve

Card 31 (6F12.0) I=1,NT1(K)

Column		Contents
1-12	PERMR1(I,K)	= Percent retention of E_{11} modulus at point I
13-24	TEMP1(I,K)	= Temperature at point I
etc.	Repeated NT1(K) times	

Card 32 (6F12.0) I=1,NT2(K)

Column		Contents
1-12	PERMR2(I,K)	= Same as card 31 but for E_{22}
13-24	TEMP2(I,K)	= modulus

Card 33 (6F12.0) I=1,NT33(K)

Column		Contents
1-12	PMR33(I,K)	= Same as card 31 but for E_{33}
13-24	TMR33(I,K)	= modulus

Card 34 (6F12.0) I=1,NT23(K)

Column		Contents
1-12	PMR23(I,K)	= Same as card 31 but for G_{23}
13-24	TRM23(I,K)	= modulus

Card 35 (6F12.0) I=1,NT13(K)

Column		Contents
1-12	PMR12(I,K)	= Same as card 31 but for G_{13}
13-24	TMR13(I,K)	= modulus

Card 36 (6F12.0) I=1,NT3(K)

Column			Contents
1-12	PERMR3(I,K)	=	Same as card 31 but for G_{12}
	TEMP3(I,K)	=	modulus

Card 37 3(E12.5,F12.0) I=1,NT4(K)

Column			Contents
1-12	ALP1(I,K)	=	α_1 thermal coefficient at point I
13-24	TEMP4(I,K)	=	Temperature at point I
etc.	Repeated NT4(K) times		

Card 38 3(E12.5, F12.0) I=1,NT5(K)

Column			Contents
1-12	ALP2(I,K)	=	Same as card 37 but for α_2
13-24	TEMP5(I,K)	=	coefficient

Card 39 3(E12.5.F12.0) I=1,NTALP3(K)

Column			Contents
1-12	ALP3(I,K)	=	Same as card 37 but for α_3
13-24	TALP3(I,K)	=	coefficient

If no moisture analysis is required skip to card 51

The following cards are repeated NDIFM times

K=1,NDIFM (Cards 40-50)

Card 40 (6I12)

Column		Contents
1-12	NM1(K)	= Number of linear segmented points for E_{11} modulus percent retention curve
13-24	NM2(K)	= Number of linear segmented points for

C-3

		E_{22} modulus percent retention curve
25-36	NM33(K)	= Number of linear segmented points for E_{33} modulus percent retention curve
37-48	NM23(K)	= Number of linear segmented points for G_{23} modulus percent retention curve
49-60	NM13(K)	= Number of linear segmented points for G_{13} modulus percent retention curve
61-72	NM3(K)	= Number of linear segmented points for G_{12} modulus percent retention curve

Card 41 (3I12)

Column		Contents
1-12	NM4(K)	= Number of linear segmented points for β_1 coefficient
13-24	NM5(K)	= Number of linear segmented points for β_2 coefficient
25-26	NBETA3(K)	= Number of linear segmented points for β_3 coefficient

Card 42 (6F12.0) I=1,NM1(K)

Column		Contents
1-12	PERMR4(I,K)	= Percent retention of E_{11} modulus at point I
13-24	TEMM1(I,K)	= Moisture content at point I
etc.	Repeated NM1(K) times	

Card 43 (6F12.0) I=1,NM2(K)

Column			Contents
1-12	PERMR5(I,K)	=	Same as card 42 but for E_{22}
13-24	TEMM2(I,K)	=	modulus

Card 44 (6F12.0) I=1,NM33(K)

Column			Contents
1-12	PMMR33(I,K)	=	Same as card 42 but for E_{33}
13-24	TMMR33(I,K)	=	modulus

Card 45 (6F12.0) I=1,NM23(K)

Column			Contents
1-12	PMMR23(I,K)	=	Same as card 42 but for G_{23}
13-24	TMMR23(I,K)	=	modulus

Card 46 (6F12.0) I=1,NM13(K)

Column			Contents
1-12	PMMR13(I,K)	=	Same as card 42 but for G_{13}
13-24	TMMR13(I,K)	=	modulus

Card 47 (6F12.0) I=1,NM3(K)

1-12	PERMR6(I,K)	=	Same as card 42 but for G_{12}
13-24	TEMM3(I,K)	=	modulus

Card 48 3(E12.5, F12.0) I=1,NM4(K)

Column			Contents
1-12	BETA1(I,K)	=	β_1 hygroscopic coefficient at point I
13-24	TEMM4(I,K)	=	Moisture content at point I
etc.	Repeated NM4(K) times		

Card 49 3(E12.5, F12.0) I=1,NM5(K)

Column			Contents
1-12	BETA2(I,K)	=	Same as card 48 but for β_2
13-24	TEMM5(I,K)	=	coefficient

Card 50 3(E12,5,F12.0) I=1,NBETA3(K)

Column			Contents
1-12	BETA3(I,K)	=	Same as card 48 but for β_3
13-24	TBETA3(I,K)	=	coefficient

Card 51 (6F12.6)

Column		Contents
1-12	THE(1)	= Angle number 1 in degrees
13-24	THE(2)	= Angle number 2 in degrees
etc.	Repeated NANG times	

The following card is repeated NDS times

I=1,NDS

Card 52 (4I3,2F12.0)

Column		Contents
1-3	INODED(I)	= I
4-6	INODE(I,1)	= U - displacement code
7-9	INODE(I,2)	= V - displacement code
10-12	INODE(I,3)	= W - displacement code
		= 1 for force or non-zero displacement boundary condition
		= 2 for prescribed zero-displacement

13-24	YY(I)	= Y coordinate of node I before being scaled by SMY
25-36	ZZ(I)	= Z coordinate of node I before being scaled by SMZ

The following card is repeated NE times

I=1,NE

Card 53 (6X,5I6)

Column		Contents
1-6		= Blank
7-12	ND(I,1)	= Node number 1 of element I
13-18	ND(I,2)	= Node number 2 of element I
19-24	ND(I,3)	= Node number 3 of element I
25-30	IMAT(I)	= Material number of element I
31-36	ITHETA(I)	= Angle number of element I

Card 54 (2I12)

Column		Contents
1-12	NDCST	= Number of non-zero displacement constraints
13-24	NFCST	= Number of non-zero force constraints

If NDCST = 0 skip to card 56

The following card is repeated NDCST times

I=1,NDCST

Card 55 (2I12,F12.0)

Column		Contents
1-12	NODED(I)	= Node number of constrained node
13-24	MODE	= Code for constraint

= 2 for V constraint

= 3 for W constraint

25-36 DCST(I) = Displacement constraint increment

If NFCST = 0 no more input is required

The following card is repeated NFCST times

I=1,NFCST

Card 56 (2I12,F12.0)

Column			Contents
1-12	NODEF(I)	=	Same as card 55 but for force constraints
13-24	MODE	=	
25-36	FCST(I)	=	

Notes:

GENERAL: Input units need only be consistent except for thermal properties which must be degrees F.

Card 6 NE≤400, NDS≤400, NDIFM≤10, NANG≤10

Card 7 NLOADS≤ 5

Card 10 The first and last load increments are always printed

Card 11 The scale factors are multiplied by the Y and Z coordinates to obtain the final Y and Z coordinates

Card 12 ALOADS(2,N) is applicable to thermal and hygroscopic loading only. ALOADS(1,N) must be input as 0.0 for inplane loadings.

Card 32 Node numbers must be given in counter-clockwise order

A listing of the computer program is available upon request.